UCRL-LR-132438

Scaling Supernova Hydrodynamics to the Laboratory

J. O. Kane
(Ph.D. Thesis)

June 1999

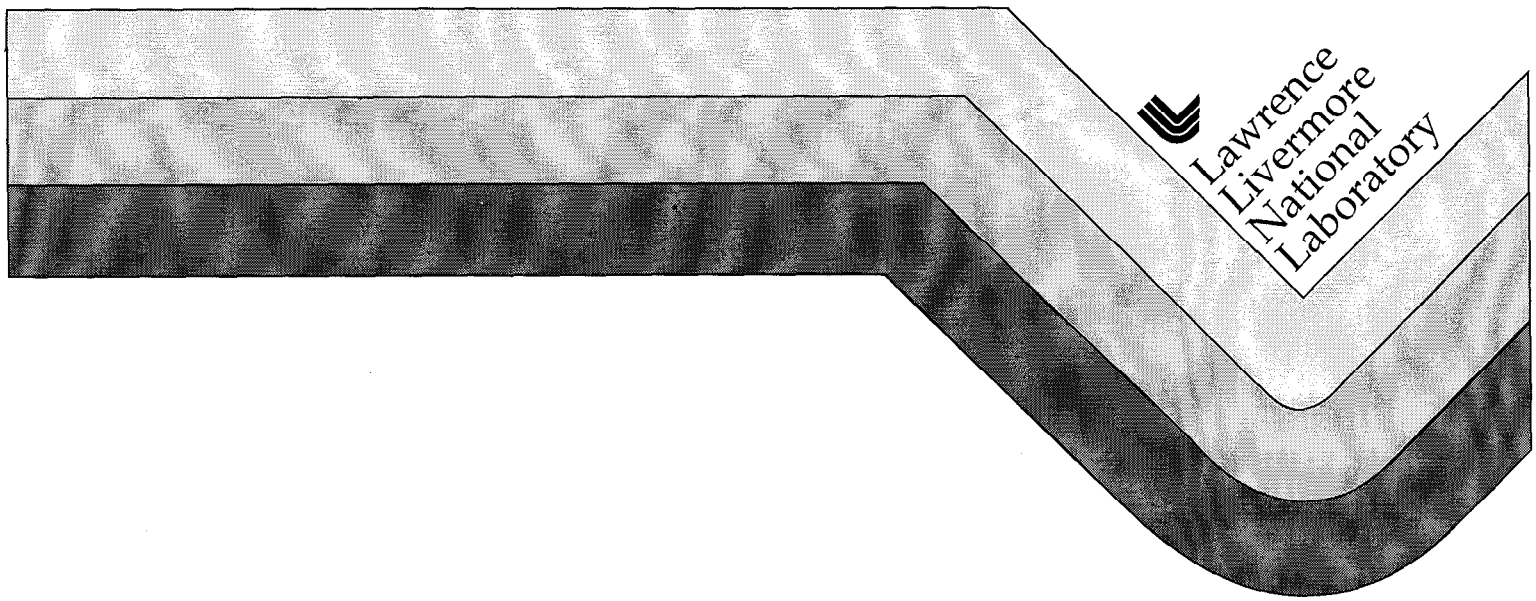

Work performed under the auspices of the U.S. Department of Energy by Lawrence Livermore National Laboratory under Contract W-7405-ENG-48.

UCRL-LR-132438
Distribution Category UC-0

Scaling Supernova Hydrodynamics to the Laboratory

J. O. Kane
(Ph.D. Thesis)

June 1999

LAWRENCE LIVERMORE NATIONAL LABORATORY
University of California • Livermore, California • 94551

SCALING SUPERNOVA HYDRODYNAMICS TO THE LABORATORY

Jave Kane, Ph. D.
The University of Arizona, 1999

Director: David Arnett

Supernova (SN) 1987A focused attention on the critical role of hydrodynamic instabilities in the evolution of supernovae. To test the modeling of these instabilities, we are developing laboratory experiments of hydrodynamic mixing under conditions relevant to supernovae. Initial results were reported in J. Kane *et al.*, Astrophys. J.**478**, L75 (1997) The Nova laser is used to shock two-layer targets, producing Richtmyer-Meshkov (RM) and Rayleigh-Taylor (RT) instabilities at the interfaces between the layers, analogous to instabilities seen at the interfaces of SN 1987A. Because the hydrodynamics in the laser experiments at intermediate times (3–40 ns) and in SN 1987A at intermediate times (5 s–10^4 s) are well described by the Euler equations, the hydrodynamics scale between the two regimes. The experiments are modeled using the hydrodynamics codes HYADES and CALE, and the supernova code PROMETHEUS, thus serving as a benchmark for PROMETHEUS. Results of the experiments and simulations are presented. Analysis of the spike and bubble velocities in the experiment using potential flow theory and a modified Ott thin shell theory is presented. A numerical study of 2D vs. 3D differences in instability growth at the O-He and He-H interface of SN 1987A, and the design for analogous laser experiments are presented. We discuss further work to incorporate more features of the SN in the experiments, including spherical geometry, multiple layers and density gradients. Past and ongoing work in laboratory and laser astrophysics is reviewed, including experimental work on supernova remnants (SNRs). A numerical study of RM instability in SNRs is presented.

STATEMENT BY AUTHOR

This dissertation has been submitted in partial fulfillment of requirements for an advanced degree at The University of Arizona and is deposited in the University Library to be made available to borrowers under rules of the Library.

Brief quotations from this dissertation are allowable without special permission, provided that accurate acknowledgement of source is made. Requests for permission for extended quotation from or reproduction of this manuscript in whole or in part may be granted by the head of the major department or the Dean of the Graduate College when in his or her judgment the proposed use of the material is in the interests of scholarship. In all other instances, however, permission must be obtained from the author.

SIGNED: _____

ACKNOWLEDGEMENTS

I would like to acknowledge the enthusiasm and cooperation of the Graduate College and the Department of Physics at the University of Arizona, and Lawrence Livermore National Laboratory, for making my term as a graduate student at the Laboratory possible. I wish to extend special thanks to Fulvio Melia of the Department for Physics for encouraging me to begin research in my first week at the University. I have been unusually fortunate to have supervision from two truly exceptional scientists, David Arnett and Bruce Remington. Each expects a lot, and in return, gives even more.

DEDICATION

To family old and new — Kerstin and Brian, Staci and Elijah.

TABLE OF CONTENTS

LIST OF FIGURES

ABSTRACT

Supernova (SN) 1987A focused attention on the critical role of hydrodynamic instabilities in the evolution of supernovae. To test the modeling of these instabilities, we are developing laboratory experiments of hydrodynamic mixing under conditions relevant to supernovae. Initial results were reported in J. Kane *et al.*, Astrophys. J.**478**, L75 (1997) The Nova laser is used to shock two-layer targets, producing Richtmyer-Meshkov (RM) and Rayleigh-Taylor (RT) instabilities at the interfaces between the layers, analogous to instabilities seen at the interfaces of SN 1987A. Because the hydrodynamics in the laser experiments at intermediate times (3–40 ns) and in SN 1987A at intermediate times (5 s–10^4 s) are well described by the Euler equations, the hydrodynamics scale between the two regimes. The experiments are modeled using the hydrodynamics codes HYADES and CALE, and the supernova code PROMETHEUS, thus serving as a benchmark for PROMETHEUS. Results of the experiments and simulations are presented. Analysis of the spike and bubble velocities in the experiment using potential flow theory and a modified Ott thin shell theory is presented. A numerical study of 2D vs. 3D differences in instability growth at the O-He and He-H interface of SN 1987A, and the design for analogous laser experiments are presented. We discuss further work to incorporate more features of the SN in the experiments, including spherical geometry, multiple layers and density gradients. Past and ongoing work in laboratory and laser astrophysics is reviewed, including experimental work on supernova remnants (SNRs). A numerical study of RM instability in SNRs is presented.

CHAPTER 1

INTRODUCTION

1.1 Overview

1.2 Motivation: Hydrodynamic instabilities in Supernova 1987A

Observations of supernova (SN) 1987A [10], a core collapse SN in the Large Magellanic Cloud, strongly suggested the occurence of material mixing driven by the Rayleigh-Taylor (RT) instability [104, 145] and its shock-driven analog, the Richtmeyer-Meshkov (RM) instability [130, 110]. More discussion of SN 1987A can be found in [10, 109, 155, 99] and references therein. Radioactive ^{56}Co from the shock-induced explosive burning of O was observed much sooner after the explosion than predicted by one dimensional (1D) spherically symmetric explosion models, implying that the ^{56}Co had been mixed well into the outer layers. The 'Bochum event' [80, 26] showed spectroscopic features suggesting enhanced heating of the envelope, presumably due to mixing from the radioactive core [139]. Furthermore, Doppler broadening of the gamma-ray and optical lines from ^{56}Co implied peak ^{56}Co velocities in excess of 3000 km/s [153, 148, 109]. Two dimensional (2D) modeling indeed confirms the presence of deep nonlinear RT-induced mixing [67, and references therein]. However, 2D simulations to date predict maximum velocities of $\leq$ 2000 km/s, suggesting that three dimensional (3D) effects may be important in accounting for the ^{56}Co velocities. Currently, much effort is being invested in studying the detailed multi-dimensional pre-explosion evolution of the O layer of SN 1987A [20, 13] in an effort to understand the types of initial perturbations which the blast wave may encounter in that layer. Theoretical, numerical and experimental work [51, 81, 107, 156] on single-mode perturbations in planar geometries suggests that hydrodynamic instabilities are expected to grow considerably faster in 3D than in 2D in the nonlinear regime.

An interesting analog to the planar case presents itself for the case of a SN, in which a

blast wave expands in spherical geometry through a steeply falling density gradient with density 'steps' (pronounced gradients) at interfaces between certain composition layers. Numerical simulations of SN 1987A [67] suggest that the interfaces between the O and He layers, and between the He and H layers of the progenitor were particularly prone to RT instabilities; these instabilities could potentially mix the ^{56}Co well into the outer layers of the star, so that observed velocity of the ^{56}Co is higher than predicted by 1D simulations. The effects of 3D hydrodynamics could potentially increase the observed ^{56}Co peak velocities further still.

Given the fundamental role played by the RM and RT instabilities in SN evolution, it is desirable to develop the means of testing the hydrodynamics of the SN codes. In this dissertation we report on results of scalable experiments using the Nova laser at Lawrence Livermore National Laboratory (LLNL) to test the modeling of compressible RM and RT instabilities. We discuss hydrodynamic instabilities in SN 1987A, and show numerical simulations of SN 1987A in 1D, 2D and 3D, performed using PROMETHEUS. We discuss scaling the hydrodynamics between SNe and the laser experiments, then present the results of SN-relevant hydrodynamic instability experiments at the Nova laser. We use the SN code PROMETHEUS to model these experiments, thus using them as a benchmark for PROMETHEUS. For comparison, as well as for the design of the experiment, we use the LLNL hydrodynamics code CALE. We present analytic theory that describes the combination of RM and RT single mode instability growth in the laser experiments. We also look at the role of RM instability in the later evolution of a SN, in the SNR stage.

The organization of this dissertation is as follows. In Chapter 1 we first motivate the research with a brief overview of hydrodynamics instabilities in SN 1987A (this section). We then briefly review some essential basic theory of fluid dynamics and hydrodynamic instabilities, describe the laser facilities which were used for the experiments, review other and previous work in astrophysics using intense lasers, and finally discuss the numerical codes we have used in this study. In Chapter 2 we first give an overview of hydrodynamic instabilities in SN 1987A, then consider numerical simulations of SN 1987A using PROMETHEUS, and discuss differences in 2D vs. 3D hydrodynamics in SN 1987A. In Chapter 3 we present the discussion of scaling between hydrodynamics in SNe and the laser experiment. In Chapter 4 we discuss the supernova-relevant hydrodynamic insta-

bility experiments. We first discuss the experimental setup and the targets, then look at 1D and 2D simuations of the experiment, compare the results of the experiment to the simulations, present the analytic theory of the instability growth in the experiments, and discuss differences in the simulations between the codes. In Chapter 5 we discuss further and ongoing work, including 2D vs. 3D hydrodynamic instability experiments, multiple-layer experiments, and a design for experiments at a future laser (the National Ignition Facility, described in Section 1.4.2.2). Appendix A describes a study of the RM instabilty in supernova remnants (SNRs). Appendix B discusses contemporary work in laser astrophysics.

1.3 Fluid dynamics and hydrodynamic instabilities

1.3.1 Overview

In this section we briefly describe some of the basic theory of fluid dynamics and hydrodynamic instabilities. Hydrodynamics and fluid dynamics are interchangeable terms describing the motion of fluids (liquids or gases.) Since the goal of the main experimental work described in this dissertation was to develop laboratory experiments which are well described by pure hydrodynamics, we will concentrate on hydrodynamics described by the Euler equations. Following the description in [97], the basic assumptions in fluid dynamics are that the fluids can be considered as continuous media. That is, when we consider the smallest volume of interest to us in the fluid, that volume still contains a very large number of molecules. For the purpose of writing down the differential equations describing the fluid, we assume that we can break down the fluid into very small volume elements that are infinitesimal in the sense that they are very small compared to the volume of fluid. To describe the fluid, we assign to each infinitesimal volume element a mean net velocity $\mathbf{v}$, and assign two independent thermodynamic quantities, such as density ρ and one of pressure P, temperature T, internal energy u, or total energy E, where E is simply the sum of the internal energy and the kinetic energy $mv^2/2$, m being the mass of the volume element. The equation of state (EOS) then determines the value of the third thermodynamic quantity. The EOS could be, for example, an ideal gas law (see [101], pp. 7–13),

$$P = \rho RT/\mu, \tag{1.1}$$

where R is the universal gas constant and μ is the molecular mass. For an ideal gas EOS, the relation

$$P = (\gamma - 1)u \tag{1.2}$$

also holds, where γ is the adiabatic index of the fluid (see [140], pp. 20–21, [101], pp. 7–13).

1.3.2 Compressible hydrodynamics

A compressible fluid is one in which the density of a fluid element can change over time. The most general equations describing a compressible fluid, including effects of radiation transfer, heat conduction, and viscosity, and a gravitational field $\mathbf{g}$, are the Navier-Stokes equations (see [140], p. 23, [97], p. 45),

$$\begin{aligned} \frac{\partial}{\partial t}\rho &+ \nabla \cdot (\rho \mathbf{v}) = 0 \\ \frac{\partial}{\partial t}(\rho \mathbf{v}) &+ \nabla \cdot (P\tilde{\mathbf{I}} + \rho \mathbf{v}\mathbf{v}) = \rho \mathbf{g} + \eta \nabla^2 \mathbf{v} \\ \frac{\partial}{\partial t}(\rho E) &+ \nabla \cdot [(\rho E + P)\mathbf{v}] = \rho \mathbf{v} \cdot \mathbf{g} + \rho \mathcal{L}(\rho, \mathcal{T}) \end{aligned} \tag{1.3}$$

where $\tilde{\mathbf{I}}$ is the unit matrix, η is the coefficient of viscosity and $\mathcal{L}$ accounts for transfer of energy by radiation, conduction, and viscosity. The middle line in Eqn. 1.3 is three equations, one for each component of $\rho\mathbf{v}$. The term $\nabla \cdot P\tilde{\mathbf{I}}$ is equivalent to simply ∇P, and $\mathbf{v}\mathbf{v}$ (a 2D matrix) is the outer product of $\mathbf{v}$ with itself; the divergence ($\nabla\cdot$) of either matrix is simply a vector. When viscosity is negligible and transfer of heat by radiation and conduction is negligible, the Navier-Stokes equations reduce to the Euler equations ([97], pp. 1–10),

$$\begin{aligned} \frac{\partial}{\partial t}\rho &+ \nabla \cdot (\rho \mathbf{v}) = 0 \\ \frac{\partial}{\partial t}(\rho \mathbf{v}) &+ \nabla \cdot (P\tilde{\mathbf{I}} + \rho \mathbf{v}\mathbf{v}) = \rho \mathbf{g} \\ \frac{\partial}{\partial t}(\rho E) &+ \nabla \cdot [(\rho E + P)\mathbf{v}] = \rho \mathbf{v} \cdot \mathbf{g} \end{aligned} \tag{1.4}$$

This set of five equations in the six variables $\mathbf{v}$, P, ρ and E are closed by the equation of state. The first of Eqns. 1.4 is a statement of the conservation of mass, the middle three (second line) a statement of the conservation of momentum, and the last a statement of conservation of energy. In the case of one space variable, x, with $g = (-g, 0, 0)$ Eqns. 1.4

reduce to the 1D Euler equations,

$$\begin{aligned} \frac{\partial}{\partial t}\rho &+ \frac{\partial}{\partial x}(\rho v) = 0 \\ \frac{\partial}{\partial t}(\rho \mathbf{v}) &+ \frac{\partial}{\partial x}(P + v^2) = -\rho g \\ \frac{\partial}{\partial t}(\rho E) &+ \frac{\partial}{\partial x}[(\rho E + P)v] = -\rho g v \end{aligned} \tag{1.5}$$

An operator-split code like PROMETHEUS (see Section 1.6.3) essentially solves Eqn. 1.5.

The Euler equations describe adiabatic flow, one in which the entropy of a fluid element does not change with time. However, in both SNe and in the laser experiments we discuss in this dissertation, we have shocks, which increase the entropy of fluid elements. Thus, shocks cannot be modeled by the Euler equations, and are instead modeled by the Rankine-Hugoniot shock jump conditions, which are statements of conservation across the shock discontinuity (see Ref. [140].) That is if we denote the change in a conserved quantity Q across the shock by $[Q]$, then we have, for example, in the case of an ideal fluid in one dimension ([140], p. 102)

$$\begin{aligned} [\rho v] &= 0 \\ \left[\rho v^2 + p\right] &= 0 \\ \left[\frac{1}{2}v^2 + \frac{\gamma}{\gamma - 1}\frac{P}{\rho}\right] &= 0 \end{aligned} \tag{1.6}$$

Numerical schemes for solving the hydrodynamics equations, such as those discussed in Section 1.6, must either use artificial viscosity to increase the entropy of a zone as a shock crosses the zone — HYADES (see Section 1.6.1) does this, or explicitly solve Eqns. 1.6) across a shock — PROMETHEUS (see Section 1.6.3) essentially does this.

1.3.3 Incompressible hydrodynamics

In an incompressible fluid, changes in density are negligible, that is $\partial\rho/\partial t = 0$, and $\mathrm{d}V = 0$, where $\mathrm{d}V$ is the volume of a fluid element. Assuming the flow is adiabatic, then $\mathrm{d}u = T\mathrm{d}s - P\mathrm{d}V = 0$ ([97], p. 10), and setting $\mathrm{d}S = 0 = \mathrm{d}V$, we have

$$\mathrm{d}u = 0. \tag{1.7}$$

We can arbitrarily set $u = 0$, and then reduce the Euler equations, Eqn. 1.4, to

$$\begin{aligned} \nabla \cdot \mathbf{v} &= 0 \\ \frac{\partial}{\partial t}\mathbf{v} &+ \nabla \cdot [(P/\rho)\tilde{\mathbf{I}} + \mathbf{vv}] = \mathbf{g} \\ \frac{\partial}{\partial t}(v^2/2 + P/\rho) &+ \nabla \cdot [(v^2/2 + P/\rho)\mathbf{v}] = \rho \mathbf{g}. \end{aligned} \tag{1.8}$$

However, the last of these equations is obtained by applying $(\mathbf{v}\cdot)$ to the third equation, so that we have just the first four equations, in the variables P and $\mathbf{v}$. In the special case where the fluid flow is irrotational everywhere, that is

$$\nabla \times \mathbf{v} = 0, \tag{1.9}$$

it easy to show that the flow must remain irrotational with time (see [97].) In this case, we can write $\mathbf{v}$ in terms of a potential ϕ as

$$\mathbf{v} = \nabla\phi, \tag{1.10}$$

and we say that we have *potential flow*. It follows from the first of Eqns. 1.8 and from Eqn. 1.10 that

$$\nabla^2\phi = 0, \tag{1.11}$$

while the momentum equations for the case of potential flow can be written in the form

$$\nabla \cdot [(\partial\phi/\partial t)\tilde{\mathbf{I}} + (P/\rho)\tilde{\mathbf{I}} + (\nabla\phi)^2] = \mathbf{g} \tag{1.12}$$

Potential flow is an important tool in the theory of hydrodynamic instabilities. In fact, potential flow can be defined for the compressible case as well (See [97], p. 14), but we will not need this extension.

1.3.4 Hydrodynamic instabilities

1.3.4.1 Rayleigh-Taylor (RT) instability

The Rayleigh-Taylor (RT) instability (see Refs. [104, 145]) occurs whenever a fluid of low density ρ_1 accelerates a fluid of higher density ρ_2, for example, when a layer of dense fluid sits atop a layer of less dense fluid in a gravitational fluid $\mathbf{g} = -g\hat{\mathbf{x}}$, directed

perpendicular to the interface, from the dense to the lighter fluid. In the case of constant g, the unperturbed fluids are in hydrostatic equilibrium,

$$\nabla p = -\rho \mathbf{g}, \tag{1.13}$$

which is just $\partial P/\partial x = \rho g$ in this case. Clearly, this situation is unstable ('heavy objects fall, light objects rise'). The light fluid can also accelerate the dense fluid when there is a pressure gradient such that the pressure is higher in the light fluid than in the dense fluid, for reasons other than the presence of a gravitational field. For example, in the case of SN 1987A, the pressure drops in the fluid inward in radius from the shock, as the fluid expands, and so pressure drops inward with radius from the shock (see Figure 2.3). In the laser experiments described in Chapter 4, the target decompresses behind the shock, so that the pressure at any time drops with distance behind the shock (see Figure 4.6). Any perturbations in the shape of the interface between the two fluids will grow over time into a pattern of rising bubbles of the lighter fluid separated by falling spikes of the denser fluid, with the fluids interpenetrating and eventually inverting to a stable configuration in which the dense fluid accelerates the lighter fluid. A *single mode* perturbation is a sinusoidal perturbation, and a *multimode* perturbation is a sum of single mode perturbations.

We now consider two incompressible, irrotational fluids in a constant gravitational field $\mathbf{g} = (-g, 0, 0)$ perpendicular to the interface between the fluids. In the case of a small amplitude single mode two dimensional (2D) perturbation in the shape of the interface, we can determine the growth rate of the perturbation by using linearized versions of Equations 1.8 (see Refs. [145, 104, 41]). We can also determine the growth rate by an intuitive argument for conservation of energy, as follows. Let λ be the wavelength of the perturbation, let $\eta(y) = \sin(ky) \ll \lambda$ be the infinitesimal amplitude of the perturbation, with the wavenumber $k = 2\pi/\lambda$, where y is the direction parallel to the unperturbed interface, and let $x = 0$ be the position of the unperturbed interface. One can confirm by substitution that the single mode solution of Eqn. 1.11 on either side of the interface is of the form

$$\phi = -\frac{\dot{\eta}}{k} e^{-k|x|} \sin(ky), \tag{1.14}$$

for some amplitude $\dot{\eta}$. Thus the velocity field on either side of the interface is

$$v_x = \frac{\partial \phi}{\partial x} = \dot{\eta} e^{-k|x|} \sin(ky) \tag{1.15}$$

$$v_y = \pm\frac{\partial\phi}{\partial y} = -\dot{\eta}e^{-k|x|}\cos(ky), \tag{1.16}$$

with the '+' sign for $x > 0$ and the '−' sign for $x < 0$. The magnitude $v(x,y) = (v_x^2+v_y^2)^{1/2}$ of the velocity at any point in the fluid is then

$$v(x,y) = \dot{\eta}e^{-kx} \tag{1.17}$$

By Eqn. 1.7, the internal energy of the fluid does not change, so we can equate the rate of change of total kinetic energy K in the fluid to minus the rate of change of total gravitational potential energy U of the fluid, as follows. Integrating the kinetic energy on both sides of the fluid over one wavelength λ by a 1 cm cross section of fluid, with the assumption that $\eta \ll \lambda$, we have

$$K = (\rho_1+\rho_2)\int_{x=0}^{\infty}\int_{y=0}^{\lambda}\frac{1}{2}v^2 \mathrm{d}x\ \mathrm{d}y \tag{1.18}$$

$$= (\rho_1+\rho_2)\frac{\dot{\eta}^2}{2}\int_{x=0}^{\infty}e^{-2kx}\mathrm{dx}\int_{y=0}^{\lambda}\mathrm{d}y \tag{1.19}$$

$$= (\rho_1+\rho_2)\frac{\dot{\eta}^2}{2}\frac{1}{2k}\lambda \tag{1.20}$$

$$= (\rho_1+\rho_2)\frac{\pi\dot{\eta}^2}{2k^2} \tag{1.21}$$

Hence,

$$\dot{K} = (\rho_1-\rho_2)\frac{\pi\dot{\eta}\ddot{\eta}}{k^2} \tag{1.22}$$

Integrating the potential energy on both sides of the interface, we have

$$U = (\rho_1-\rho_2)\int_{y=0}^{\lambda}\int_{x=0}^{\eta\sin(ky)}\rho g x\,\mathrm{d}y\,\mathrm{d}x \tag{1.23}$$

$$= (\rho_1-\rho_2)\frac{\pi g\eta^2}{2k} \tag{1.24}$$

Hence,

$$\dot{U} = (\rho_1+\rho_2)\frac{\pi g\eta\dot{\eta}}{k} \tag{1.25}$$

Setting $\dot{U} = \dot{K}$, we arrive at

$$\ddot{\eta}(t) = \frac{\rho_2-\rho_1}{\rho_1+\rho_2}kg\eta(t), \tag{1.26}$$

The solution to Equation 1.26 is

$$\eta(t) = e^{\gamma t}, \tag{1.27}$$

where the growth rate γ (not to be confused with the adiabatic exponent in Eqn. 1.2), is given by

$$\gamma = \sqrt{Akg}, \tag{1.28}$$

A being the Atwood number $(\rho_2 - \rho_1)/(\rho_1 + \rho_2)$. For rigorous derivation of the Equation 1.26, see References [104, 145, 41].

In the case just presented, we had two fluids, each of constant density, and the condition for instability was simply that fluid 2 at density ρ_2 is at lower pressure P than fluid 1 at density $\rho_1 < 1$. In the more general incompressible case, where there is not a sharp density discontinuity but a density gradient, the condition for instability is (see Reference [25])

$$\nabla P \cdot \nabla \rho < 0 \tag{1.29}$$

In the incompressible case (see Reference [14]), the condition for instability becomes

$$\nabla P \cdot \nabla \rho < 1/\gamma, \tag{1.30}$$

where γ is the adiabatic exponent.

In the nonlinear stage of RT instability, which occurs once η is no longer small compared to λ, the theory becomes more complicated. The usual method is to use perturbation theory and expand the potential flow equations, Eqns. 1.12, to two or more orders. Layzer [100, 81] developed a single-mode potential flow model for $A = 1$ and applied it successfully to 2D planar and 3D cylindrical bubbles. Layzer's model uses an approximate description of the flow near the bubble tip, on the assumption that the flow is driven by the rising bubbles, with the spikes acting as repositories for the dense matter. Lazyer's model predicts the linear growth rate of a bubble, and also the asymptotic velocity of a 2D bubble,

$$v_{b,\mathrm{asym}} = 0.230\sqrt{g\lambda}, \tag{1.31}$$

and a cylindrical bubble

$$v_{b,\mathrm{asym}} = 0.360\sqrt{g\lambda}, \tag{1.32}$$

Youngs [161] and Read [124] performed numerical and experimental investigations of multimode RT mixing, finding that the mixing width h (distance from bubble front to spike front) is given by

$$h = \alpha A g t^2, \tag{1.33}$$

where α appears to be about 0.07 for true 3D evolution of the mixing. Hecht *et al.* [81] adapted the Layzer theory, extending it to the multimode case for $A = 1$, and also to the case of the RM instability for $A = 1$, discussed in Section 1.3.4.2. Alon *et al.* [6] studied single-mode, two-bubble and multimode RT mixing for arbitrary density ratios, finding that the mix width constant α was approximately 0.05 at all density ratios. Haan [78] developed a model for predicting when nonlinear effects become important in multimode RT instability in a system of size L; he found that nonlinear effects begin when mode amplitudes reach about $(Lk^2)^{-1}$ for modes of wave number k and system size L. Plesset [122] studied the RT instability for incompressible fluids in spherical geometry, finding that the stability conditions for planar geometry do not apply without significant modifications. Yedvab *et al.* [159] studied single and multimode RT instability in cylindrical systems. In the deep nonlinear stage of RT instability, the interface shape becomes complex, because of vortices induced by the Kelvin-Helmholtz (KH) instability (see Section 1.3.4.4), and one must resort to numerical simulation.

1.3.4.2 Richtmeyer-Meshkov (RM) instability

The Richtmeyer-Meshkov (RM) instability [130, 110] occurs whenever a shock wave passes through a material perturbation (perturbation in the shape) of the interface between two fluids of different densities or different compressibilities. The passage of the shock through the interface causes perturbations in the pressure which tend to reinforce the initial perturbation. The RM instability occurs whether the Atwood number is positive or negative, that is, whether the shock passes from a light to a heavy fluid or from a heavy to a light fluid. There is a large and growing body of literature on the RM instability, because of its importance in such applications as astrophysics and inertial confinement fusion (ICF) [103, 102]. The theory of the RM instability is more complicated than that of the RT instablity because of the action of the shock and the essential role of compressibility in the interaction of the shock with the interface. In the case of heavy to light, the RM instability first changes the phase of the instability (inverts the perturbation.) In the light to heavy case, refraction of the shock through the interface causes pressure to decrease in the fluid in front of the peaks of the perturbation (between the interface and the shock) and to increase in the fluid ahead of the valleys of the perturbation. These changes in pressure cause the peaks and valley to grow in amplitude. In the heavy to light

case, the pressure increases ahead of the peaks and decreases ahead of the valleys, which causes the initial inversion, after which the perturbations grow in the opposite phase. The interaction of the shock with the interface will in general produce a transmitted shock, and a reflected wave which may be a shock or a rarefaction, depending upon the Atwood number A, the EOS of the fluids, and the strength of the shock (see Ref. [158, 73]),

A basic intuitive description of the RM instability, comparable to the description of the RT instability (above) may be more elusive than has traditionally been appreciated (see [149] for a discussion of this.) The RM instability was first studied theoretically by Richtmeyer (Ref. [130]) and experimentally by Meshkov (Ref. [110]). Richtmeyer presented two models of the RM instability for the case of a reflected shock, The first model is obtained by linearizing the Euler equations (Eqns. 1.4), and the second is an impulsive model where the RM instability is seen as a limiting case of the RT instability in which the accelerating field g is a impulse of infinitesimal duration (see [149] for a discussion of the validity of this notion.) Richtmeyer obtained linearized equations for the amplitude $\eta(t)$ of the perturbations:

$$\ddot{\eta} = kAg(t)\eta \tag{1.34}$$

$$\eta(t_0) = \eta_0 \tag{1.35}$$

$$\dot{\eta}(t) = 0, \tag{1.36}$$

where $g(t)$ is the acceleration and A is the Atwood number. The rate of amplitude growth $\dot{\eta}$, first increases, and then approaches a constant asymptotic value after some oscillations. Equations 1.34 have been studied numerically [158] and by perturbation theory, in an extension to the case of a reflected rarefaction [149]. Richtmeyer also modeled the effect of the shock as an impulse of the form

$$G = \Delta V \delta(t), \tag{1.37}$$

where ΔV is the velocity change induced by the impulse. Substituting Eqn. 1.37 into the first of Eqns. 1.34 yields

$$\dot{\eta} - \dot{\eta}_0 = -kA\Delta V\eta_0, \tag{1.38}$$

As Richtmeyer noted, the constant η_0, an initial amplitude, was ambiguous, because a determination of its value involves effects of compressibility, whereas the derivation of

Eqn. 1.38 begins with the potential flow equations, Eqn. 1.12. Richtmeyer chose $\eta_0 = \eta_0^*$, the postshock amplitude of the perturbation, which is given roughly by

$$\eta_0^* = \eta_0(1 - \Delta V/c_s), \tag{1.39}$$

where c_s is the incident shock speed; this formula accounts for the distance the valley of the perturbation moves by the time the peak is hit by the shock. In the case of heavy to light, the interface is inverted by the shock. If ΔV is greater than c_s, then the perturbation will invert before the shock reaches the peak (see Eqn. 1.39) of the perturbation, and the inversion is called a 'direct' inversion; otherwise, the inversion is called an indirect inversion (See Reference [84]).

Meshkov [110] observed the RM instability in both light to heavy and heavy to light shock tube experiments. However, in the light to heavy case, the growth rates were on the order of 50% of the prediction of the linearized Richtmeyer theory. Meshkov noted that experimental artifacts may have changed the growth rate. Meyer and Blewett [111] addressed the discrepancy by numerical simulations. They noted that the initial amplitudes in the Meshkov experiment were too large to be considered linear. Thus, they performed light to heavy numerical simulations with smaller amplitudes than Meshkov used, and found that the simulations also gave signficantly higher growth rates than those observed experimentally. However, for the light to heavy case they found that the simulations agreed well with the Richtmyer impulsive theory, Eqn. 1.38. Meyer and Blewett also performed numerical simulations of the heavy to light case, and found that they obtained agreement with the impulsive theory if instead of using Eqn.1.39 for the post-shock amplitude in Eqn. 1.38, they used the average of the preshock and postshock amplitudes, that is

$$\eta_{0,\mathrm{MB}}^* = (\eta_0 + \eta_0^*)/2. \tag{1.40}$$

Considerable further work has been done on the RM instability, both experimental and theoretical. Benjamin [22, 23] and Aleshin *et al.* [4] have performed further shock tube experiments. Benjamin saw growth rates higher than Meshkov's but significantly smaller than predicted by Eqn. 1.38. Aleshin *et al.* considered the transition from the linear to the nonlinear stage and found growth rates slightly above the prediction of Eqn. 1.38. Dimonte and collaborators [56, 57] have performed experiments to study the RM instability at high compression at the Nova laser (see Section 1.4.1). They

produced a nearly constant velocity shock in a planar target driven by x-rays from the hohlraum (see Section 1.4.1 and Chapter 4). In [56], the growth rates they observed were in agreement with linear theory if they used the Meyer-Blewett prescription, Eqn. 1.40, for the amplitude in the heavy to light case. In [57], multimode RM was studied, and the turbulent mix width h (distance from bubble to spike front) was observed to vary as $h \sim t^{\beta}$, with $\beta \sim 0.6 \pm 0.1$.

Hecht [81] extended the work of Layzer on potential flow models for RT instability [100] to multimode RM instability, for incompressible fluids with $A = 1$ (massless second fluid.) Alon *et al.* [6] studied single-mode, two-bubble and multimode RM mixing for arbitrary density ratios, finding, in disagreement with the later experimental results of Dimonte *et al.* [57] that the mix width exponent β was approximately 0.4 at all density ratios. Velikovich and Dimonte [150, 149] have developed higher order perturbation theory for single modes. Zhang and Sohn [163] used Padé approximants and asymptotic matching to develop a quantitative nonlinear theory for the compressible RM instability that gave excellent agreement with experiments and numerical simulations [85, 22]. Graham [73] performed extensive numerial studies of the RM instability in cylindrical geometry, and gives an excellent review of theory, simulations and experiments of RM instability.

1.3.4.3 Nonlinear Asymptotic RT and RM velocities — drag vs. buoyancy

For the single mode RM and RT cases, a simple intuitive argument can be made for the evolution of the bubble and spike velocities in the nonlinear stages. This discussion follows [5, 81]. Newton's equation for the heavy fluid above the bubble is

$$\rho_2 V \frac{\mathrm{d}u}{\mathrm{d}t} = c(\rho_2 - \rho_1) g V - c_{\mathrm{D}} \rho_2 u^2 S, \tag{1.41}$$

where the subscripts 1 and 2 refer to the dense and light fluids, respectively, u is the velocity of the bubble tip, S is the bubble's cross-sectional area, V is the volume of dense fluid set in motion by the bubble, c is a constant and c_{D} is the drag coefficient. The buoyancy term, $c(\rho_2 - \rho_1)gV$ accounts for the rising of the bubble under the force of the acceleration g, and the drag term accounts for the momentum which the bubble must impart to the dense fluid as the bubble pushes the dense fluid out of the way. Dividing Eqn. 1.41 through by $\rho_2 V$, using the definition of A, and taking $S/V \sim \lambda$, we arrive at

$$\dot{u} = c \cdot 2A/(1 + A) g - c_{\mathrm{D}} u^2/\lambda. \tag{1.42}$$

Ignoring the changes in c and c_D as the bubble rises and changes shape somewhat, we can now find the asymptotic RM and RT velocities. For RM, setting $g = 0$ in Eqn. 1.42, that is, assuming no accelerating force, Eqn. 1.42 reduces to $\dot{u} = c_D u^2/\lambda$, which has the solution

$$u = c_D^{-1}\lambda/t. \tag{1.43}$$

Doing full scale numerical solutions with single mode perturbations, Alon *et al.* found

$$c_D^{-1} = (3\pi)^{-1} \approx 0.11, A \gtrsim 0.5 \tag{1.44}$$

$$c_D^{-1} \approx 0.15, \text{ for low values of } A \tag{1.45}$$

For RT, setting $\dot{u} = 0$ in Eqn. 1.42 we arrive at $c \cdot 2A/(1+A)g = c_D u^2/\lambda$, which gives $u_{\text{bubble,asym.}} = (cg\lambda c_D^{-1} \cdot 2A/(1+A))^{1/2}$. Again from numerical simulations, Alon *et al.* found that $c \approx 1/2$ for $A \gtrsim 0.5$, To obtain the result for the spike, we reverse the roles of fluid 1 and fluid 2 in Eqn. 1.41. The equation for bubble and spike velocities then becomes

$$\dot{u} = c_B g - c_D u^2/\lambda, \tag{1.46}$$

where u is the bubble or the spike velocity, and

$$c_B = \frac{A}{1+A} \tag{1.47}$$

$$c_{D,\text{bubble}} = 3\pi \tag{1.48}$$

$$c_{D,\text{spike}} = 3\pi \cdot \frac{1-A}{1+A} \tag{1.49}$$

for $A \gtrsim 0.5$. Setting $\dot{u} = 0$ in Eqn. 1.46 and using Eqn. 1.47, the asymptotic velocities for RT are

$$u_{\text{asym}} = \sqrt{\frac{1}{6\pi}\frac{2A}{1 \pm A} g\lambda}, \tag{1.50}$$

for $A \gtrsim 0.5$, with the $+$ for the bubble and the $-$ for the spike.

1.3.4.4 Kelvin-Helmholtz (KH) instability

The Kelvin-Helmholtz (KH) instability occurs whenever there is a shear, that is, a change in the transverse velocity, between two adjacent layers of fluid. The KH instability does not involve a gravitational or impulsive force as the RT and RM instabilities do. The KH instability is manifest in the studies in this dissertation as waves along the sides of

bubbles and spikes and as rollups at the tips of spikes (see Figures 2.6 and 4.11.) Shore [140] gave an intuitive explanation of the KH instability in terms of the airfoil effect. For simplicity, assume steady ($\partial \mathbf{v}/\partial t = 0$) potential flow (Eqns. 1.11 and 1.12), with $\mathbf{g} = 0$. It follows (See [97], P. 18) that

$$\mathrm{d}/\mathrm{d}t(v^2/2 + P/\rho) = 0, \tag{1.51}$$

which is Bernoulli's equation, where $\mathrm{d}/\mathrm{d}t$ means that we follow a particular fluid element. Hence, at the point in the steady flow where the velocity of the fluid element is highest, the pressure of the fluid element is lowest. Thus, given two layers of fluids in motion relative to each other, with the velocities of the layers directed parallel to the interface between the layers, if there is a slight upward perturbation to the shape of the interface, the overlying flow will be forced to deviate around the perturbation, with an accompanying increase in velocity and drop in pressure. Thus, the upward perturbation will experience lift, reinforcing the perturbation. Eventually, the shear of the flow will cause the perturbation to curl up into a vortex.

1.3.4.5 2D vs. 3D hydrodynamic instabilities

3D perturbations grow faster in the nonlinear regime than 2D perturbations, because the growth saturates later in 3D (see Refs. [100, 51, 156, 82] and references therein for theoretical work on this topic). Marinak *et al.* [107] investigated 2D vs. 3d growth in acceleration, with a light fluid, the ablated material, acclerating the dense target, in indirect drive experiments at the Nova laser. They found that 3D perturbations grew approximately 50% faster than 2D perturbations, at the ablation front, when the wavenumbers were chosen to give the same growth rate in the linear regime. Workers in SNe have noted possible 2D vs. 3D effects in their simulations of SNe (eg. [118].) The difference in 2D vs. 3D growth can be understood qualitatively by a drag vs. buoyancy argument for incompressible fluids. A 2D bubble of low density fluid shaped like a ridge has to push more high density material out of its way (imparting momentum to it) as it rises than a hill-shaped 3D bubble [51, 81, 107]. That is, the kinematic drag per unit buoyant force is larger in 2D, making the terminal bubble velocity lower. The bubble velocity u will change with time according to Equation 1.46. The buoyancy and drag coeffecients, c_B and c_D respectively, account for the shape of the bubble and spike and therefore the

differences between 2D and 3D. For the case $A = 1$, Layzer [100] and Hecht *et al.* [81] found that the 3D asymptotic RT bubble velocities were

$$u_{3D,RT,asym} = \sqrt{g/k} \tag{1.52}$$

For $A = 1$, Eqn. 1.50 gives 2D asymptotic RT bubble velocities of $\sqrt{(1/6\pi)g\lambda} = \sqrt{1/3}\sqrt{g/k}$ $\approx 0.577\sqrt{g/k}$. That is, the 3D asymptotic RT velocity is about 73% higher than the 2D asymptotic RT velocity, when the same wavenumber is used for the 2D and 3D perturbations. The 2D-3D difference will be discussed for specific scenarios in Sections 2.4 and 5.1.

1.4 A survey of some intense lasers

1.4.1 Nova facility

1.4.1.1 Overview

In this section we discuss the Nova laser facility, located at Lawrence Livermore National Laboratory in Livermore, CA. More information on Nova can be found in [39, 37, 40] and references therein.

1.4.1.2 ICF

The primary mission of the Nova laser is the study of Inertial Confinement fusion (ICF). In ICF, two isotopes of H, deuterium (D) and Tritium (T), are combined under very high temperatures and pressures. The fuel in a DT fusion capsule is heated to over 10^7 K and compressed to a density 20 times that of lead. The pressures achieved in the core of capsule are on the order of 10^5 Mbar (10^{17} ergs/cm^3 or 10^{11} atmospheres.) The fusion products are He, a neutron, and energy. The laser energy is used to heat the outer layers of the fuel capsule, which is about the size of a grain of salt, and composed of a shell of plastic (CH) surrounding the DT fuel. The energy is supplied either by shining the laser beams directly on the surface of the capsule (direct drive), or by mounting the capsule inside a cylindrical gold radiation cavity (a hohlraum — see Figure 4.1), resulting in a nearly blackbody radiation field of temperature 200–300 eV (1 eV equals 11605 K) that bathes the capsule.

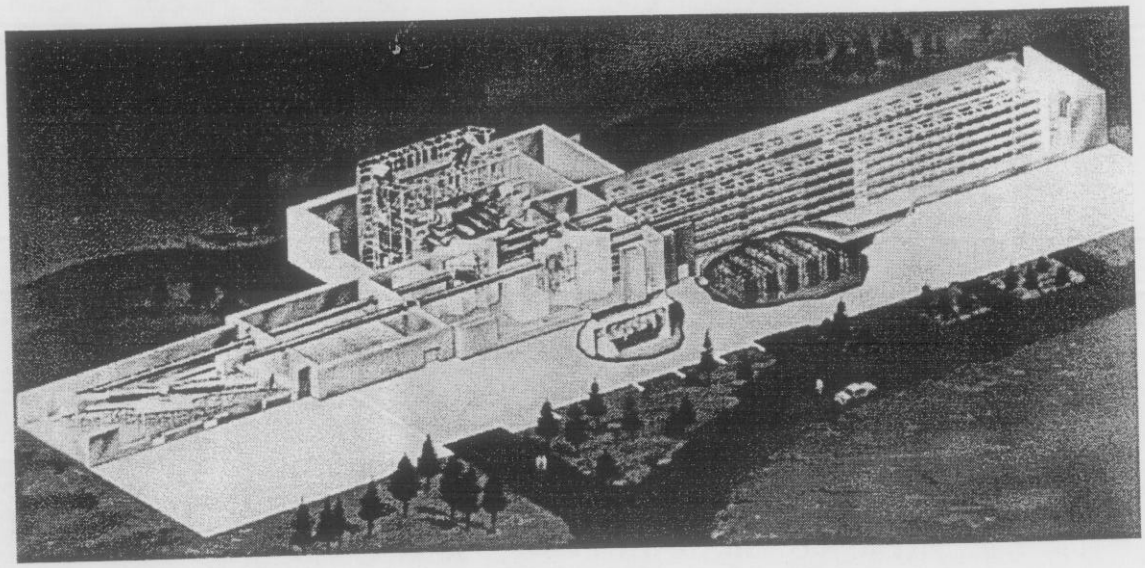

Figure 1.1: The Nova laser facility

The laser energy heats the surface of the fuel pellet's outer shell so rapidly that the surface begins to boil away. The rocket-like action of the boiled-off surface material causes a shock wave to propagate inward into the remaining material of the shell, causing the fuel pellet to implode. The pellet is reduced in radius by a factor of 30, compressing the DT fuel to the point that fusion occurs. The Nova laser supplies a maxium of 150 kJ of energy per shot. The amount of energy required for break-even fusion, in which more energy is produced than input, is calculated to be over 1 Mbar. The Nova is also used for a wide variety of experiments besides ICF, including XUV/x-ray lasers, hydrodynamics, radiation generation and transport, equation of state measurements, and recently, laboratory astrophysics.

1.4.1.3 The facility

The Nova laser system (Figure 1.1) is located at Lawrence Livermore National Laboratory in Livermore, California. The Nova laser operates two shifts per day, five days per week, and produces about 1400 experiments per year. Approximately 60 personnel operate the laser and target areas. The laser consists of a 120-terawatt (TW — 10^{15} W) neodymium:glass laser that can be directed into two target chambers for inertial confinement fusion experiments. The laser consists of ten separate beams, that operate at 1.05 μm wavelength (frequency '2ω'). The laser light is frequency converted using large

potassium diphosphate (KDP) crystals just before the target chambers to the second or third harmonic, or 0.53 μm (frequency 2ω) and 0.35 μm (frequency 3ω) respectively. The final diameter of each beam is 74 cm. The f/4 focus lenses on each chamber provide a focused spot at target of about 150 μm (about twice the size of a human hair), with peak intensity delivered to target of approximately 10^{17} W cm^{-2}. The maximum energy on target is $\approx$ 100 KJ at 1ω, or $\approx$ 40 KJ at 2ω or 3ω. The pulse length can be varied from 20 picosecond (ps — 10^{-12} s) to 1 nanosecond (ns — 10^{-9} s) Gaussian, or 500 ps to 10 ns in a shaped form. All beams can be individually pointed with a precision of about 30 μm at chamber center. Beam power balance of $< 5\%$ rms at the peak of temporally shaped pulses can be provided. Up to three of the beams can be used as target backlighters (see Section 1.4.1.5), with from 0 to 50 ns delay from the main pulse.

1.4.1.4 Target Chambers

The target chambers are spherical vacuum vessels with target inserter systems that allow remote operation for a variety of target experiments. Both target chambers have a range of target diagnostics for measuring X-ray, optical light, and neutron emissions. The chambers are located in separate rooms for increased system flexibility. The 10-Beam chamber is about 4.5 m diameter of aluminum and the 2-Beam chamber is about 1.8 m diameter of stainless steel. There are two, 1ω, chirped pulse lasers that can be used on the target chambers in conjunction with the ten beam laser system. A 100 TW system is available for use on the 2-Beam target chamber, with a 1ω pulse of about 40 J in 400 femtoseconds (fs — 10^{-15} s). A Petawatt system has been built on the 10-Beam target chamber, where one of the ten beams is modified to produce a 1ω pulse of about 1 kJ in 1 ps.

1.4.1.5 Diagnostics

The diagnostics at Nova can be grouped into four different types: X-ray Spectrometers, Neutron Diagnostics, Optical Diagnostics, and X-ray Imagers. The principal uses of the X-ray spectrometers include measuring time resolved density and electron temperature of ICF implosions, measuring ionization states, making opacity measurements, and measuring energy of fast electrons. Principal uses of neutron diagnostics are for ICF: measuring fuel areal density and ion temperature, and hydrodynamic mixing and asymmetry in

the implosion. Principal uses of optical diagnostics include measurements of hohlraum radiation temperatures with streaked optical pyrometer, and measurements of plasma instabilities.

The diagnostics of the most direct importance to the experiments described in this dissertation are the x-ray imagers. The gated x-ray framing camera [21], used in ICF for imaging symmetry of implosions, is also for x-ray backlighted images (radiographs). The usual strategy in a radiograph is to select a backlighter material which, when heated by laser, radiates x-rays at a wavelength to which some of the materials in the target are more opaque and others more transparent, so that a shadow of the more opaque materials are recorded on film (see Refs. [69, 36]). In *face on* radiography we look through the target perpendicular to some surface of interest, such as an ablation front or an interface between two materials. In *side on* radiograpy we look sideways through the target, parallel to the the surface of interest. The framing camera allows multiple images on a shot ($\approx$ 16), and uses an 80 ps gated x-ray pinhole imager. A Wölter x-ray microscope [63, 125] is available; it provides 22 $\times$ magnification for x-ray backlit images. Also used is a 1D steaked-slit imager [126]. The x-ray imagers can be used to make time-streaked images, in which the x-ray signal is integrated in one space dimension to provide an average 1D image vs. time, or to make static 2D images at selected times.

1.4.1.6 Time and distance scales

Some typical scale lengths for Nova experiments are as follows. Experimental times are measured in ns (10^{-9} s), with the drive pulses typically lasting from 1 to 5 ns, and observations of the experiment lasting 5–40 ns. The indirect drive hohlraums are measured in millimeters, and the target dimensions are measured in hundreds of microns (1 μm = 10^{-6} m = 10^{-4} cm.) Pressures on high energy shots are typically measured in the tens of Mbar (10^{12} erg/cm^3). Temperatures in laser experiments are commonly expressed in the energy unit eV, where 1 eV = 11605 K. Radiation temperatures inside hohlraums are measured in hundreds of eV. Temperatures inside targets in the range of 1–10 eV, and can be much higher, in ablated material, or inside ICF capsules, for example. Densities in irradiated targets are typically on the order of few tenths of a g/cm^3 to a few g/cm^3, but can be much higher in ICF capsules, for example, and much lower in ablated material.

1.4.1.7 Hydrodynamics experiments at the Nova laser

Hydrodynamics instabilities have been the focus of intensive research in ICF for some time (see, for example, [103, 144]). As shocks cross the shell in an ICF capsule, capsule surface finish perturbations will grow due to the RM instability. The low density shell material ablated away by the laser energy accelerates the denser remaing shell, and so the ablation front is RT unstable. Perturbations at the outer surface grow and feed through to the inner surface of the capsule. When the shock rebounds from the core of the capsule, the shell decelerates, and becomes RT unstable. The mixing produced by these instabilities can cause shell material to penetrate the core, degrading the capsule performance [103]. Thus understanding the RM and RT instabilities (and learning how to control them in ICF), is of critical importance to the ICF mission.

Remington and collaborators have done a series of Nova laser experiments to study the RT instability. In Ref. [127] they describe experiments in which a foil of FS ($SiOC_4F_3$) or CHBr (brominated plastic) is mounted across a diagnostic hole in the side of the hohlraum and accelerated by ablation induced by the x-ray drive from the hohlraum. Modulations are imposed in the solid target to act as seeds for ablative RT instability. The growth of modulations is diagnosed with face on (looking perendicular to the ablation front) or side on (looking parallel to the ablation front) x-ray radiographs. 1D time-streaked imaging is done using a Wölter x-ray microscope or slit image. 2D imaging is done with the gated x-ray pinhole camera. Single mode perturbations allowed measurments of RT growth rates in the linear and nonlinear regimes. In [128], Remington *et al.* used CHBr foils with two or eight sinusoidal wavelengths superposed, observing coupling of modes and production of beat modes in the nonlinear regime. Marinak *et al.* [107] observed the difference in RT growth between 2D and 3D perturbations in ablatively accelerated CHBr foils. Dimonte and Remington [56] and Dimonte *et al.* [57] did Nova laser experiments to study RM growth. See Sections 1.3.4.1 and 1.3.4.2 for further discussion of the hydro experiments mentioned here, and also see Reference [40].

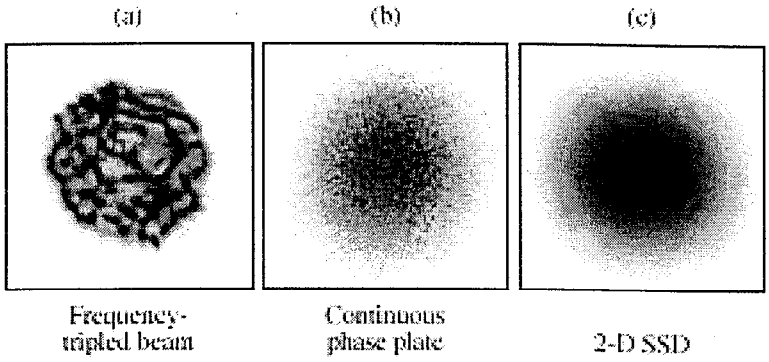

Figure 1.2: Beam smoothing with SSD at Omega (a) Frequency-tripled beam (0.35 μm). (b) phase plate, no SSD, and (c) with SSD. Images are integrated over 1 ns.

1.4.2 Other facilities

1.4.2.1 OMEGA

The OMEGA laser [50, 96] is located in the Laboratory for Laser Energetics at the University of Rochester in Rochester, NY. Like Nova, it is a neodymium:glass laser, and like Nova, is typically used to deliver up to 30 kJ of energy per shot. OMEGA has 60 beams, as opposed to Nova's 10 beams, thus operating at lower energy per beam. OMEGA is used for similar research to Nova. One of the main research goals at OMEGA is doing preparatory work for the direct-drive ICF capability of the National Ignition Facility (NIF) (see Section 1.4.2.2). In addition to ICF, a wide variety of experiments are fielded at OMEGA, including experiments in plasma physics, spectroscopy of highly ionized atoms, fundamental physics, materials science, biology, chemistry, and laboratory astrophysics. As with Nova, the fundamental wavelength of the laser is 1.05 μm; target irradiation is usually done at the third harmonic of the fundamental, 0.35 μm. OMEGA has beam smoothing by spectral dispersion (SSD) [142] to provide a more uniform direct drive irradiation pattern on target (see Figure 1.2). Target experiments on OMEGA are carried out in a 3.3 m diameter vacuum chamber. OMEGA's beam pointing precision and stability have been measured as ± 16 μm, and its beam energy imbalance as less than $\pm 4\%$ rms.

1.4.2.2 The National Ignition Facility

The 192 beam National Ignition Facility [3] will be the successor to Nova. NIF will delivery 1.8 MJ, 40 times the energy of Nova, at 10 times the power of Nova, to the target. The first bundle of NIF beams will be online in 2001, and the full 192 beam system will be complete by late 2003. NIF will be the first laser facility to produce break-even ICF. NIF will be the latest in a long line of glass:neodymium lasers that have been built since 1960 at Livermore; other lasers were the Long Path laser, the two-beam Janus laser, Cyldos, Argus, the 10-beam 10 kJ Shiva, the Novette laser, and Nova.

1.4.2.3 Gekko

The Gekko laser [1] is located at the Institute of Laser Engineering at Osaka University in Osaka, Japan. The Institute was established for laser fusion research, high power laser development, and the study of their applications. The Gekko XII laser is a twelve-beam glass laser system Gekko (30 kJ, 55 TW power.) The Gekko laser has been used for ICF research, and recently, for laser astrophysics (see Section B.3).

1.4.2.4 Phebus

The Phebus laser of the Commissariat à L'Énergie Atomique in Limeil-Valenton, France, has two Nova-like glass:neodymium beams, and can deliver 4 kJ of energy at 0.35 μm to the target. Phebus is scheduled to be decomissioned in 1999. In the French laser program, Phebus is to be succeeded by LIL laser, and eventually by the Laser Megajoule, which will be similar to NIF.

1.4.2.5 NIKE

The NIKE laser [28] is a KrF laser located at the Naval Research Laboratory (NRL) in Washington, D.C. NRL participated in ICF research, and in the development of glass:neodymium lasers, from the beginning of research in both programs. NIKE produces 4–5 kJ of UV light in a 4 ns pulse. A new beam-smoothing techique suited for KrF lasers was developed for NIKE, resulting in a beam with better uniformity than existing glass lasers by a factor of about 10.

1.4.2.6 Vulcan

The VULCAN laser is located in the Laboratory of the Research Councils's Rutherford Appleton Laboratory at Chilton in Oxfordshire, UK [2]. Vulcan is a multi-beam multi-terawatt laser/matter interaction facility based on a neodymium:glass laser operating at 1.05 μm. Vulcan has both long pulse (2500 J in 1 ns) and short pulse (1 ps pulse at 35 TW) operation. The system has four experimental areas with laser radiation in various geometries including line focus and cluster. Developments are underway to enhance the output capabilities to > 200 TW in Phase I of a two phase PetaWatt enhancement program. Vulcan is one of two lasers at Central Laser Facility CCL. The other is Sprite, the worlds brightest UV laser, capable of producing intensities of 10^{19} W/cm^2 at a repetition rate of up to 15 shots per hour. Both high power lasers are used to investigate the basic physics of the interaction of laser pulses with gas and solid targets, laser fusion and X-ray laser development, and also ICF related physics.

1.5 Astrophysics experiments on large lasers

Most astrophysics experiments on lasers have been done only recently, as large intense lasers have been built. Some experimental work on large lasers predates the experiments discussed in this dissertation, and there have been other types of astrophysics experiments in the laboratory. In this section we will survey some work in laboratory astrophysics and in large laser astrophysics experiments. Because so much of the work is contemporary, and more easily described after discussing the experiments done for this dissertation, we will discuss the more contemporary work after the main body of the thesis, in Appendix B, and in particular in Sections B.1, B.2, and B.3. For an excellent review of both historical and contemporary laboratory and laser astrophysics experiments, see Ref. [59]. For further discussion of the possibilities for astrophysics experiments on large lasers and of laboratory astrophysics in general, see [131, 132, 68, 52, 72].

In [59], Drake discusses a number of historical laboratory astrophyics experiments. As Drake argues, the approach in the earlier experiments was to produce an experiment with some feature relevant to astrophysics, generally a blast wave, and then see what relevant physics could be extracted, while the goal in more contemporary experiments has been to design an experiment with a limited set of physics that can be scaled to

astrophysical scales. The first of the historical experiments which Drake discusses were performed by Borovsky *et al.* [32]. The goal in these experiments was to simulate a supernova remnant (SNR) (see Appendix A for a discussion of SNRs). The experiments were performed on the Helios laser system at Los Alamos National Laboratory. The laser delivered 6 kiloJoules (kJ) of CO_2 light at a wavelength of 10.6 μm in a 1 ns pulse to a solid spherical target a few hundred μm in diameter. Radiation from the explosion ionized the surrounding air in the target chamber, creating an ambient plasma into which the explosion ejecta expanded spherically. The experimenters hoped to detect the forward and/or reverse shock (see Appendix A) in the current of ions reaching the target chamber wall but found no evidence of either shock. One difficulty with the experiment was that large numbers of relativistic electrons were produced in the shock, and could produce hydrodynamics different than that expected in a SNR. Furthermore, in the experiment there was no background magnetic field, which is generally thought to be needed to establish a collisionless shock in SNRs.

In another set of experiments at the KI-1 facility at Novosibirsk (see for example, [7, 119, 162] and references therein), workers attempted to simulate the deceleration of an SNR blast wave. In this experiment, a CO_2 pulse delivered 0.5–1 kJ of energy in a long, 0.1 μs–0.3 μs pulse to the target. This lower intensity pulse produced lower levels of relativistic electrons. In contrast to the experiment described above, the ambient plasma was magnetized with a cylindrically symmetric magnetic field produced by magnetic coils. A θ-pinch was used to produce the ambient plasma. The magnetic field decelerated the ejecta, by $\mathbf{J} \times \mathbf{B}$ forces as electrical fields induced in the ejecta by the swept-up magnetic field interact with the background field. A forward shock was observed in measured profiles of electron density and magnetic field. As Drake notes, the deceleration observed, being due to work done to compress the magnetic field, is different in nature than the deceleration in an SNR, in which the deceleration is due to accumulation of mass. However, these experiments could potentially yield insight into the formation of collisionless shocks, which are indeed relevant in SNe (see Ref. [134]).

A third set of experiments dealt with instability of Sedov-Taylor blast waves [136]. In a spherical explosion where the ejecta sweeps up ambient matter, the Sedov-Taylor phase occurs when the mass of swept-up matter exceeds the mass of ejecta. Old SNRs enter the Sedov-Taylor phase when the SN ejecta has swept up enough of the circumstellar

medium (CSM). The experiments were performed by Grun *et al.* [75] at the Naval Research Laboratory. The goal of the experiment was to produce and observe the Vishniac instability [151], which occurs at the blast wave when the ambient matter has an effective adiabatic exponent γ less than 1.2. This can occur in SNRs when the blast wave becomes radiative (see [106]), Oscillations at the shock front can become overstable, disrupting the shell of material behind the shock if the shell is thin enough. Grun *et al.* [75] used a 5 ns, 200 J pulse of laser light at a wavelength of 1.05 μm to heat a thin plastic foil, creating high-velocity ejecta which swept up an ambient gas of nitrogen or xenon at a pressure of 5 Torr, which resulted in a Sedov-Taylor blast wave when the blast wave reached a radius of about 6 mm. After the Sedov-Taylor radius was reached, the researchers observed that the blast wave distance increased as $t^{0.4}$, as expected. Furthermore, the Vishniac theory was confirmed when strong instability at the shock front was observed for the case of xenon gas, which was radiative and had an effective γ of ≈ 1.06, and was not observed for nitrogen, which was not radiative and had an effective γ of ≈ 1.3. The relevance of these experiments to astrophysical events was considered in [106].

Rose [131, 132] also discusses a number of possible applications to astrophysics of plasmas produced by lasers. Rose discusses the use of laser-produced plasmas for identification of line spectra in the XUV; for opacity measurements relevant to Cepheid variables, for example; opacity measurments by measurement of radiation transport; direct laser heating of a plasma to test X-ray nebula modeling; dense plasma experiments relevant to white dwarfs; line transport in plasmas with strong velocity gradients; stellar opacities, relevant to the solar neutrino problem.

Budil *et al.* [35] have performed a series of experiments at the Nova laser designed to investigate the evolution of a high density sphere after the passage of a strong shock wave, thereby emulating a SN shock-cloud interaction. The interaction of strong shock waves, such as those generated by the explosion of SNe, with dense interstellar clouds is a problem of fundamental importance in the interstellar medium and may lead to the formation of a new generation of stars. In our own galaxy, the structure observed in the Cygnus Loop has been attributed to the development of hydrodynamic instabilities from such shock-cloud interactions. The researchers used the Nova laser to generate a strong ($M \sim 10$) shock wave which traveled along a miniature, beryllium shock tube, 750 μm in diameter, filled with plastic. Embedded in the plastic is a copper microsphere

(100 μm diameter) and its evolution as well as the trajectory of the shock wave were diagnosed via face-on radiography. 2D and 3D simulations of the experiment were done with an adaptive mesh refinement (AMR) code and an arbitrary Lagrangian and Eulerian (ALE) code; significant differences in the evolution were observed between the 2D and 3D simulations.

Rubenchik *et al.* [133] have investigated using the Petawatt arm of the Nova laser to study meteorite impacts. The velocity of meteorites can reach 100 km/s and higher. There is currently no facility that can accelerate a sample in the solid state up to such speeds to experimentally simulate a high velocity meteorite impact. However, for velocities larger than 10 km/s the kinetic energy density in a meteorite is much larger then the material evaporation energy, so the impact can be simulated by an impulsive, local energy release. The time of release must be smaller than the impact time and the energy must be released on a scale comparable with the meteorite size. The PetaWatt Laser at LLNL, which can deliver 500 J of energy in a $\sim$ 50 μm spot over few ps, is an ideal facility for studying high speed meteorite impact physics. Rubenchik *et al.* [133] have presented preliminary results from experiments using Petawatt to create craters in thick planar Au targets, and have discussed scaling the experimental results.

1.6 Numerical codes

In this chapter we discuss the numerical hydrodynamics codes which we have used for simulating the Nova laser experiments, SN 1987A, and SNRs.

1.6.1 HYADES

The HYADES code (see Ref. [98]) is a 1D Lagrangian code which has multigroup radiation transport and uses tabular Equation of State (EOS). We use HYADES to model the initial physics in the laser experiments. We use the measured x-ray radiation temperature, $T_r(t)$, as the energy input to HYADES.

1.6.2 CALE

The LLNL code CALE is a 2D Arbitrary Lagrangian Eulerian (ALE) code (see Ref. [16]) with tabular EOS and interface tracking; CALE allows both planar and cylindrical (r-z) geometry. The version of CALE that we have used does not have radiation transport,

although very recently we have obtained a version which does have radiation transport. We use mainly CALE to design the laser experiments, because we can use tabular EOS with CALE.

1.6.3 PROMETHEUS

PROMETHEUS is a multidimensional hydrodynamics code which uses the Piecewise Parabolic Method (PPM; see Ref. [154]). PROMETHEUS allows planar, spherical, and cylindrical geometry, and can be run in 1D, 2D or 3D.

1.6.3.1 PPM

In the PPM method, the solution to the 1D hydrodynamics equations is computed by solving the Riemann problem [49, 101] at each boundary between two zones. The historical basis for the PPM method is the Godunov method [71], in which the thermodynamic variables — density ρ, pressure P, and velocity v are approximated as constant quantities for the solution of the Riemann problem. The Van Leer second order method [45] is a higher order improvement on the first order Godunov method, in which the thermodynamic variables are approximated as linearly varying quantities within each zone. In the PPM method, the thermodynamic quantities are approximated by parabolas, giving as high as 4th order accuracy in smooth parts of the flow. An important advantage of the PPM method over more traditional finite-difference methods for computing hydrodynamic flow (see the survey in [154]) is that it naturally allows representation of shocks, often without having to use any of the artificial viscosity that other methods need to stabilize the shock. In many cases a small amount of artificial viscosity is required, but much less than in other methods. A major advantage of the PPM method is its higher order accuracy. This is particularly important in multi-dimensional calculations. The cost of a 1D finite-difference hydro calculation on a uniformly-zoned grid increases with the number of zones n as n^2, the second factor of n due to the limit on the time step imposed by the Courant condition [49] which states that information cannot travel across more than one zone during one time step. Similarly, the cost of 2D and 3D calculations go as n^3 and n^4, respectively. Thus, to double the resolution of a 2D calculation causes an 8-fold increase in the time required, and to double the resolution of a 3D calculation causes a 16-fold increase in time, making it quickly intractable to increase the resolution

of a 3D calculation. Thus it is highly desirable to use as few zones as possible.

1.6.3.2 Operator splitting and additional physics

PROMETHEUS uses operator-splitting to do multi-dimensional hydrodynamics. The hydrodynamics is calculated in 1D 'sweeps', with the first three sweeps in the x, y and z directions, and the next three in the z, y and x directions, where x, y, and z stand for whatever coordinate directions are being used in the given geometry. The entire state of the calculation is updated after the sweep. The same time step is used for each sweep in each set of three sweeps. The backwards order of the second set of sweeps produces a more accurate result, compensating for the small inaccuracy in solving operator-split 1D equations hydrodynamics instead of the fully multidimensional hydrodynamics equations.

Operator splitting can also be used to add other physics, such as diffusion by heat conduction or radiation transport, and also nuclear burning, following the method described in [114]. We investigated the effect of nuclear burning in the O layer in SN 1987A using this method (see Ch. 2.) The version of PROMETHEUS that we have used does not have radiation transport, although other workers report having successfully added to it their versions of PROMETHEUS [62].

1.6.3.3 Equation of state

Ideal gas equation of state (EOS) is used for all the PROMETHEUS simulations of the laser experiments; we choose an adiabatic exponent γ for each material in the target to best reproduce the 1D shock speed, and velocity of the interface between the materials, as simulated by HYADES and CALE using tabular EOS. In the SN and SNR simulations, we use ideal gas, $\gamma = 4/3$, which is the radiation-dominated limit of an EOS with contributions from radiation pressure and fully-ionized ideal gas.

A disadvantage of the PPM method as implemented in PROMETHEUS is that is difficult to use a fully general EOS with this method [47, 46]. The original version of the PPM method allowed only ideal gas EOS. An improvement in the Riemann solver in the PPM method [46] allowed the use of more general equations of state. We have done investigations of using tabular EOS with PROMETHEUS.

1.6.3.4 Moving grid

PROMETHEUS implements the direct Eulerian version of PPM [154, 47], in which the the new state (after the next time step) in each zone is calculated in one step onto the grid at the next time step. The other version of PPM, Lagrangian-plus-remap (LRPPM), first does a Lagrangian step, in which the grid moves with the fluid, and then remaps onto the grid at the next time step. The two different versions of PPM give very similar results [47, 66, 44]

Although the computational grid in PROMETHEUS is orthogonal, the grid lines are allowed to move in each direction, so that the state at the next time step is calculated on a new grid. This moving grid option is indispensable in many problems, especially in problems in spherical geometry, such as the SN and SNR problems (see Chapter 2 and Appendix A). In such problems the zones become very small in the angular direction at lower radius r, that is $r\mathrm{d}\theta$ and $r\mathrm{d}\phi$ can become extremely small. As a result the Courant condition can impose a very small time step in these small zones, yet the same time step must be used in all zones in the problem. In the case of a spherical explosion, roughly speaking a shell of dense material is blasted outward by the shock wave. If the entire grid can expand homologously with the blast wave or with the shell, then $r\mathrm{d}\theta$ and $r\mathrm{d}\phi$ will increase, thus allowing the time step to increase. The saving in time can be very large. Of equal importance in this case is the fact that the entire spatial extent of the problem does not have to be zoned in advance. The outer edge of the grid can be made to advance just ahead of the shock into the relatively static medium surrounding the explosion. The conditions in the surrounding medium can be fed in as a boundary condition at the high-r boundary. The saving in zones can be significant when the radius of the blast wave expands during the problem. Just enough zones can be used initially that the bulk of the material behind the shock in the problem will always be contained within the grid. At the lower radius boundary, where the fluid will typically be greatly rarefied, a flow-out boundary condition can be used. A small amount of material can be lost in this way from the problem, but the effect of this can be mitigated by first studying the problem in 1D and choosing the inner radius of the initial grid judiciously.

In the SN problems we describe (Ch. 2), we tend to have hydrodynamics in the outer part of the grid that require two dimensions or three dimensions, because the problem is

by design not spherically symmetric, such as when we place a perturbation in a fluid layer to trigger the RM and RT instabilities. However, often the innermost part of the problem is described reasonably well by 1D hydrodynamics. In such a case, it is possible to run the innermost part of the problem in 1D, by simply turning off the sweeps in the angular directions. The radial zoning can be made very coarse at lower radius, and the time step in the 1D zones can be calculated considering only the radial extent of those zones, thus removing the severe Courant condition constraint on the time step due to the small $r\mathrm{d}\theta$ and $r\mathrm{d}\phi$ in those inner zones. The effect is that the flow in the innermost regions, and its effect upon the flow further out, can be treated to perhaps a better approximation than if, the inner radius of the problem were higher and the entire problem down to this inner radius were calculated in 2D or 3D.

1.6.3.5 Radiation transport and Heat conduction

We have chosen the problems described in this dissertation so that the essential physics is the hydrodynamics, as discussed in Ch. 3. In the case of the SN, we do not address the complicated physics in the core of the star, while in the laser experiments, we are not directly concerned with the physics of energy input from the laser; we simply want to start a strong shock wave in the laser target. However, to begin a simulation of the laser problem, we do not need to do an adequate modeling of the energy input, which requires radiation transport and heat conduction. In this work we have done so using the code HYADES, described in Sec. 1.6.1. HYADES has multigroup radiation transport, and various opacity models. Below a user-set temperature threshold, HYADES can use a cold opacity table. Otherwise, HYADES can use various ionization models for the materials, such as the Saha model, and the much more expensive average atom model [98]. In modeling the laser experiments, we have tried both Saha and average atom models. We found no significant difference in the results, for our problems. HYADES also has diffusive heat conduction. In general, as evidenced by running HYADES (with radiation and heat conduction) and 1D CALE (without radiation and heat conduction) in parallel after mapping at early times from HYADES to CALE, we find that diffusion by radiation or by conduction does not significantly affect the results of the simulations.

CHAPTER 2

NUMERICAL SIMULATIONS OF HYDRODYNAMIC INSTABILITIES IN SUPERNOVA 1987A

2.1 Overview

In this chapter we present some numerical simulations of SN 1987A, performed with the code PROMETHEUS (see Section 1.6.3). Much of the material in this chapter was presented in condensed form in [92]. Many groups have performed numerical simulations of the explosion phase of SN 1987A (see eg. [8, 10, 11, 67, 115, 116, 139, 157, 77, 83, 118, 24] and references therein). Until computing power reached the point during the last ten years that 2D simulations were routinely possible, most simulations of SNe were in 1D. A 1D simulation automatically assumes a spherically symmetric explosion. However, the possibility of hydrodynamic instabilities in SN was long recognized [64, 42]. To model the mixing due to these instabilities, it was common to resort to mixing length models. However, these models generally underpredicted the peak velocities of the core elements such as ^{56}Co and underestimated the time at which these materials would become visible in the spectrum of the ejecta (see the discussion in Section 1.2 and references mentioned therein).

In [11, 67, 115], Arnett, Fryxell and Müller performed 2D simulations of the explosion in cylindrical r-z geometry. They found that by imposing a random zone-by-zone velocity perturbation of between 1–10% amplitude in the shocked fluid behind the blast wave, significant RT instability and mixing resulted. Neither these nor other 2D simulations that assume physically reasonable seed perturbations for the instabilities can reproduce the core elements velocities seen in observations of SN 1987A. The possibility remained that 3D hydrodynamic simulations could produce more mixing.

Müller, Fryxell and Arnett [116] performed preliminary three dimensional simulations of RT instabilities in SN envelopes using PROMETHEUS. The results were obtained in spherical polar coordinates (r, θ, ϕ) on an Eulerian grid of $200 \times 20 \times 20$ zones. Periodic

boundary conditions were imposed in angular direction at $\theta = \pi/2 \pm \pi/20$ and $\phi = \pm\pi/20$, respectively. The angular resolution, therefore, was 0.9 degrees. The EOS consisted of contributions from radiation and 10 Boltzmann gases (H, ^{4}He , ^{12}C , ^{16}O , ^{20}Ne , ^{24}Mg , ^{28}Si , ^{56}Fe , ^{56}Co and ^{56}Ni), which were assumed to be completely ionized, and which were used to keep track of the amount of mixing of nuclear species. The initial model was a $15M_\odot$ star near the end of core carbon exhaustion having a $4M_\odot$ He-core and a metallicity $z = z_\odot/4$ [8]. The explosion was artificially initiated by instantly depositing a mixture of internal (50%) and kinetic (50%) energy into the inner few zones. At $t = 300$ s a random perturbation of 1 to 10% amplitude was added to the radial velocity of each zone in order to get the instability started.

These preliminary three dimensional calculations showed pronounced instabilities producing clumpy structures, which had up to a factor of ten higher density than the surrounding matter. The size of the structures was limited in angular direction by the grid resolution. The overall appearance of the instability qualitatively resembled coarse 2D results obtained by the same authors on grids with similar radial and angular resolution. However, without the assumption of axial symmetry, genuine 3D clumpy structures formed. This 'similarity' of the 2D and 3D results was also found when the amount of mixing in the different models was compared (for further details see [116]).

These simulations assumed only RT instability; that is, they did not consider the shock-driven RM instability. Also, they assumed that no long-wavelength perturbations existed in the progenitor (pre-explosion) star. The work of Bazán and Arnett [13, 20] suggested that longer wavelength perturbations that could subject the O layer of SN 1987A to RM instability could exist in the progenitor. In the numerical investigations presented here, we consider the effects of single mode perturbations in the O layer of the progenitor and near the post-shock He-H interface of SN 1987A. Apart from the motivation provided by the work of Bazán and Arnett, these simple perturbations are of interest because they also admit the possibility of developing a theoretical description of the mixing based upon potential flow theory. As a first step in this development, we consider the difference between 2D and 3D hydrodynamics in the explosion. The greater instability growth expected in 3D compared to 2D is of direct interest because of the possible contributions of 3D hydrodynamics to the difference between ^{56}Co velocities in observations and those in 2D simulations.

We first examine single mode 2D and 3D growth at the O-He and He-H interfaces of SN 1987A. In the nonlinear stages of growth we expect such single mode perturbations to evolve into the familiar bubble-and-spike configurations [104, 145], by a combination of RM instability triggered by the blast wave impulse, and RT instability as the He layer decelerates the dense O layer and the H layer decelerates the He layer. We then examine the coupling between an instability at the O-He interface started by a single mode perturbation in the O layer and an instability at the He-H interface started by a random post-shock velocity perturbation in the fluid near the He-H interface. In these simulations, we deposit the canonical SN 1987A explosion energy of 1.5×10^{51} ergs at the bottom of the O layer, omitting the behavior of the Fe core. We use simply a radiation dominated ideal gas EOS, with $\gamma = 4/3$. We find in 1D simulations that the results are nearly identical in the O, He and H layers if we use fully ionized ideal gas plus radiation pressure EOS. We neglect nuclear burning. However, we have performed 1D simulations in which we have included the burning of O to the Si-Ca group elements (see Ref. [12] for discussion of nuclear burning), adding the energy released by the burning to the internal energy of the fluid. We find that the 1D hydrodynamics with and without the O-burning were nearly identical. In calculations presented here we use a moving grid that expands homologously in radius with the blast wave. We feed in the static initial model as the radial boundary condition a few zones above the shock. Except where noted, we use 'squarish' zones (dr = $r\mathrm{d}\theta$ [= $r\mathrm{d}\phi$ in 3D.]) To track the grid, we estimate the position $R_\mathrm{s}(t)$ of the shock at each time step by the location of the strong discontinuity in density, pressure and radial velocity, and estimate the shock velocity $v_\mathrm{s}(t)$ by a least squares fit to the previous m shock positions versus time, where typically we have used $m = 5$. We begin moving the grid when the shock is within n zones of the end of the grid in radius, where typically we have used $n = 8$. If the shock drifts above or below this zone, we correct the grid velocity until the shock moves back into that zone. The grid velocity for a zone at radius $r(t)$ is then simply $v_\mathrm{s}(t)r(t)/R_\mathrm{s}(t)$.

2.2 Initial model

Figure 2.1 shows a $20\mathrm{M}_\odot$ initial model (1 $\mathrm{M}_\odot = 1.99 \times 10^{33}$ g) for the progenitor of SN 1987A [12]. Figure 2.1a is a schematic of the layered structure of the initial model, and Figure 2.1b illustrates the structure of the progenitor by density, and by mass fractions

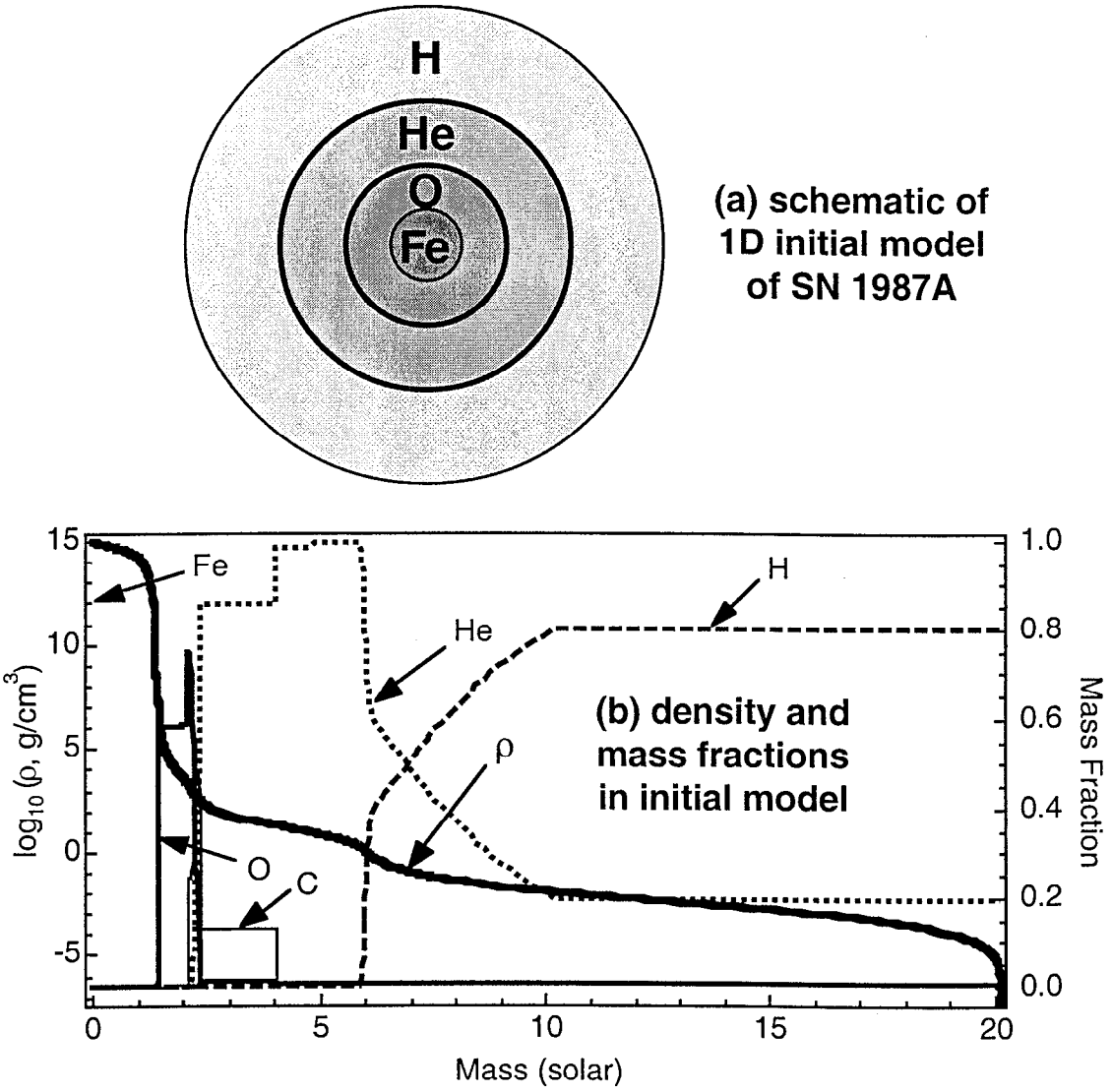

Figure 2.1: Initial model of SN 1987A from a stellar evolutionary calculation. (a) Schematic of initial model (b) Density and mass fractions of O, C, He and H vs. mass coordinate in initial model.

of O, C, He and H (designated $X_{\rm O}$, $X_{\rm C}$, $X_{\rm He}$, and $X_{\rm H}$, respectively) vs. mass coordinate. This progenitor structure is the result of a 1D stellar evolutionary calculation done by David Arnett using the code Tycho [12]. The progenitor represents the end product of $\approx 10^7$ years of evolution, during which the star has burned successively heavier and heavier elements, beginning with the burning of H and culminating with an 'onion-skin' layered structure containing a dense Fe core surrounded by successively less dense layers. The distinctions between the various layers is not sharp in terms of mass fractions of various elements, but we can distinguish three layers outside the core which are of interest to us because of the hydrodynamic instabilities which can occur at the interfaces between these layers: the O, He and H layers, listed in order outwards from the core. The 'O' layer is $\approx$ 60% O by mass, with lesser amounts of Mg, Si, Ne, C, He and H. The 'He' layer is $\approx$ 85% to almost 100 % He by mass; the lower $\approx$ 1.8 $M_\odot$ of the He layer is $\approx$ 15% C by mass. The 'H' layer is $\approx$ 80% H and 20% He by mass. There is a wide region between the He layer and the outer H envelope which is partly He and partly H. There is an overall drop in density with radius, which is to be expected for a self-gravitating sphere; for a more complete discussion, see [140], pp. 159–168, and [95, 79].

We take the O-He and He-H interfaces to be at about 2.3 $M_\odot$ and 6 $M_\odot$, respectively, in the initial model in Fig. 2.1a. The density drops steeply in the initial model at both interfaces because of changes in molecular mass across the interfaces. These drops can be understood by assuming an ideal gas law EOS with continuous pressure and temperature across an interface. Equating pressure P and temperature T across such an interface between fluids 1 and 2 of average molecular masses μ_1 and μ_2 respectively, we have $P = \rho_1 RT/\mu_1 = \rho_2 RT/\mu_2$, where R is the universal gas constant. Thus, $\rho_1/\rho_2 = \mu_1/\mu_2$. During the explosion these density drops trigger the RM and RT instabilities.

2.3 One dimensional (1D) simulations

Fe cannot be burned without consuming more energy than it releases, and so the core of the progenitor shown in Fig. 2.1 becomes unable to support itself against gravitational collapse. The star is essentially in hydrostatic equilibrium in its own gravitational field before the collapse of the core [12]. After core collapse, a strong shock moves radially out through the star, reaching the O-He interface at about 5 s, the He-H interface at about 80 s, and the surface of the star by about $t = 6 \times 10^3$ s. A strong velocity kick is imparted to

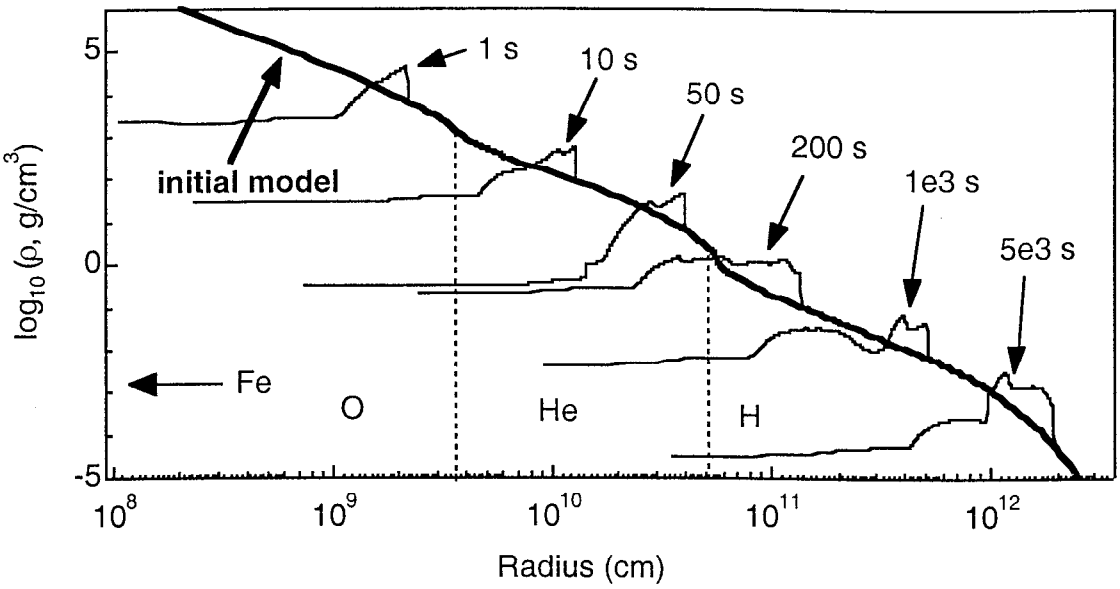

Figure 2.2: Density vs. radius in SN 1987A for initial model and at intermediate times during the explosion, from a 1D PROMETHEUS simulation.

the fluid and to each interface, and the entire ejecta expands radially. In the O, He and H layers of the star, the gravitational force of the star upon the ejecta rapidly becomes negligible as the shell expands, and deceleration of the layers due to gravity integrated over the first few hours of the explosion is negligible compared to the velocities imparted to the layers by the shock.

The mass cut (the mass coordinate below which material falls back onto the core and is accreted onto the neutron star or black hole formed by the collapsed core — see Ref. [99]) is expected to be somewhere near the bottom of the O layer. In our calculations we have ignored the small amount of material from the base of the O layer that will fall back onto the core.

Figure 2.2 shows density vs. radius in the initial model and at $t = 1$, 10, 50, 200, 1000 and 5000 s. Figure 2.3 shows density and pressure vs. radius at $t = 10$, 200, 500 and 2000 s, and Figure 2.4 shows density and velocity vs. radius at the same times. As seen in Figure 2.2 at $t = 1$ s, the blast wave is roughly a strong spherical blast wave until the shock reaches the O-He interface. At this time, the forward shock is at radius $r \approx 5 \times 10^9$ cm. At seen in Figures 2.2 and 2.3 at $t = 10$ s, the drop in density at the O-He interface in the initial model (Fig. 2.2) leads to a drop in density at the contact discontinuity

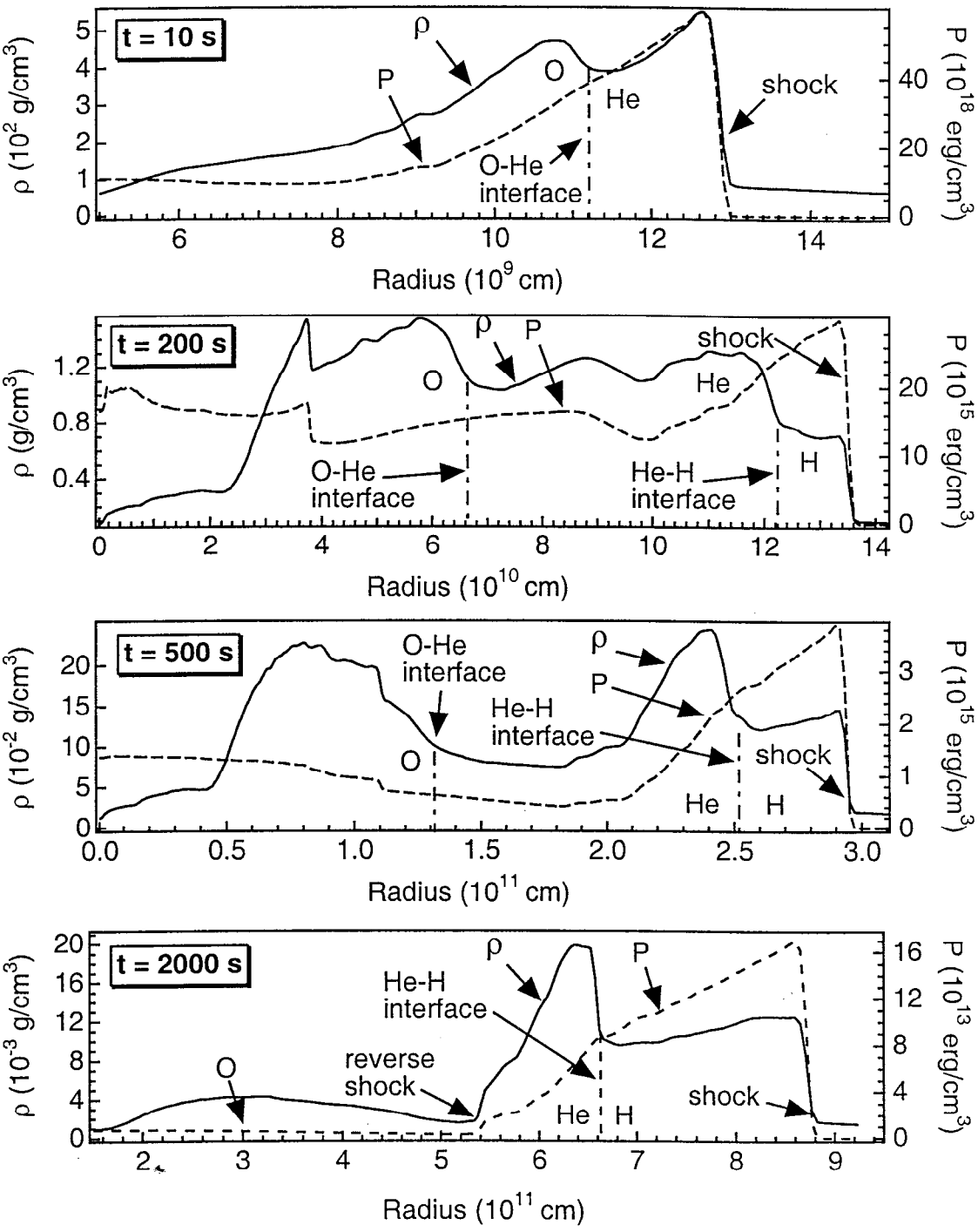

Figure 2.3: Density and pressure vs. radius in SN 1987A at $t = 10$, 200, 500 and 2000 s, from the 1D PROMETHEUS simulation.

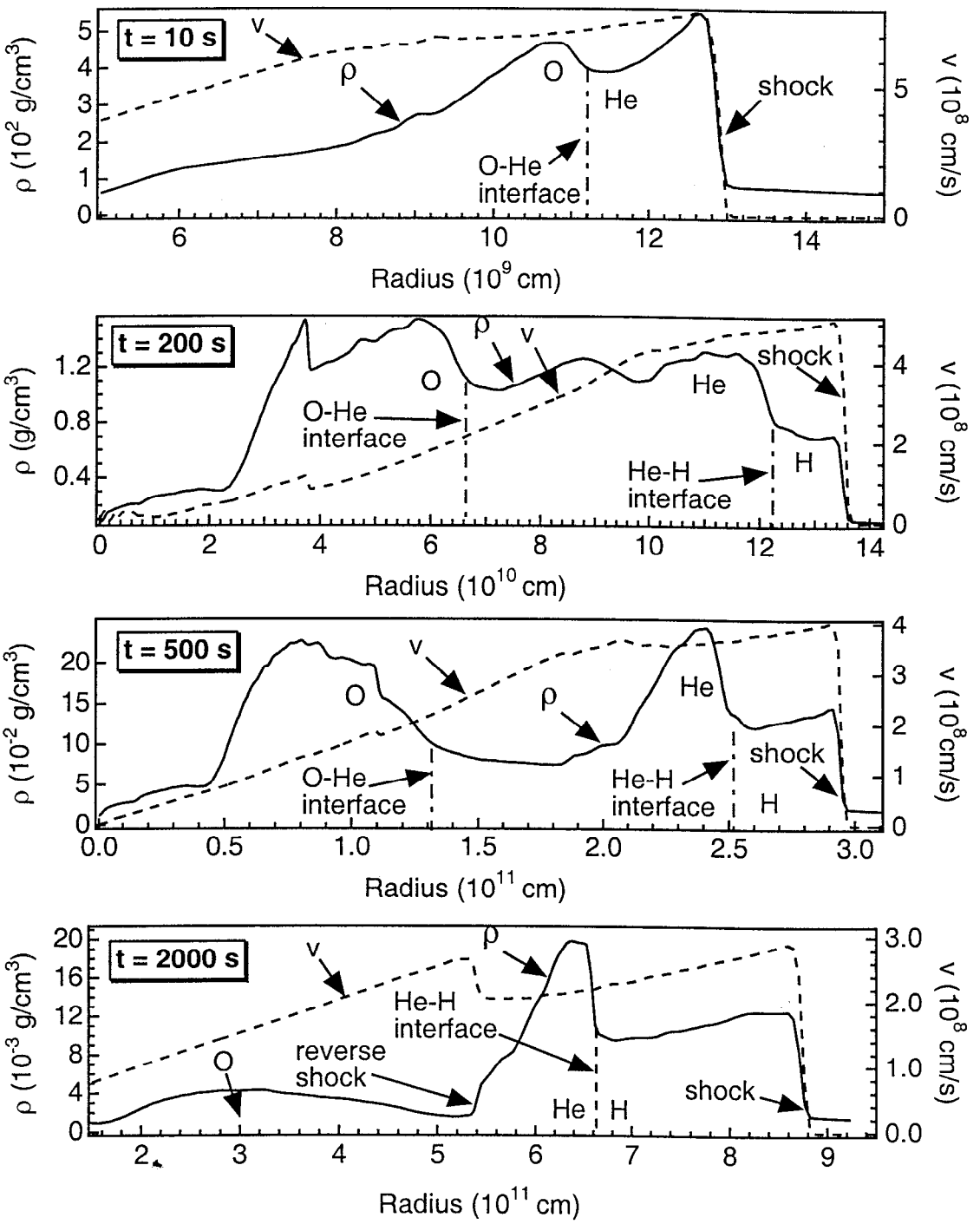

Figure 2.4: Density and velocity vs. radius in SN 1987A at $t = 10$, 200, 500 and 2000 s, from the 1D PROMETHEUS simulation.

(CD) at the O-He interface after passage of the shock. The discontinuity and shock are now at $r \approx 11.2 \times 10^9$ cm and $r \approx 12.5 \times 10^9$ cm, respectively, as seen in Figure 2.3. At this CD, the density and pressure gradients are now 'crossed' ($\nabla P \cdot \nabla \rho < 0$), with density falling sharply and pressure rising across the CD. As seen in Figure 2.4 at $t =$ 10 s, the velocity is continuous across the CD, rising towards the shock. By $t = 200$ s a second CD is evident at the He-H interface, with the density and pressure gradients crossed there. The velocity is continuous across this CD, as seen in Figure 2.3 at $t = 200$ s. At the same time, as seen in Figure 2.3 at $t = 200$ s, a rarefaction is moving back from the He-H interface to the O-He interface, as the shock accelerates into the less dense H layer, which has the effect of decompressing the fluid behind the CD and lowering the pressure in that fluid. The leading edge of the rarefaction is at $r \approx 3.8 \times 10^{11}$ cm at $t = 200$ s. At $t = 200$ s the rarefaction has not yet reached the O-He interface, and the pressure and density gradients are still crossed at that interface. A weak second shock is visible at $r \approx 3.8 \times 10^{11}$ cm; this shock first moved inward from the O layer as a reverse shock, reflected off the dense material at lower radius, and then passed outward through the O layer. This weak shock has little effect on the gross hydrodynamics. The weak shock, O-He interface, leading edge of the rarefaction, H-He interface and forward shock are at $r \approx 3.7 \times 10^{10}$ cm, $r \approx 6.6 \times 10^{10}$ cm, $r \approx 8.7 \times 10^{10}$ cm, $r \approx 12.2 \times 10^{10}$ cm and $r \approx 13.6 \times 10^{10}$ cm, respectively.

However, by $t = 500$ s, as seen in Figure 2.3, the rarefaction has moved through the O-He interface and the pressure and density gradients are now uncrossed, with both quantities falling across the O-He CD. The weak second shock is at $r \approx 11 \times 10^{11}$ cm and has weakened considerably after expanding from a lower radius. At this time there is a local pressure minimum in the He layer, so that material is accelerated towards that minimum from both the direction of the He-H interface and the O-He interface. As the material below the minimum expands radially with the ejecta, its internal energy is siphoned off into kinetic energy. As a result, by $t = 2000$ s a reverse shocks forms in the He layer. The reverse shock is visible in Figure 2.3 at $r \approx 6.8 \times 10^{11}$ cm, with density and pressure both rising across this reverse shock, and is clearly visible in Figure 2.4 by a discontinuity in velocity. The reverse shock is also visible at a later time, $t = 5 \times 10^3$ s, in Figure 2.2. The reverse shock moves through the He layer, through the O-He interface and on into the O layer.

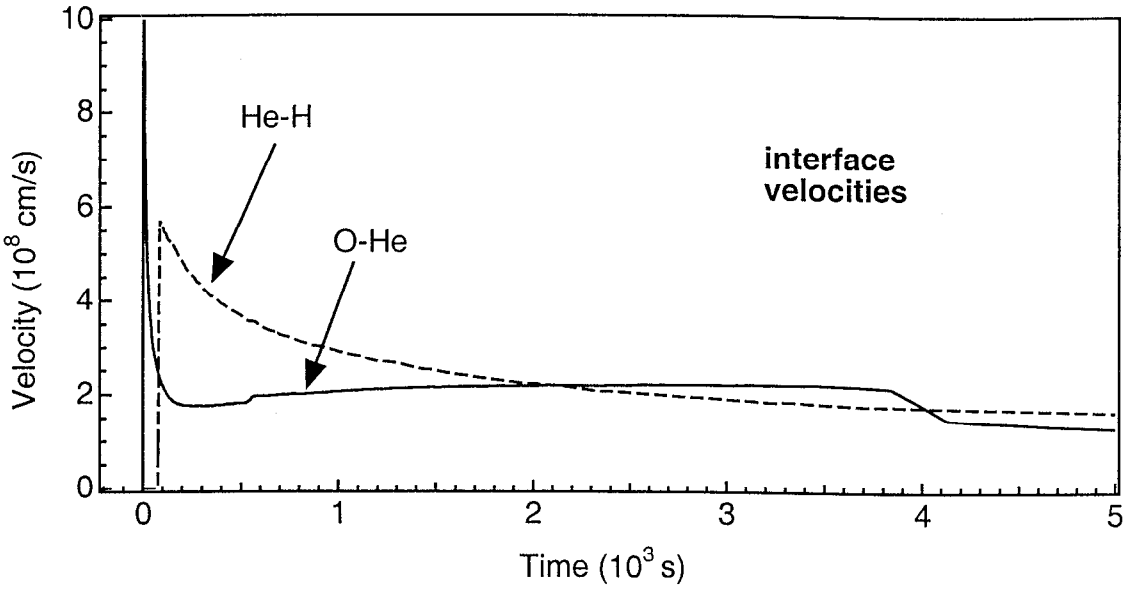

Figure 2.5: Velocity vs. time for O-He and He-H interfaces in SN 1987A, from the 1D PROMETHEUS simulation.

As the forward shock passes into the tenuous outer part of the H layer, a rarefaction moves down in radius from the H layer into the lower layers, eventually uncrossing all density gradients, at which time the ejecta is expanding homologously, with velocity proportional to radius and with density dropping off roughly as a power law with radius. The gradients remain crossed at the He-H interface until this rarefaction reaches the He-H interface.

Figure 2.5 shows the velocity of the O-He and He-H interfaces vs. time. The shock sharply accelerates the O-He interface, which then decelerates until about 200 s as the He layer slows down the O layer. After 200 s, the O-He interface is accelerated by the rarefaction. At about 600 s, the O-He interface undergoes a small further acceleration due to the weak second shock discussed above. At 4000 s, the O-He interface is sharply decelerated by the reverse shock at the base of the He layer. Meanwhile, the He-H interface is first accelerated by the shock at about 80 s, and then undergoes protracted deceleration as the He layer is slowed down by the H envelope. After 4000 s, when the passage of the reverse shock has coupled the O-He and He-H interfaces, the two interfaces decelerate together.

The sharp acceleration of the interfaces by the shock suggests that both interfaces

will be subject to the RM instability. The crossed gradients at the O-He interface before $t = 200$ s (Figure 2.3), and the deceleration of the O-He interface until $t = 200$ s (Figure 2.5) suggest that the O-He interface will be subject to the RT instability as the lighter He layer slows down the denser O layer. Similarly, the crossed gradients at the He-H interface, seen by $t = 200$ s in Figure 2.3, and the deceleration of the He-H interface after $t = 80$ s (Figure 2.5) suggest the He-H interface will be subject to the RT instability as the lighter H layer slows down the denser He layer. Each interface is expected to evolve well into the nonlinear regime [11, 67, 115]. The O layer will be decompressed by the rarefaction and then recompressed by the reverse shock, creating a potentially interesting coupling of instablities at the He-H and the O-He interfaces.

2.4 Two and three dimensional (2D and 3D) simulations

2.4.1 Single mode perturbations at the O-He and He-H interfaces

We now proceed to examine the growth of single mode 2D and 3D perturbations at the He-H interface. We take the simulated 1D conditions at $t = 400$ s, after the shock has passed the He-H interface, and map into 2D and 3D simulations. We impose single mode velocity perturbations of mode m (the number of wavelengths of the perturbation in 2π radians). The perturbation is centered in radius at the position $r = r_0$ of the He-H CD at $t = 400$ s. There is a sharp density drop at the CD at $t = 400$ s, similar to the drop seen at the CD in Fig. 2.3 at $t = 500$ s. In the angular direction θ we center the perturbation at $\theta = \theta_0 = \pi/2$ — the equator. That is, there will be a bubble or spike centered at the equator. In the present investigation we choose to have a spike at the equator, because our motivation is to study the faster ejection of the dense material in the spike (which comes from the layer initially at lower radius in the progenitor) in 3D compared to 2D, and in 3D it is computationally feasible to model only one half by one half wavelength of the perturbation. The centering in the angular direction ϕ in the 3D simulations is arbitrary since the spherical coordinate system is fully symmetric in ϕ. We use a mode number m_2 for the 2D perturbation and a mode number m_3 for the 3D perturbation which are related as described below, and give the same growth rate for the 2D and 3D perturbations in the linear regime (see Section 1.3.4.1).

For simplicity, we use a general form for the velocity perturbation which is curl-

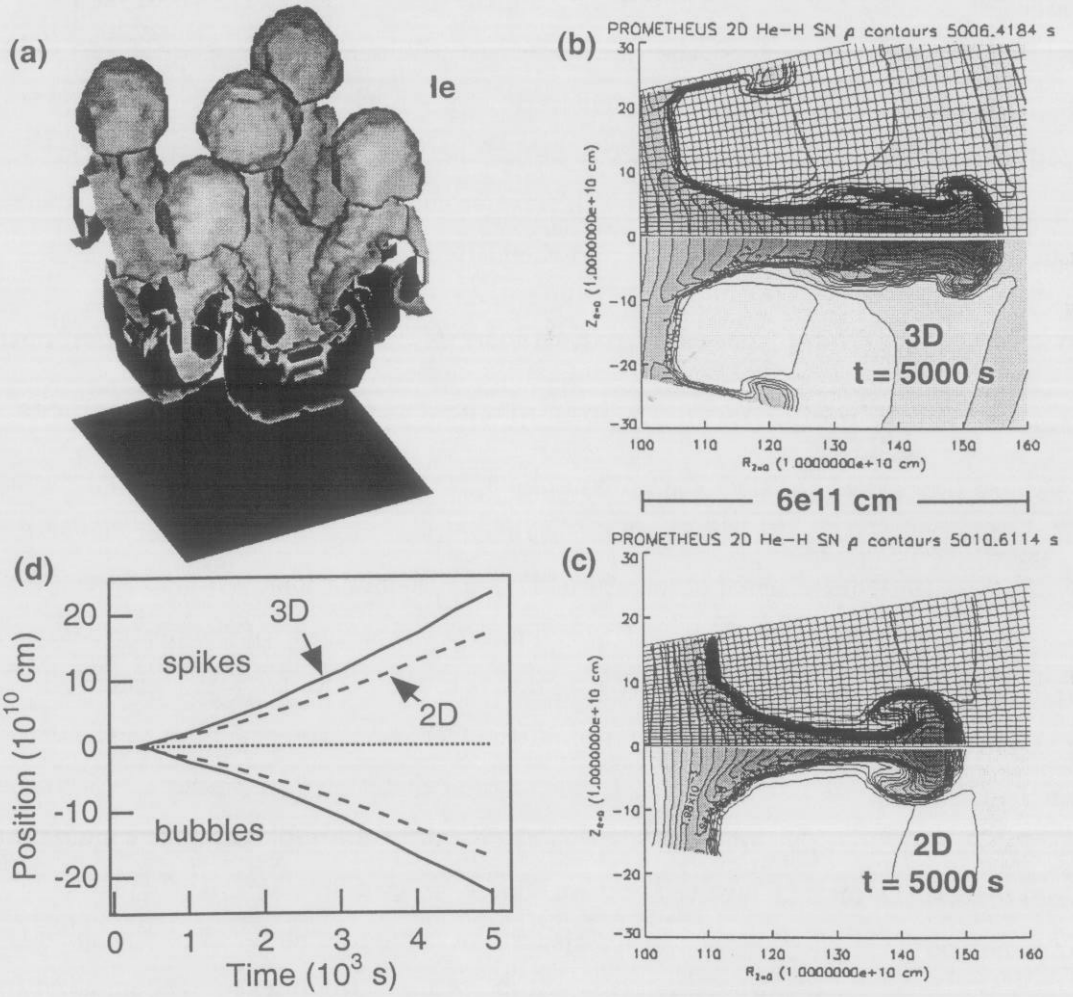

Figure 2.6: 2D vs. 3D simulations of single mode instabilities at the He-H interface of SN 1987A. (a) 3D rendering of He-H interface at $t = 5000$ s. (b) 2D slice of 3D density at $t = 5000$ s. (c) 2D density at $t = 5000$ s. (d) Bubble and spike positions vs. time.

free in the planar limit $m \to \infty$, because the hydrodynamics theories to which we refer are based upon potential theory for incompressible fluids (see Refs. [5, 81, 6] and the discussion in Section 1.3.3). The incompressible fluid approximation is applicable when the characteristic velocities (such as bubble and spike velocities) are small compared to the sound speed. The form of the 2D perturbation is (compare to Eqn. 1.15) $\mathbf{v}_2 \to \mathbf{v}_2 + \delta\mathbf{v}_2$, with

$$\begin{aligned} \delta v_{\mathrm{r},2} &= v_0 e^{-m_2|r-r_0|/r_0} \sin[m_2(\theta-\theta_0)] \\ \delta v_{\theta,2} &= \pm v_0 e^{-m_2|r-r_0|/r_0} \cos[m_2(\theta-\theta_0)], \end{aligned} \tag{2.1}$$

where v_r is the radial velocity and v_θ the tangential velocity, with the '+' sign for $r > r_0$ and the '−' sign for $r < r_0$. The form of the 3D perturbation is $\mathbf{v}_3 \to \mathbf{v}_3 + \delta\mathbf{v}_3$, with

$$\begin{aligned} \delta v_{\mathrm{r},3} &= v_0 e^{-m_3|r-r_0|/r_0} \sin[m_3(\theta-\theta_0)] \sin(m_3\phi) \\ \delta v_{\theta,3} &= \pm v_0 e^{-m_3|r-r_0|/r_0} \cos[m_3(\theta-\theta_0)] \sin(m_3\phi) \\ \delta v_{\phi,3} &= \pm v_0 e^{-m_3|r-r_0|/r_0} \sin[m_3(\theta-\theta_0)] \cos(m_3\phi) \end{aligned} \tag{2.2}$$

again with the '+' sign for $r > r_0$ and the '−' sign for $r < r_0$. We choose the amplitude v_0 of the perturbation to be some fraction of the magnitude of the radial velocity $v_r(r_0)$ of the He-H interface at $t = 400$ s. In the present investigation we choose v_0 to be 10% of $v_r(r_0)$.

We choose the 2D and 3D mode numbers m_2 and m_3 such that $2m_3^2 = m_2^2$, which means that the initial wavelength of the 3D perturbation, λ_3, and the initial wavelength of the 2D perturbation, λ_2, are in the relation $\lambda_3 = \sqrt{2}\lambda_2$. In the planar limit this choice of 2D and 3D mode numbers gives the same 2D and 3D growth rates in the linear regime (see Refs. [51, 81, 107] and see the discussion in Section 1.3.4.5). In our simulation, we chose $m = 20$.

As stated, we model one half wavelength of the perturbation at the equator. We use reflecting boundaries in θ and ϕ. This choice of boundary conditions means that the flow is not being represented with complete accuracy at the boundaries in θ, because the wavelength at the equator is not actually identical to the adjacent wavelength, since the spherical coordinate system is not symmetric in θ. However, for large enough mode number m the error should be small. We use 161 zones in the radial direction, spaced such that the zones are 'squarish' in the case of even angular zoning, ie., $r\mathrm{d}\theta = \mathrm{d}r$ and

$r\mathrm{d}\phi = \mathrm{d}r$, except at lower radius, where we use coarser radial zoning to reduce the computational expense in 3D. In simulations described later in this section, we calculated the inner part of the problem in 1D to keep the time step larger. In the simulations presented currently, we had not implemented this computational device. Thus, the coarser zoning in the radial direction did not affect the time step, since the zone widths in the angular directions, $r\mathrm{d}\theta$ and $r\mathrm{d}\phi$, are not changed. With the radial zoning chosen, the angular zoning would have been 32 zones per wavelength to give squarish zones in the 2D simulation, or 16 zones in the half wavelength modeled. In fact, we used 24 zones in the angular direction, and did not use even zoning in the angular directions, but feathered the angular zone widths inward toward the equator such that the zones were squarish at the boundaries away from the equator, but that at the equator we had $\mathrm{d}r = 2r\mathrm{d}\theta$. We did this to model the spikes better in the angular direction, because they became long and thin during the simulation.

In 3D we used the same radial zoning and the same number of zones in the angular directions, 24 zones, and the same relative feathering, with the zones at the equator and towards $\phi = 0$ being half the angular width of the zones at the boundaries away from the equator and from $\phi = 0$. Since the initial 3D wavelength was greater than the initial 2D wavelength by a factor of $\sqrt{2}$, this choice of 3D zoning meant that at the equator and at $\phi = 0$ we had $\mathrm{d}r = \sqrt{2}r\mathrm{d}\theta = \sqrt{2}r\mathrm{d}\phi$, while at the boundaries away from the equator and from $\phi = 0$ we had $\mathrm{d}r = r\mathrm{d}\theta/\sqrt{2} = r\mathrm{d}\phi/\sqrt{2}$.

In Figure 2.6 we show the results of the 2D and 3D calculations at the He-H interface. In Figure 2.6a, we show a density contour surface from the 3D calculation at 5000 s. The He spikes ('mushrooms') with Kelvin-Helmholtz 'caps' penetrating into the H along the radial direction are evident, as are the saddle lines connecting the He mushrooms and separating the H bubbles; 2D Kelvin-Helmholtz rollups occur on those saddle lines as well. In Figures 2.6b and c, we show density contour plots from the 2D and 3D calculations; the 3D plot (Fig. 2.6b) is a 2D slice through the peak of the 3D spike and the lowest point of the 3D valley.

In Figure 2.6c, we show the positions of the 2D and 3D bubbles and spikes in the rest frame of an unperturbed interface. In that frame the bubble and spike velocities are $\approx$ 20–25% faster in 2D than in 3D. We have also tried a lower amplitude perturbation, $v_0/v_r(r_0) = 0.05$ (not shown) and find about the same relative difference between 2D and

3D, although the bubble and spike grow more slowly from the smaller initial amplitude.

We have also considered density perturbations in the O layer of the progenitor; density perturbations have been shown numerically to occur in that layer [20]. In all cases, we use single mode perturbations, examining modes $m = 20$, 40 and 80. For each type of perturbation and each mode, we compare the result at the equator, where the perturbation is a 2D sinusoid of wavelength λ, to the result at the pole, where the perturbation is an axisymmetric 3D 'dimple' of radius D. We choose $D = \beta_1/\pi \times \lambda \approx 1.22\lambda$, where β_1 is the radius of the first zero of J_1 (the first derivative of the cylindrical Bessel function J_0). In the linear stage, this choice gives the same growth rate for the two perturbations [51, 141].

In one case we imposed a simple sinusoidal density modulation in θ in the pre-shock O layer. For $m = 20$, 40 and 80, in the rest frame of an unperturbed 1D interface the O spike grows 30-40% faster at the pole than at the equator. The results for $m = 20$ and $m = 40$ are shown in Figure 2.7, by contour plots of density, at $t = 80$ s and $t = 300$ s. In Figure 2.7 the O spikes are moving from left to right out into the He layer. By $t = 300$ s the rarefaction from the He-H interface has passed through the O-He interface, the O-He interface is no longer RT-unstable, and the spikes have expanded in the rarefaction. The bubble positions are very similar for the 2D simulations and for the dimple simulations at each mode number. This is because the amplitude of the initial J_0 perturbation is a damped function of angle; the amplitude of J_0 at the first zero of J_1 is only about 40% of the amplitude in the 2D perturbation at $m\theta = \pi$. In any case, our primary interest is the spike position, because the core materials are ejected in the dense outgoing spikes. On the other hand, we could also study the dimple perturbation of opposite sign, such that a bubble is formed at the pole instead of a spike. This bubble would be expected, again by the drag-vs.-buoyancy arguments, to grow faster than the 2D bubble. We have not investigated this, but it has been done for planar bubbles rising on the axes of cylindrical tubes by Layzer [100] and by Jacobs and Catton [86, 87].

We have also tried perturbations based on Fig. 7 in Ref. [20], which shows the averaged 1D density profile in the O layer of the progenitor just prior to core collapse. In that figure, there were strong density enhancements at the O-He interface and the Si-O interface. We have tried simple versions of these perturbations, which are sinusoidal in the angular direction and drop off exponentially from the O-He or Si-O interface. We find

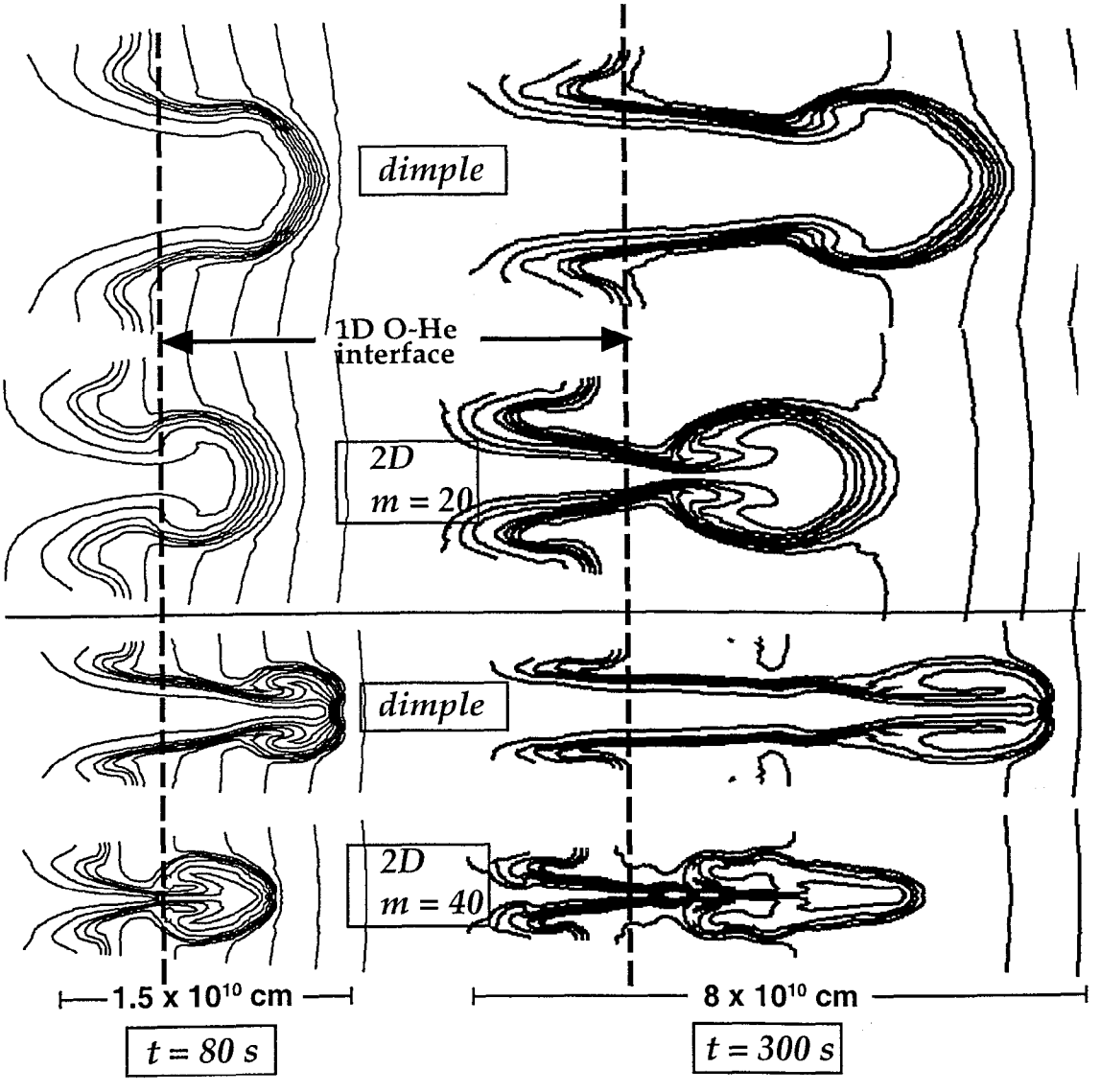

Figure 2.7: 2D vs. 3D PROMETHEUS simulations of single mode instabilities at the O-He interface of SN 1987A. Top: $m = 20$ and corresponding dimple. Bottom: $m = 40$ and corresponding dimple. Left: $t = 80$ s. Right: $t = 300$ s. Also shown is the position of a 1D (unperturbed) interface at both $t = 80$ s and $t = 300$ s, from a PROMETHEUS simulation.

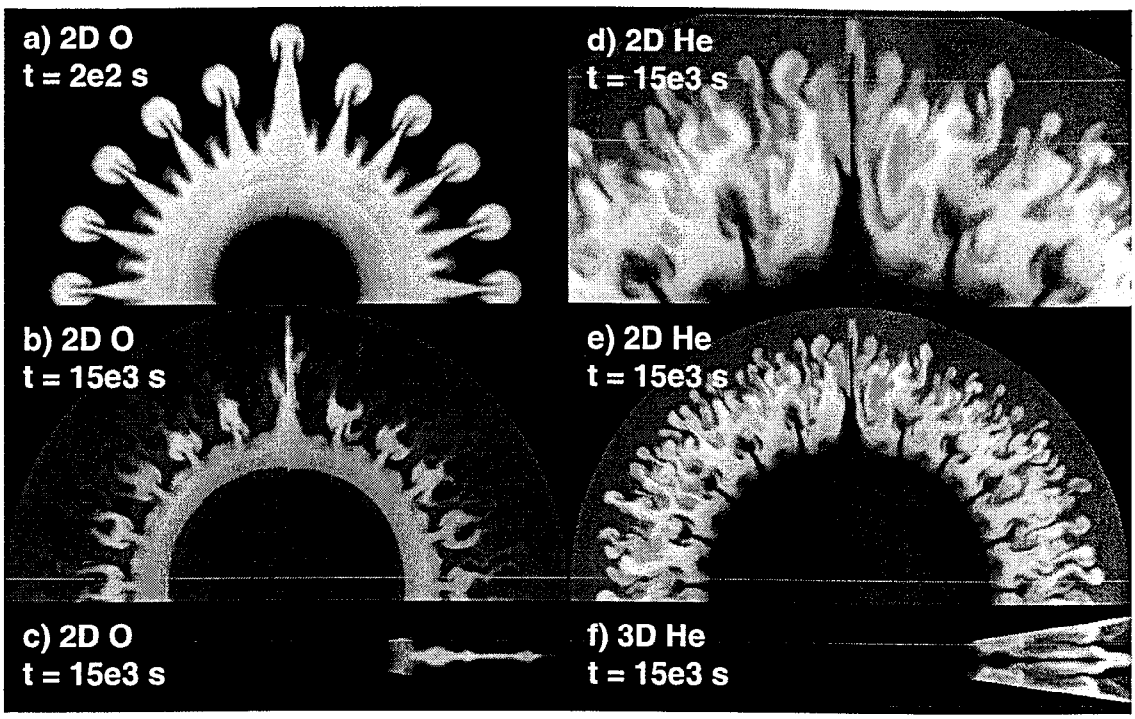

Figure 2.8: 2D and 3D PROMETHEUS simulations showing coupled hydrodynamic instability growth at the O-He and He-H interfaces of SN 1987A. (a) 2D: mass fraction of O at t = 200 s. Bar is 1.2 $\times 10^{10}$ cm long. (b) The same, at $t = 1.5 \times 10^3$ s. Bar is 3.6 $\times 10^{12}$ cm. (c) 3D: O at $t = 1.5 \times 10^3$ s. Same scale as part b. (d,e) 2D: mass fraction of He at $t = 1.5 \times 10^3$ s. Part d is a closeup of part e at the pole. Part e: same scale as part b. (f) 3D: He at $t = 1.5 \times 10^3$ s. Same scale as parts b,c,e.

that the perturbation at the Si-O interface produces very weak instability growth. The perturbation at the O-C interface produces somewhat stronger growth, but much weaker than the case we describe above, in which we have perturbed the density in most of the O region. The simulations suggest that perturbations throughout the O layer would be needed to produce strong hydrodynamic instability growth in the O layer and at the O-He interface.

2.4.2 Coupled instabilities at the O-He and He-H interfaces

The rarefaction and the reverse shock (see the discussion in Section 2.3) transmit information from the He-H interface back to the O-He interface. Hence, we next consider the effect of coupling on the instability evolution at the O-He and He-H interfaces. We impose a sinusoidal density perturbation in θ of mode $m = 20$ and 10% amplitude in the O layer

of the initial model. After the shock passes the He-H interface, we perturb the radial velocity in the fluid near the He-H interface, with a random zone-by-zone perturbation of amplitude 10%.

In Figs. 2.8a–b and 2.8d–e we show the results of a 2D calculation of π radians of the star, from $\theta = -\pi/4$ to $\theta = 3\pi/4$, so that a $\pi/2$ cone around the pole is modeled, as well as a $\pi/2$ wedge around the equator; in these figures we have reflected the simulation to produce the images shown. We use 480 zones in the θ coordinate direction (48 zones per wavelength of the O perturbation.) At lower radius we calculate only in 1D in the radial direction, to avoid the timestep limits imposed by the Courant condition. Figures 2.8a and 2.8b show oxygen mass fraction ($X_{\rm O}$) at t = 200 s and at $t = 1.5 \times 10^3$ s. Figures 2.8d and 2.8e show $X_{\rm He}$ at $t = 1.5 \times 10^3$ s; Fig. 2.8d is a blowup of the image in Fig. 2.8e near the pole. The perturbation in the O layer produces a strong growth of bubbles and spikes at the imposed mode; this pattern persists through the subsequent rarefaction and the recompression by the reverse shock. The random velocity perturbation leads to a complicated bubble-and spike structure at the He-H interface.

The axisymmetric 3D O spike at the pole grows significantly larger than the 2D spikes (ridges) away from the pole. A similar difference at the pole was noted in [118]. The difference appears greater at later times, perhaps due to coupling of the instabilities at the two interfaces. In Figs. 2.8d and 2.8e we can see the dark areas where the O spikes have penetrated the He layer; the dark area at the pole is considerably more pronounced. The O spike has penetrated through the He layer into the H layer, while the 2D ridges do not reach the He-H interface.

The converging grid at the pole may cause the flow to be represented inaccurately there; to check the 3D effect further we have done 3D calculations at the equator, where the grid does not converge, using a 'crosshatch' density perturbation (sinusoidal in both angular directions) in the O layer. First, we modeled 1.5×1.5 wavelengths at low resolution (not shown), with half of one spike next to the equator, and a full spike adjacent to it. We used reflecting boundary conditions in the angular directions. The two resulting O spikes grew strongly in the radial direction and looked similar to each other. Since the spike adjacent to the equator was not constrained from 'tipping over' in either angular direction, this first 3D simulation suggested that a reasonable result could be obtained at higher resolution by modeling only one-half of one spike at the equator, that is, half

a wavelength in each angular direction. Thus, we modeled 0.5×0.5 wavelengths at the same resolution as the 2D calculation shown in 2.8a–b. Fig. 2.8c and 2.8f show the results for the 3D calculation. We have reflected the image around the equator for clarity. The 3D O spike at the equator grows as strongly as the polar spike in the 2D calculation shown in Fig. 2.8a–b. The He layer is considerably perturbed by the O spike, as seen in Fig. 2.8f, and the He bubble appears to grow more strongly in 3D. These 3D calculations are suggestive of a significant 3D effect; it would be very useful to repeat them at higher resolution to see if the results converge. The 0.5×0.5 wavelength simulation took about 200 CPU hours on a 540 MHz CPU.

The greater penetration of the 3D over the 2D O spikes is not enough to account for the difference in ^{56}Co velocities between observations of SN 1987A and 2D simulations. However, our results suggest a distinctly different hydrodynamic evolution in 3D vs. 2D for SN 1987A, at least for the single mode density perturbations in the O layer which we have studied. Fluid from the O layer may penetrate considerably further in 3D than in 2D, and the overlying He layer may be ruptured and fragmented much earlier in 3D than in 2D.

Fully multimode perturbations in the O layer could potentially yield different growth in both 2D and 3D than we see with these single mode perturbations. Bazán [19] has recently begun using the massively parallel Accelerated Strategic Computing Initiative (ASCI) machines at LLNL to study multimode perturbations in SN 1987A in 2D and 3D. Early results show an approximately 30% enhancement in growth rates in 3D vs. 2D.

CHAPTER 3

SCALING HYDRODYNAMICS

3.1 Overview

In this chapter we discuss the scaling of hydrodynamics from the intermediate stages of a core-collapse supernova explosion to the microscopic scales of the Nova laser experiments. We are able to do the scaling because in both situations we have 'pure' hydro, described by the compressible Euler equations. As a result, there a simple tranformations which allow us to do the scaling.

3.2 Compressible hydrodynamics— laser to supernova

3.2.1 Pure hydro at intermediate times

We can rigorously transform the hydrodynamics at the microscopic scale of a laser experiment to the astronomical scale of a SN. We can do so because in both cases, the hydrodynamics is described by equations which scale from one regime to the other. Both the laser experiment and the SN at intermediate times (the first few hours) are described by compressible hydrodynamics equations — the Euler equations. This is true because in both cases, the plasmas are collisional (particles are localized on small scales), viscosity is unimportant (inertial forces are much greater than viscous forces), thermal conduction is negligible (compared to advection of heat), and radiation transport effects are negligible (again, compared to advection of heat.) For a more complete discussion of these criteria, see Ref. [134], and for additional discussion of scaling see Refs. [93, 38, 6, 81].

Briefly, let h, v and τ be a typical scale length, fluid velocity, and time scale for either regime. The plasmas are collisional because the ratio ℓ_c/h is small, where ℓ_c is the collisional mean free path; for the SN, $\ell_c/h < 5 \times 10^{-12}$, and for the laser, $\ell_c/h < 7 \times 10^{-6}$. Viscosity is unimportant because the Reynolds number $\mathrm{Re} \equiv hv/\nu$ is very large ($\gg 10^3$), where ν is the dominant viscosity. For the SN, photon viscosity dominates and $\mathrm{Re} > 10^{12}$; for the laser experiment, ion viscosity dominates and $\mathrm{Re} > 2.5 \times 10^5$.

Thermal conduction is negligible because the Peclet number $\mathrm{Pe} \equiv hv/\chi \gg 1$, where χ is the thermal diffusivity. In both cases, magnetic fields are unimportant and χ is the thermal diffusivity for unmagnetized electrons. For the SN, $\mathrm{Pe} > 10^{11}$; for the laser experiment, $\mathrm{Pe} > 1.3 \times 10^4$. That radiation transport is unimportant in both cases can be seen by considering either the photon Peclet number $\mathrm{Pe}_\gamma \equiv hv/\chi_\gamma$ where χ_γ is the thermal diffusivity for photons, or the ratio τ_R/τ, where τ_R is the radiation cooling time. For the SN, $\mathrm{Pe}_\gamma > 4 \times 10^5$; for the laser experiment, $\tau_\mathrm{R}/\tau > 4 \times 10^3$.

To support these assertions with greater detail, we will roughly follow the discussion in Ref. [134], but for simplicity establish only conservative bounds on the quantities mentioned. Note that we use cgs units, except that we used energy units (eV) for temperature T, which makes Boltzmann's constant k_B equal to one. For the arguments regarding collisionality, we use Equation 9 in [134]

$$\frac{\ell_\mathrm{c}}{h} \approx 3 \times 10^{13} \frac{T(\mathrm{eV})^2}{\Lambda h n_\mathrm{i}} \tag{3.1}$$

where Λ is the Coulomb logarithm and the ion-ion mean free path for hydrogen from Braginski [33] has been used (the exact mean-free path is only important if this collisionality condition is marginal). We can take $\Lambda \gtrsim 1$ (being conservative.) Let us now apply equation 3.1 to the case of SN 1987A. At $t = 2000s$, the EOS is radiation-dominated and we can conservatively take $T < 10^3$ eV. We will take the scale length $h \approx 10^{11}$ cm to be the width of the dense part of the He layer (see Figure 2.3). Making a conservative underestimate of n_i, we take $n_\mathrm{i} = \rho/Am\mathrm{H}$, where $A < 10$ is the atomic number. Thus,

$$(\ell_\mathrm{c}/h)_\mathrm{SN} \lesssim 3 \times 10^{13} \cdot \frac{T(\mathrm{eV})^2 A \cdot 1.67 \times 10^{-24}}{10 \cdot h\rho} < 3 \times 10^{13} \cdot \frac{10^3 \cdot 10 \cdot 1.67 \times 10^{-24}}{10 \cdot 10^{11} \cdot 10^{-3}} \tag{3.2}$$

$\approx 5 \times 10^{-12}$.

Similarly, for the case of the laser experiment at $t = 20$ ns, we take $T(ev) \lesssim 10$ eV, $p \gtrsim 1$ g/cm^3 (see Figure 4.7.), take $h \approx 50\mu$m to be the thickness of the dense part of the Cu layer, and $A < 70$ (for Cu). Thus,

$$(\ell_\mathrm{c}/h)_\mathrm{expt} \lesssim 3 \times 10^{13} \cdot \frac{1^2 \cdot 70 \cdot 1.67 \times 10^{-24}}{10 \cdot 50 \cdot 10^{-4} \cdot 1} \tag{3.3}$$

$\approx 7 \times 10^{-6}$.

For the photon viscosity in the SN, we use equation 26 from [134],

$$\nu_\mathrm{rad}(\mathrm{cm}^2/\mathrm{s}) \sim \bar{\ell} c \sigma T^4/(\rho c^3) \approx 3 \times 10^{-9} \cdot \frac{A}{Z} \frac{[T(\mathrm{eV})]^4}{[\rho(\mathrm{g/cm}^3)]^2}\ \mathrm{cm}^2/\mathrm{s}$$

$$\gtrsim \; 3 \times 10^{-9} \cdot 2 \cdot [10^3]^4 \cdot 10^{-3} = 6 \times 10^6 \text{ cm}^2/\text{s} \tag{3.4}$$

which gives

$$\text{Re}_{\text{SN}} = \frac{hv}{\nu} = \frac{10^{11} \cdot 10^8}{6 \times 10^6} > 10^{12}, \tag{3.5}$$

$v = 10^8$ cm/s being a typical velocity in the SN.

For unmagnetized ion viscosity in the laser experiment we use equation 27 from [134],

$$\nu_{\text{i}}(\text{cm}^2/\text{s}) \;=\; 3.3 \times 10^{-5} \cdot \frac{\sqrt{A}[T(\text{eV})]^{5/2}}{\Lambda Z^4(\text{g/cm}^3)} < 2 \times 10^{-3} \text{ cm}^2/\text{s} \tag{3.6}$$

which gives

$$\text{Re}_{\text{expt}} = \frac{hv}{\nu} > \frac{50 \times 10^{-4} \cdot 10^5}{2 \cdot 10^{-3}} = 2.5 \times 10^5, \tag{3.7}$$

10^5 cm/s being a typical velocity in the laser experiment.

For heat conduction, we use equation 11 from [134],

$$\chi(\text{cm}^2/\text{s}) \;=\; 3.3 \times 10^{-3} \cdot \frac{[T(\text{eV})]^{5/2}}{\Lambda Z(Z+1)\rho(\text{g/cm})^3} \tag{3.8}$$

For a conservative underestimate of the Peclet number, we make a conservative overestimate of χ, taking $\Lambda = 1$. In the case of the SN, we take $Z(Z+1) \geq 2$, obtaining

$$\chi_{\text{SN}} \;<\; \frac{3.3 \times 10^{-3} \cdot (10^3)^{5/2}}{2 \cdot 10^{-3}} \text{ cm}^2/\text{s} = 1.65 \times 10^{7.5} \text{ cm}^2/\text{s} \tag{3.9}$$

$$\text{Pe}_{\text{SN}} \;>\; \frac{hv}{\chi} > \frac{10^{11} \cdot 10^8}{1.65 \cdot 10^{7.5}} > 10^{11} \tag{3.10}$$

In the case of the laser experiment, we take $Z(Z+1) \geq 2.67 \cdot (2.67+1) > 9$ (for CH_2).

$$\chi_{\text{expt}} \;<\; \frac{3.3 \times 10^{-3} \cdot 10^{5/2}}{9} \text{ cm}^2/\text{s} = 0.037 \text{ cm}^2/\text{s} \tag{3.11}$$

$$\text{Pe}_{\text{expt}} \;>\; \frac{hv}{\chi} > \frac{50 \times 10^{-4} \cdot 10^5}{0.037} > 1.3 \times 10^4 \tag{3.12}$$

For radiation transport in the SN, we use equation 18 in [134] for the radiation contribution to the thermal diffusivity χ_γ in the case where the mean free paths of photons, $\bar{\ell}$ is much less than the scale length h, that is

$$\chi_\gamma = \kappa_\gamma / c_{\text{V}} \tag{3.13}$$

with the radiative thermal conductivity κ_γ and thermal capacity per unit volume c_{V} given by

$$\kappa_\gamma \;=\; \frac{16}{3}\bar{\ell}\sigma T^3 \tag{3.14}$$

$$c_{\text{V}} \;=\; \frac{16\sigma T^3}{c} + \frac{3(Z+1)n_{\text{i}}}{2} = \frac{16\sigma T^3}{c} + 8.98 \times 10^{23} \cdot \frac{(Z+1)\rho}{A} \tag{3.15}$$

where the first term is the thermal capacity of the radiation and the second term is the thermal capacity of the electrons and ions. Here, the mean free path of the photons $\bar{\ell}$ is taken to be the $\min(\bar{\ell}_{\rm brems}, \bar{\ell}_{\rm Thomson})$. The mean free path $\bar{\ell}_{\rm brems}$ due to inverse bremsstrahlung averaged over a Planckian distribution of photons (the Rosseland mean) in a fully ionized plasma ([134], Eqn. 16) is

$$\begin{aligned}
\bar{\ell}_{\rm brems} &= 4.6\times10^{11}\cdot\frac{A^2[T({\rm eV})]^{7/2}}{Z^3[\rho({\rm g/cm^3})]^2} < 4.6\times10^{11}\cdot\frac{(3Z)^2[T({\rm eV})]^{7/2}}{Z^3[\rho({\rm g/cm^3})]^2} \\
&= 4.6\times10^{11}\cdot\frac{9\cdot T({\rm eV})}{Z[\rho({\rm g/cm^3})]^2} < 4.6\times10^{11}\cdot\frac{9\cdot(10^3)^{7/2}}{1\cdot(10^{-3})^2}\ {\rm cm} \\
&= 1.3\times10^{8}\ {\rm cm}
\end{aligned} \tag{3.16}$$

where we have overestimated $\bar{\ell}_{\rm brems}$, so that we overestimate κ_γ and χ_γ and thus conservatively underestimate ${\rm Pe}_\gamma$. The mean free path $\bar{\ell}_{\rm Thomson}$ with respect to Compton scattering is, using equation 17 in [134],

$$\bar{\ell}_{\rm Thomson} = [n_{\rm e}({\rm cm^{-3}})\sigma_{\rm T}({\rm cm^2})]^{-1} = \frac{2.5A}{Z\rho({\rm g/cm^3})}({\rm cm}) < \frac{2.5}{10^{-3}}({\rm cm}) = 2.5\times10^3\ {\rm cm} \tag{3.17}$$

where $\sigma_{\rm T} = (8\pi/3)r_{\rm e}^2 = 6.6\times10^{-25}$ cm^2 is the Thomson cross-section, $n_{\rm e}$ is the electron density, and ρ is the mass density. Thus, $\bar{\ell} = \bar{\ell}_{\rm Thomson} = 2.5\times10^3$ cm.

When radiation pressure dominates, the first term in Equation 3.14 for $c_{\rm V}$ dominates: with $k_{\rm B} = 1$ we have $\sigma = 1.56\times10^{59}$ erg cm^{-2} s^{-1} eV^{-4} and the first term is

$$\frac{16\cdot1.56\times10^{59}\cdot(10^3)^3}{3\times10^{10}}\ {\rm erg\ cm^{-3}\ eV^{-1}} = 2.77\times10^{53}\ {\rm erg\ cm^{-3}\ eV^{-1}} \tag{3.18}$$

while the second term is

$$\frac{3(Z+1)\cdot\rho}{2Am_{\rm H}} \lesssim \frac{9\cdot10^{-3}}{2\cdot1.67\times10^{-24}}\ {\rm erg\ cm^{-3}\ eV^{-1}} = 2.69\times10^{21}\ {\rm erg\ cm^{-3}\ eV^{-1}} \tag{3.19}$$

Thus, Equation 3.13 simplifies to

$$\chi_\gamma = \frac{\bar{\ell}c}{3} = \frac{\bar{\ell}_{\rm Thomson}c}{3} < \frac{2.5\times10^3\cdot3\times10^{10}}{3}\ {\rm cm^2\ s^{-1}} = 2.5\times10^{13}\ {\rm cm^2\ s^{-1}} \tag{3.20}$$

and finally

$${\rm Pe}_\gamma = \frac{hv}{\chi_\gamma} > \frac{10^{11}\cdot10^8}{2.5\times10^{13}} = 4\times10^5 \tag{3.21}$$

For the laser experiment, we calculate the blackbody radiation cooling time $\tau_{\rm BB}$ (plasma energy content divided by blackbody radiation flux) using Equation 22 in Ref.

[134]:

$$\tau_{\rm BB}({\rm s}) \;=\; 0.7\cdot\frac{(Z+1)\rho h}{A[T({\rm eV})]^3} \gtrsim \frac{1}{2}\frac{1\cdot 50\times 10^{-4}}{10}({\rm s}) = 1.75\times 10^{-4}{\rm s} \qquad (3.22)$$

Thus, $\tau_{\rm BB}/\tau = 1.75\times 10^{-4}/(20\times 10^{-9}) > 4\times 10^3$.

3.2.2 Scaling the Euler equations

The Euler equations (see Section 1.3.2),

$$\begin{aligned}
\frac{\partial}{\partial t}\rho &+ \nabla\cdot(\rho\mathbf{v}) = 0\\
\frac{\partial}{\partial t}(\rho\mathbf{v}) &+ \nabla\cdot(P\tilde{\mathbf{I}}+\rho\mathbf{v}\mathbf{v}) = \rho\mathbf{g}\\
\frac{\partial}{\partial t}(\rho E) &+ \nabla\cdot[(\rho E+P)\mathbf{v}] = \rho\mathbf{v}\cdot\mathbf{g}
\end{aligned}$$

where

$$E = u + \frac{1}{2}v^2,$$

u being the internal energy, are invariant under any scale transformation that preserves the quantity (space/time) $\times$ (density/pressure)$^{1/2}$, ie.,

$$\begin{aligned}
\rho &= a\cdot\rho_1\\
P &= b\cdot P_1\\
h &= c\cdot h_1\\
\tau &= (a/b)^{1/2}c\tau_1
\end{aligned} \qquad (3.23)$$

where h is a typical scale length, and a, b and c are constants. We assume here that in the regimes of interest, the equations of state are modeled reasonably well by polytropic gas laws with comparable adiabatic exponents (for further details, see Ref. [134].)

3.2.3 Scaling supernova to laser

We now apply the scaling transformation, Eqn. 3.23, to the regimes of the SN simulated in Ch. 2 and the the two-layer laser experiment described in Ch. 4. Our goal here is to establish an order-of-magnitude correspondence between characteristic quantities at particular intermediate times from each regime. We will consider the SN at $t = 500$ s (Figure 2.3), and the laser experiment at $t = 10$ ns (Figure 4.4). At these times the

evolution of the He and H layers in the SN appears analogous to the evolution of the Cu and CH_2 layers in the laser experiment. We will take the time scale τ_1 to 500 s, and determine what time interval this corresponds to in the laser experiment, that is, the time interval in which we expect to see similar scaled hydrodynamic evolution, for example, similar scaled growth of bubbles and spikes. At the He-H interface, we have $\rho_1 \approx 12 \times 10^{-2}$ g/cm^3 and $P_1 = 2 \times 10^3$ Mbar. We will take the scale length h_1 to be the width of the dense part of the He layer: $h_1 = 4 \times 10^{10}$ cm. In the compressible laser experiment at 10 ns at the Cu-CH_2 interface we have $\rho = 1$ g/cm^3 and $P = 1$ Mbar. We take the scale length h to be the width of the dense part of Cu layer: $h = 40\ \mu\text{m} = 40 \times 10^{-4}$ cm.

Now we use the transformation in Eqn. 3.23 to find the remaining undetermined quantity, τ. First we determine the constants of the transformation. We find that $a = \rho/\rho_1 = 8.33$, $b = P/P_1 = 5 \times 10^{-4}$, and $c = h/h_1 = 1 \times 10^{-13}$. Thus the density, pressure and spatial scales differ by 1, 4 and 13 orders of magnitude, respectively, at the chosen times. Applying the transformation, we find that a typical hydrodynamic time τ is $(8.33/5 \times 10^{-4})^{1/2} \cdot 10^{-13} \cdot 2 \times 500$ s ≈ 6.5 ns, which is indeed an appropriate time scale for instability growth in the laser experiment at intermediate times. Thus for the case of compressible hydrodynamics described by the Euler equation, we can scale the hydrodynamics from the laser experiment to the SN.

CHAPTER 4

SUPERNOVA EXPERIMENTS ON THE NOVA LASER

4.1 Overview

As a first experimental step, we have designed and shot targets at the Nova laser which are analogs to the He and H layers of SN 1987A. The targets have two layers of different densities. The laser is used to send a strong shock through the denser layer, through the interface between the two layers and on into the less dense layer. Controlled perturbations are placed in the initial target at the interface, and these perturbations give rise to RM and RT instabilities. In these first experiments, the geometry of the target is planar. We use the code HYADES and the LLNL code CALE to test designs for the targets. We then simulate the experiments using the SN code PROMETHEUS, and compare the results of the simulations to the data from the experiment. Thus we use the experiments to benchmark the hydrodynamics of PROMETHEUS.

4.2 Experiment and target

The experimental configuration is illustrated in Fig. 4.1. For discussions of the Nova laser and the experimental techniques, see Section 1.4.1 and Refs. [69, 57, 34, 121] and references therein. For a discussion of the framing camera, see [36]. Eight of the ten Nova laser beams at a wavelength of $\lambda_L = 0.351\,\mu$m, energy of 1.5 kJ/beam, and duration of 1 ns are focused into a 3.0 mm long, 1.6 mm diameter Au hohlraum (cylindrical radiation cavity,) converting to an $\sim$190 eV, approximately thermal x-ray drive. The experimental package is shown in Figure 4.2. The package is planar: an 85 μm thick Cu ($\rho = 8.9$ g/cm) foil backed by 500–600 μm of CH_2 ($\rho = 0.95$ g/cm). A sinusoidal ripple ('corrugation') of wavelength $\lambda = 200$ μm and amplitude $\eta_0 = 20$ μm, is imposed at this embedded interface, by machining the surface of the Cu before the CH_2 is added. The package is mounted across a $750\,\mu\text{m} \times 750\,\mu\text{m}$ diameter hole in the hohlraum wall, so that the inner, flat surface of the Cu sees the x-ray drive. The Cu is ≈ 800 μm $\times$ 800 μm in the directions

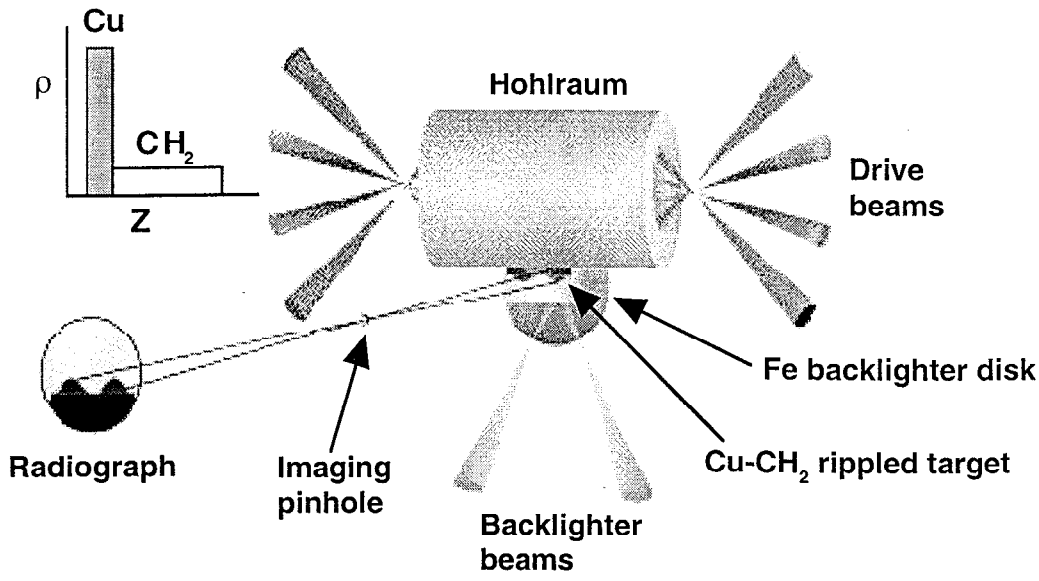

Figure 4.1: Experimental configuration

parallel to the unperturbed interface. We concentrate on the data in the middle 400 μm of the target in these directions; this section of the target contains 2 wavelengths of the initial perturbation. The edges of the target on the sides are free, so that eventually the target decompresses in the lateral direction, after the edges of the shock reach the edges and a rarefaction comes back into the target. However, this does not happen until at least 40 ns, by which time we have stopped taking data. The edges of the target can bow and curl as the shock reaches them. Potentially the material at the edge of the target can curl up into the line of sight of the diagnostics. However, the amount of material is small. Also, we make the CH_2 layer wider in the lateral directions than the Cu, so that it slows down the Cu from the edges.

As the x-ray drive heats the inner surface of the Cu, Cu is ablated from the Cu surface in a rocket-like blowoff. At the same time, a strong planar shock is launched into the Cu. As the shock crosses the Cu-CH_2 interface, it triggers the RM and RT instabilities at the interface, leading to the growth of ridge-like 2D spikes of Cu and trough-like 2D

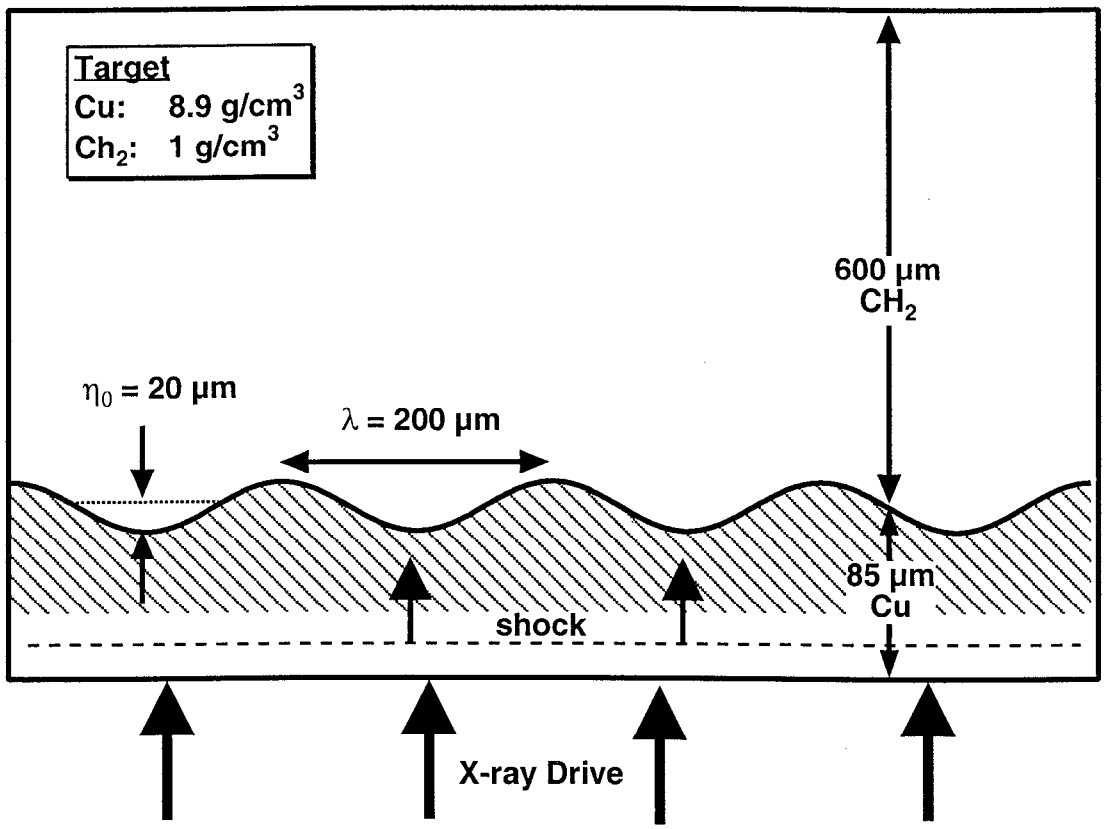

Figure 4.2: Target for Nova experiment with 2D sinusoidal material perturbation.

ridges of CH_2 between the spikes. To diagnose the growth of these bubbles and spikes, we use side-on radiography (see the discussion in Section 1.4.1). Two Nova beams at $\lambda_L = 0.528\,\mu$m, energy of 3 kJ, and duration of 5 ns are focused onto a backlighter disk, which is a separate disk of Fe, offset from the target. The backlighter disk generates He-α x-rays at 6.7 keV. The Cu is opaque, and the CH_2 essentially transparent, to these x-rays. The target is viewed along the length of the ripples by a gated x-ray framing camera. The radiographs, the images captured by the framing camera, show the shadows of the opaque Cu.

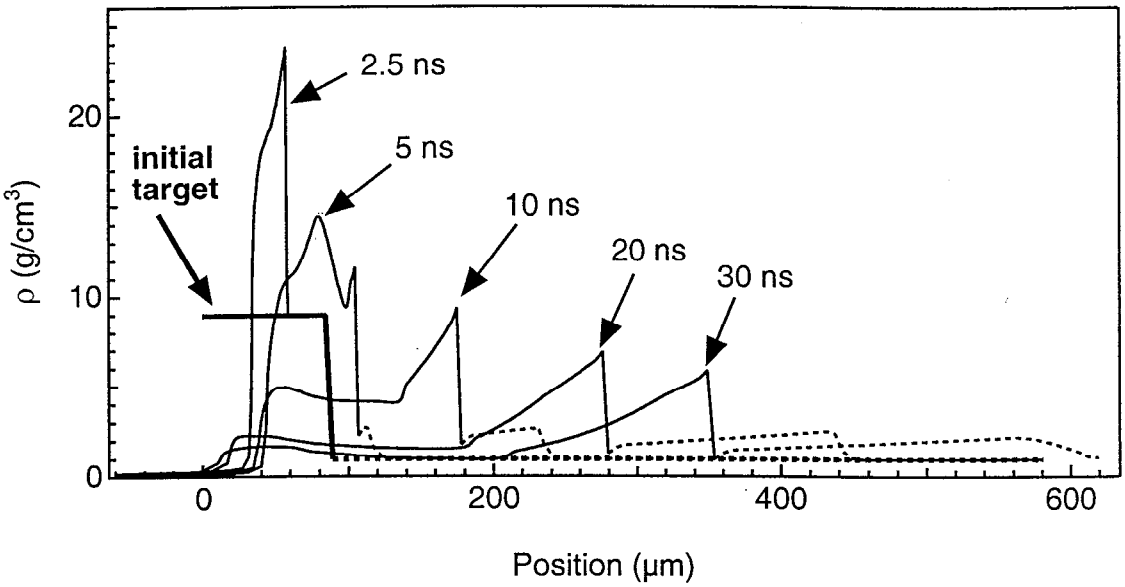

Figure 4.3: Density vs. position in initial Cu-CH_2 target, at mapping time (2.5 ns), and at 5, 10, 20 and 40 ns, from HYADES simulation. The heavy line is for $t = 2.5$ ns. At each time, the solid lines show the Cu density, and the dashed lines show the CH_2 density.

4.3 Simulations and data

4.3.1 1D simulations

We design the experiments using two codes, HYADES and CALE, which are discussed in Section 1.6, and also map into PROMETHEUS. HYADES has radiation transport; CALE and HYADES do not. We use the same EOS tables for the Cu and CH_2 in CALE as in HYADES, and use ideal gas EOS in PROMETHEUS, setting the ideal gas γ in each material to roughly reproduce the interface and shock velocities, and the compression in each material, as predicted by HYADES. The radiation temperature of the x-ray drive vs. time, $T_r(t)$, is known from separate drive characterization shots. We use the measured radiation temperature, $T_r(t)$, as the energy input to HYADES. We model the early stages of the experiment, during which the laser energy is input to the target and the shock is formed, in HYADES (which is 1D.) We then map the 1D result at an early time $t = t_{\rm map}$ into the 2D CALE simulation. We do the mapping by creating the desired CALE computational grid and then interpolating quantities from HYADES onto the CALE grid. We specify the CALE grid by specifying the 2D coordinates of each of the four corners

of each zone in CALE. In this discussion we will refer to the direction perpendicular to the 1D interface as the x direction, and the direction parallel to the 1D interface as the y direction. In CALE itself, what we call the x direction is designated the z direction, and what we call the y direction is designated the r direction. This is so because CALE can be run in either planar or r-z cylindrical geometry, and for simplicity a single pair of designations was used.) To make the mapping easy, in one direction we make all the grid lines parallel to the x direction (and thus parallel to each other), and perpendicular to the 1D interface (note that we are not required to do so, because the initial grid in CALE can be 'warped'). We then calculate the 2D centroid of each zone in the CALE grid. We map the density and material temperature from the HYADES simulation onto each row of zones parallel to the x direction, mapping to the centroid in that direction, since density and temperature are zone-centered quantities in CALE. Density and temperature are also zone-centered in HYADES. We map the velocity from the HYADES simulation, which is node-centered in HYADES, onto each row parallel to the x direction, mapping to the nodes in CALE, since velocity is also node-centered in CALE. We map temperature and density because these are the independent thermodynamic variables in the EOS tables which CALE uses.

The time $t_{\rm map}$ is the time when the shock is about to reach the thinnest part of the Cu layer, which is the 'valley' of the interface perturbation, located at $x = 85\,\mu{\rm m} - \eta_0 = 65\,\mu{\rm m}$ from the initial drive side of the Cu ($x = 0$). We set $t_{\rm map}$ to be the time when the shock is at $55\,\mu$m, which gives $t_{\rm map} = 2.5$ ns. By design, the laser drive turns off at 1 ns and the x-ray drive is rapidly diminishing by 2.5 ns. Hence, the hydrodynamics at the $x = 55\,\mu$m is decoupled from the radiation drive, as we discuss in a moment.

In the HYADES simulation, we use 152 zones in the Cu, feathered upwards in size from the drive side of the Cu, so that we resolve the hydrodynamics more accurately as the laser energy enters the problem on the drive side. We use 70 zones in the CH_2, feathered upward in size from the interface. The zones in the less dense CH_2 next to the interface are $\approx$ 3 times as wide as the adjacent zones in the more dense Cu, because a Lagrangian code like HYADES gives more accurate results if adjacent zones are closer in mass; this prescription for zoning is known as 'mass matching'.

Figure 4.3 shows density vs. 1D position x in the initial target (at time $t = 0$), at time $t_{\rm map} = 2.45$ ns, and at 5, 10, 20 and 30 ns, from a HYADES simulation. In Figure

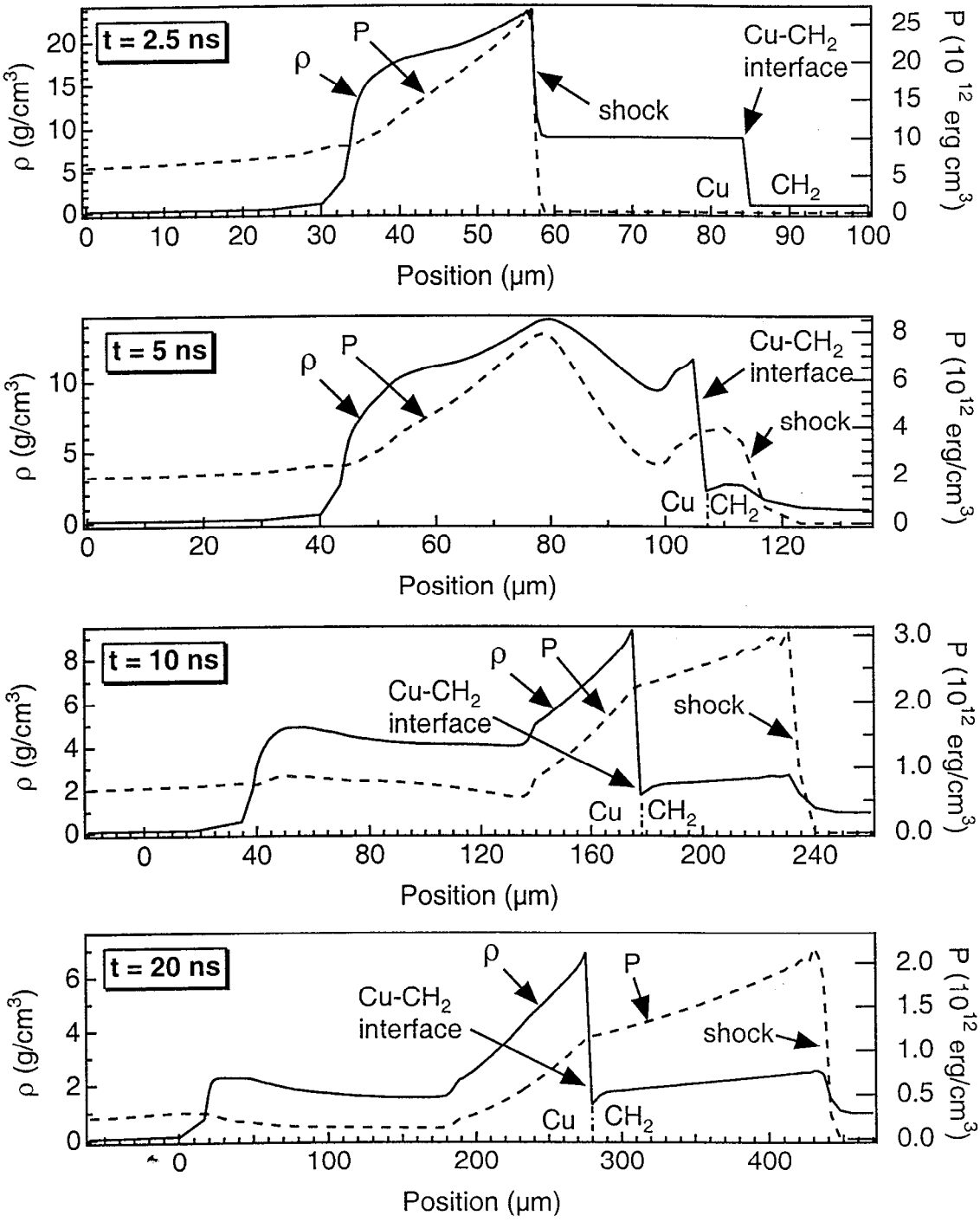

Figure 4.4: Pressure and density vs. position at $t = 2.5$, 5, 10, and 20 ns, from HYADES simulation.

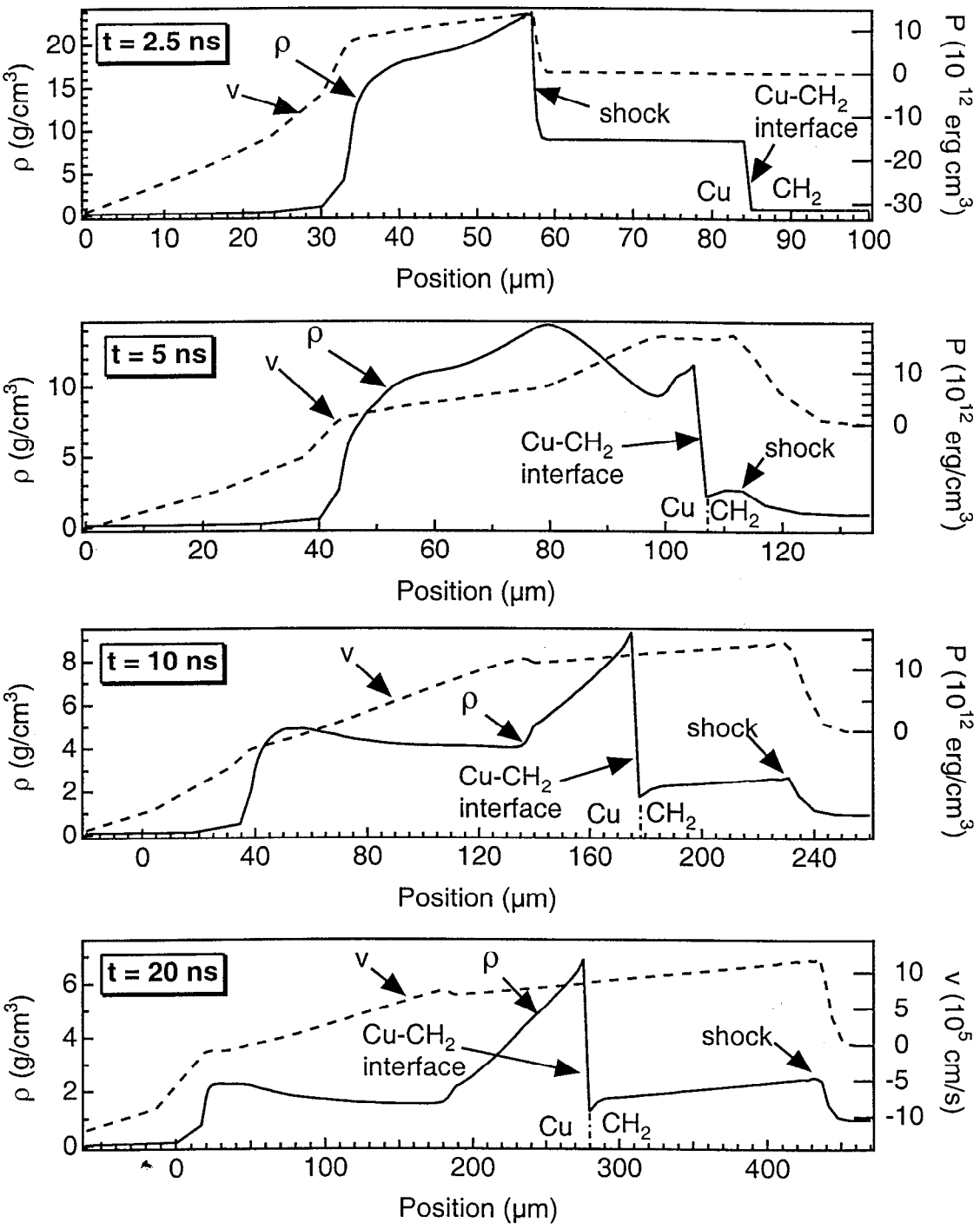

Figure 4.5: Velocity and density vs. position at $t = 2.5$, 5, 10, and 20 ns, from HYADES simulation.

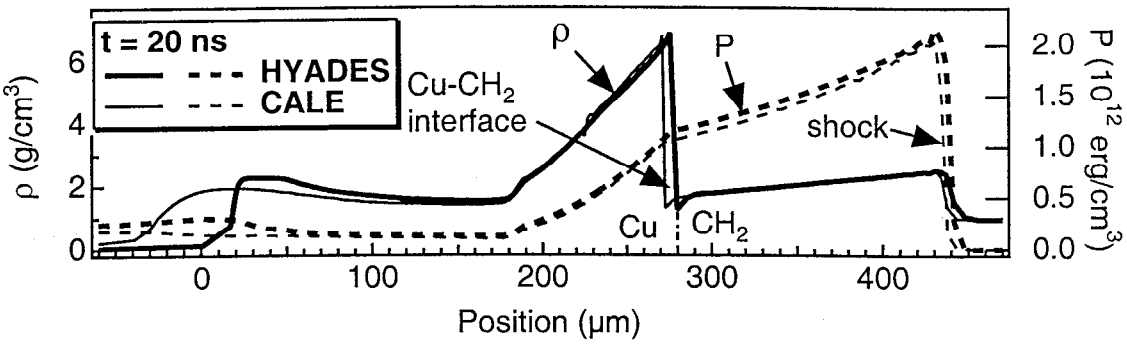

Figure 4.6: Pressure and density vs. position at $t = 20$ ns from HYADES and 1D CALE simulations.

4.4 we show the density and pressure profiles at the same times, and in Figure 4.5 we show the velocity and pressure profiles at those same times. At $t = 2.5$ ns in these figures, we can see the sharp rise in density and velocity at the ablation front, and the smooth rise of pressure and velocity from the ablation front to the shock, which shows that the target is decompressing. At $t = 5$ ns in these figures we can see the rarefaction moving backwards from the Cu-CH_2 interface into the Cu; the leading edge of the rarefaction is at about position $x = 78\,\mu$m. It is evident in density, velocity and pressure. The fluid velocity is higher beyond the rarefaction as the shock speeds up in the CH_2 after crossing the Cu-CH_2 interface. At $t = 5$ ns, the shock is spread out by the artificial viscosity in the code; the spreading is accentuated by the large zones in the CH_2 prescribed by mass matching. The density, pressure and velocity profiles at $t = 10$ ns and $t = 20$ ns are similar, suggesting that the 1D hydrodynamics approaches a state of self-similar expansion. At $t = 10$ ns and $t = 20$ ns the dense Cu spike forms a thin shell that expands over time, from a half-height thickness of about $35\,\mu$m at $t = 10$ ns to a half-height thickness of about $65\,\mu$m by $t = 20$ ns.

A weak reverse shock is visible at $t = 10$ ns at $x \approx 135\,\mu$m by a steeper rise in pressure and density and a steeper fall in velocity. This reverse shock is reminscent of the reverse shock that forms in the He layer in the 1D SN 1987A simulation shown in Fig. 2.3 at $t = 2000$ s. A reverse shock is more likely to form in spherically expanding ejecta as in the SN than in the decompressing planar target in the laser experiment, because in spherical geometry the expanding ejecta below the interface converts internal energy to kinetic energy more quickly.

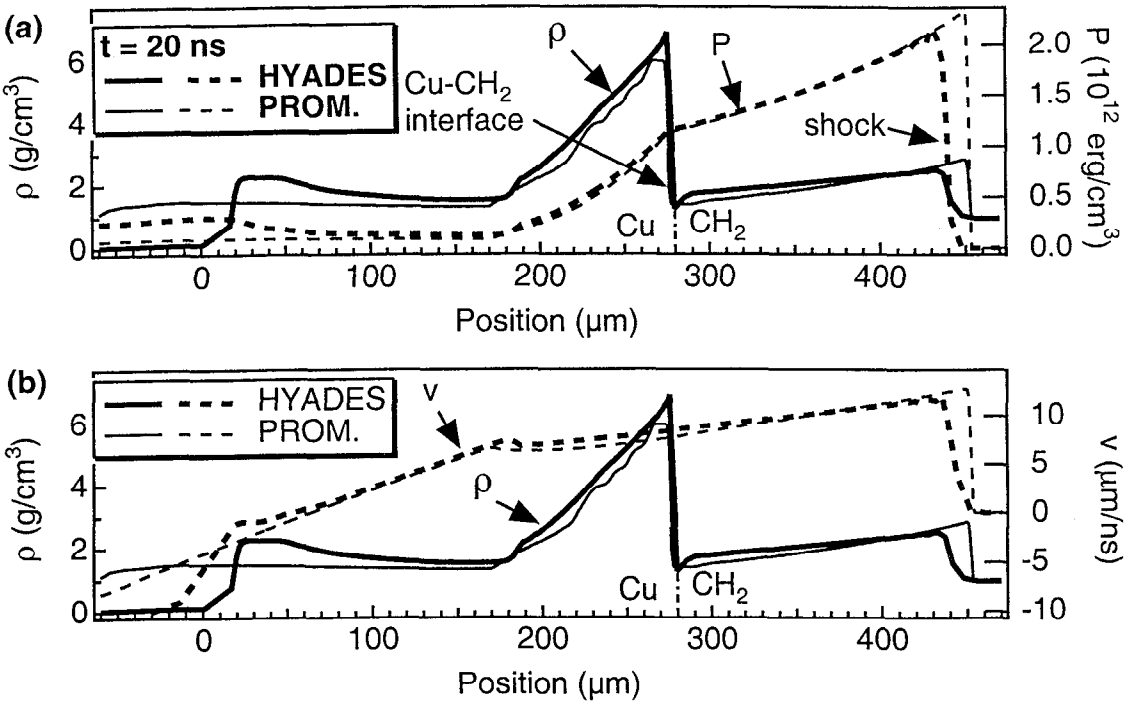

Figure 4.7: (a) Pressure and density vs. position at $t = 20$ ns from HYADES and 1D PROMETHEUS simulations. (b) Velocity and density vs. position.

At $t = 30$ ns in Figure 4.3, the shock has reached the end of the CH_2 at $x = 685\,\mu$m and a rarefaction has begun to come back into the target. The leading edge of the rarefaction is visible in Figure 4.3 at about $x = 580\,\mu$m. We stop collecting data from the experiment by $t = 40$ ns, before the rarefaction reaches the Cu-CH_2 interface. If we wished to run the experiment longer, we would simply need to make the CH_2 thicker.

In Figure 4.6 we compare density and pressure in HYADES and in 1D CALE at $t =$ 20 ns, long after the mapping from HYADES to CALE. In the HYADES run shown in Figure 4.6 we have continued running HYADES after the mapping time, with radiation transport and conduction still turned on. In the region of the problem that interests us, near the interface, CALE and HYADES are in very good agreement at this late time. The profiles at the former ablation front, at $x \approx 0\,\mu$m in Figure 4.6 look different, because in HYADES the tail of the radiation drive after the mapping time continued to heat the rarefied Cu below the ablation front and keep its pressure high, while in CALE the blowoff simply began cooling. This excellent agreement except for at the ablation front suggests that diffusion of energy by radiation transport and heat conduction is unimportant after

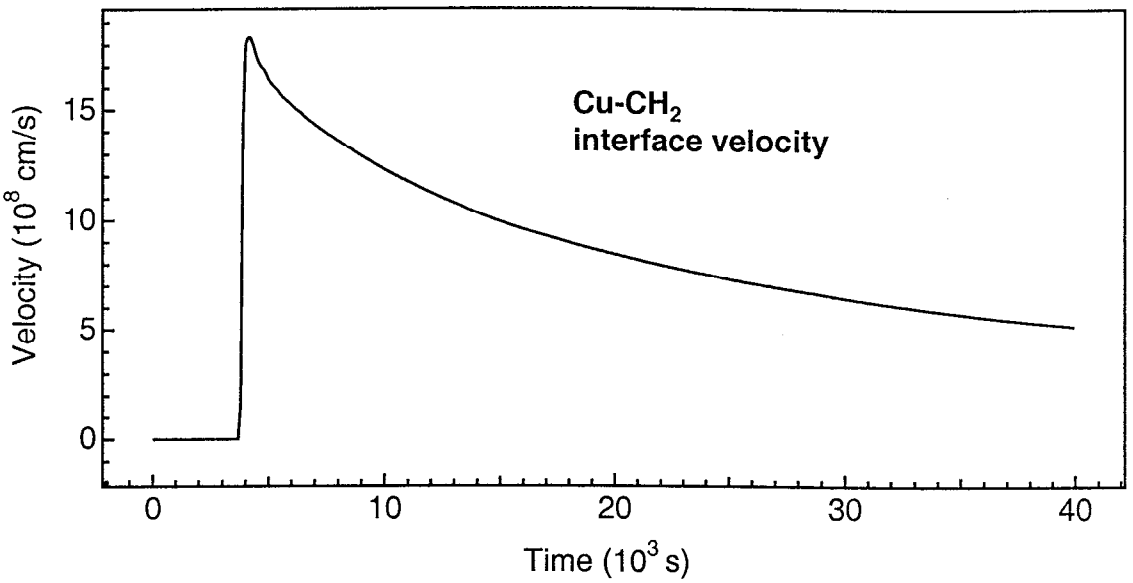

Figure 4.8: Velocity of Cu-CH_2 interface vs. time from 1D HYADES simulation.

the laser energy has entered the problem, and that the pure hydrodynamics which CALE is calculating is entirely adequate to describe the problem after the mapping time. The behavior in the former ablation front, well removed from the interface, is only properly described by including radiation transport and heat conduction, but as we see Figure 4.6, significant information from this region is not transmitted to the interface region during the time of interest in the problem.

In Figure 4.7 we compare a 1D PROMETHEUS simulation of the experiment (using ideal gas EOS) at 20 ns to the results from HYADES. Figure 4.7a compares densities and pressures, and Figure 4.7b compares velocities. The densities and pressures are in reasonable agreement; the shock pressure is slightly higher. The density profile is less smooth in PROMETHEUS, because the Lagrangian code HYADES, which stabilizes shocks with artificial viscosity, represents a shock differently than the PPM code PROMETHEUS, so mapping the HYADES shock onto the PROMETHEUS grid initially causes small disturbances in the flow behind the shock in PROMETHEUS. The interface velocity is well reproduced, and the shock velocity is slightly higher with PROMETHEUS. Back at the former ablation front, the material has decompressed more in PROMETHEUS; as with CALE, the lack of radiation transport in PROMETHEUS causes disagreement with HYADES far from the region of interest near the interface.

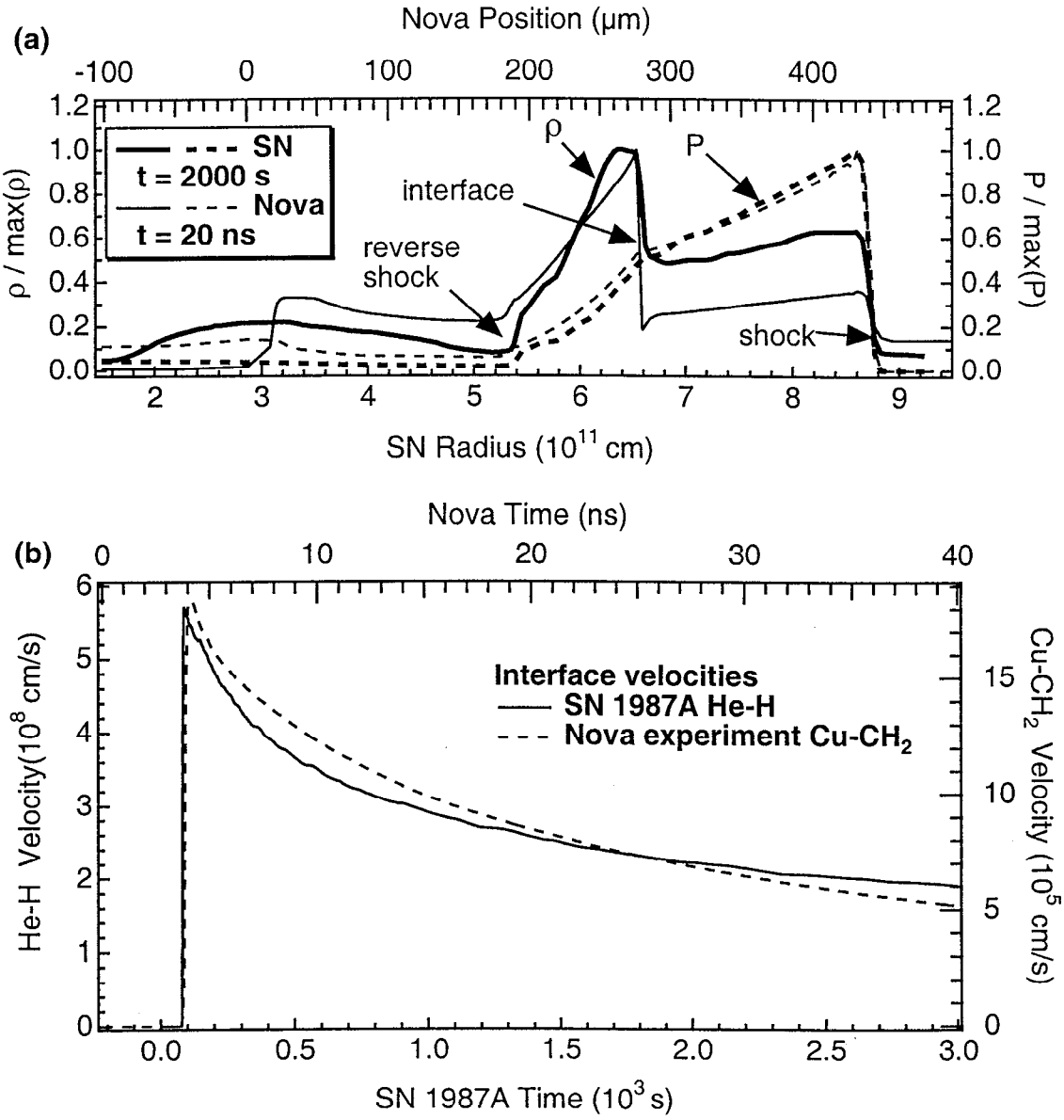

Figure 4.9: Scaling of hydrodynamics between SN and Nova laser experiment. (a) Normalized density and pressure vs. position from 1D PROMETHEUS simulation of SN 1987A and 1D HYADES simulation of Nova Cu-CH_2 experiment. (b) SN 1987A He-H velocity vs. time from 1D PROMETHEUS, and Nova Cu-CH_2 velocity vs. time from HYADES.

Figure 4.8 shows the velocity of the Cu-CH_2 interface vs. time, from the 1D HYADES simulation. There is a sharp acceleration due to the shock at $\approx$ 3.8 ns, and then a protracted deceleration as the lighter CH_2 layer slows down the heavier Cu layer.

The sharp acceleration of the Cu-CH_2 interface by the shock suggests that the interface will be subject to the RM instability. The crossed gradients at the O-He interface by $t =$ 10 ns (Figure 4.4), and the deceleration of the Cu-CH_2 interface until the end of the simulation (Figure 4.8) suggest that the Cu-CH_2 interface will be subject to the RT instability as the lighter CH_2 layer slows down the denser Cu layer.

There are some obvious similarities between the hydrodynamics shown in Figures 2.2, 2.3, 2.4 and 2.5 from the 1D PROMETHEUS simulation of SN 1987A and the hydrodynamics shown in Figures 4.3, 4.4, 4.5 and 4.8 for the Nova experiment. Both the He-H interface in SN 1987A and the Cu-CH_2 interface in the Nova experiment are subjected to rapid acceleration and then to deceleration, and thus to the RM and RT instabilities. Figure 4.9 compares the 1D hydrodynamics for the SN and Nova experiment directly. Figure 4.9a compares the normalized pressures and densities at characteristic times which correspond to each other from the scaling argument in Section 3.2.3. Figure 4.9b compares the normalized velocity vs. time trajectories for the He-H and Cu-CH_2 interfaces. The similarity of the overlaid curves in Figures 4.9 is a pictorial representation of the scaling argument in Section 3.2. The Euler equations are invariant under the transformations described in Section 3.2.2. The transformations account for the difference in units.

4.3.2 2D simulations and data

Figure 4.10 shows the evolution of the Cu-CH_2 interface in time, from a 2D CALE simulation. CALE is run in ALE mode, with tabular EOS. As with the 1D CALE simulation shown in Figure 4.6, we begin the CALE simulation by mapping from HYADES at the mapping time, $t = 2.5$ ns. In this simulation, we set the grid points in the y direction in the CALE grid such that the initial interface is a piecewise smooth 2D perturbation (see the discussion in Section 4.5) running along a line of nodes that separates zones with only Cu on one side from zones with only CH_2 on the other. In doing the interpolation from HYADES, we account for the variation in interface x coordinate by adjusting density and the CALE quantity that records the material in each zone, accordingly.

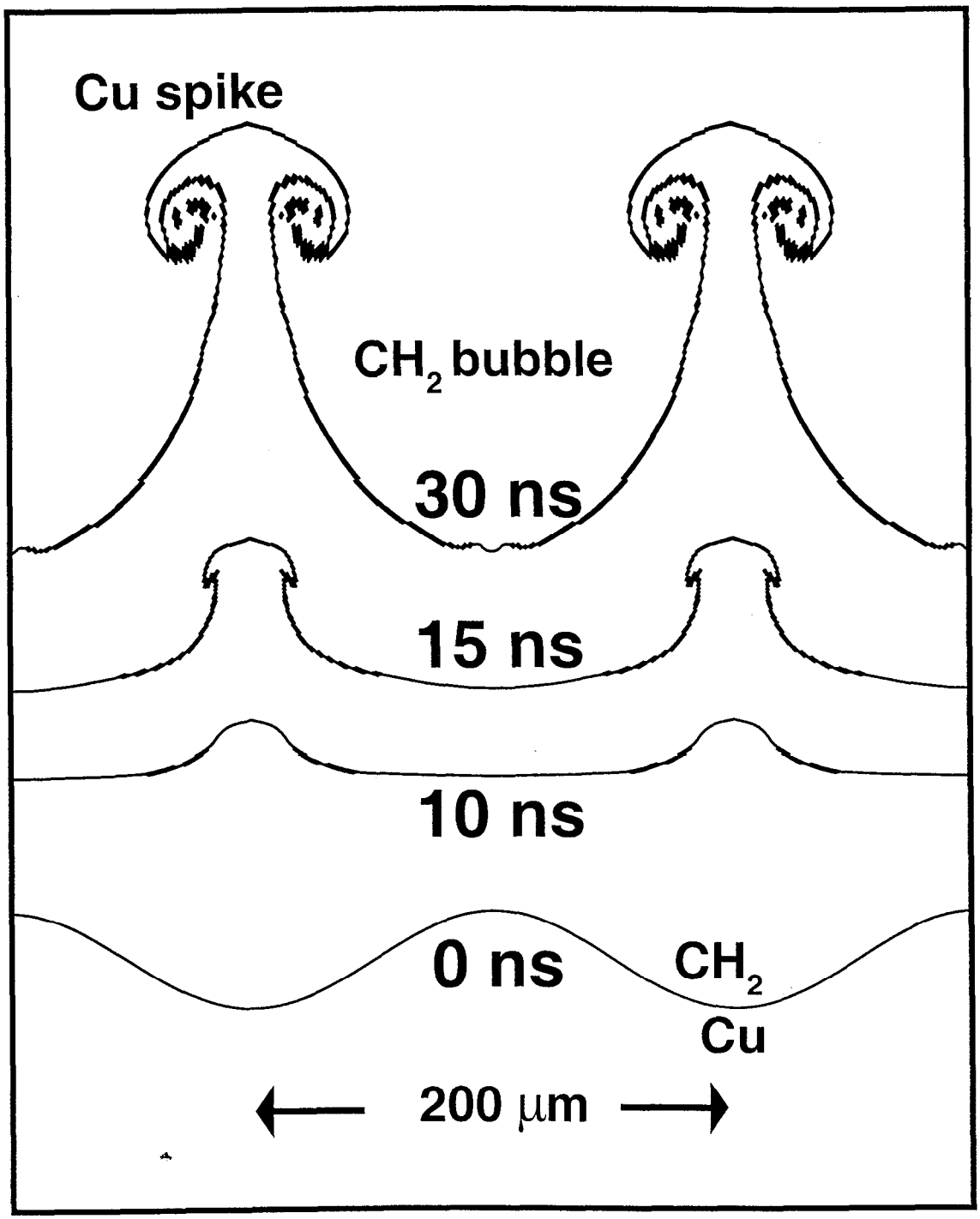

Figure 4.10: Evolution of 2D interface in Nova Cu-CH_2 experiment from a CALE simulation.

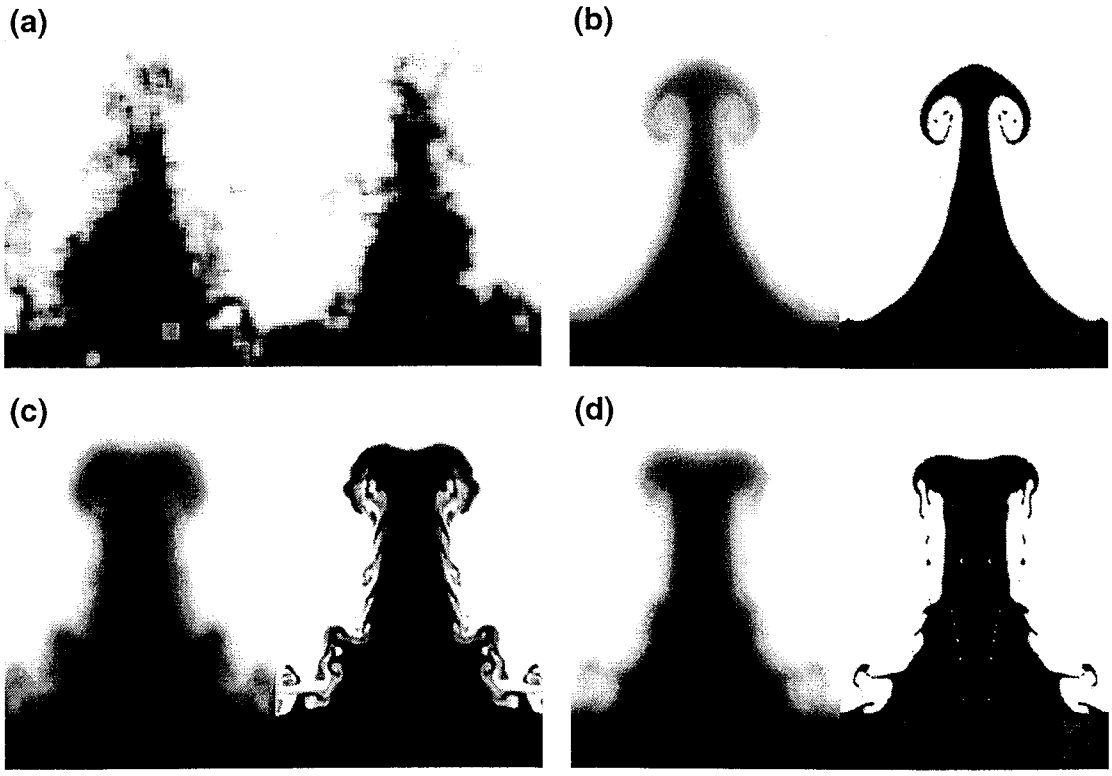

Figure 4.11: Nova experiment at $t = 30.2$ ns. (a) Radiograph from experiment. (b) CALE simulation using ALE mode, tabular EOS and smooth initial interface. (c) PROMETHEUS simulation using fixed (Eulerian) orthogonal grid, ideal gas EOS and stairstepped initial interface. (d) CALE simulation using fixed orthogonal grid, ideal gas EOS and stairstepped initial interface (same as PROMETHEUS.) Evolution of 2D interface in Nova Cu-CH_2 experiment from a CALE simulation.

In Figure 4.10 at $t = 0$ ns we are looking along the 2D ridges of Cu and troughs of CH_2 in the initial interface perturbation, the same as in Figure 4.2. At $t = 10$ ns we can see the inversion of the initial interface shape due to the RM instability. At this time the perturbation is growing both by the RM instability and by the RT instability as the CH_2 slows down the Cu. At $t = 15$ ns, rollups due to the KH instability (see the discussion in Section 1.3.4.4) are evident at the Cu spike tip. At $t = 30$ ns. the growth is becoming deeply nonlinear and the KH instability has produced pronounced vortices at the Cu spike tip. The average Cu-CH_2 interface moves several hundred μm in 30 ns, as expected from the interface velocity from the 1D HYADES simulation (Figure 4.8).

Figure 4.11 compares radiographs from the experiment at $t = 30$ ns to the results

of simulations. Figure 4.11 is a radiograph from the experiment at $t = 30$ ns. The dark shadows are the Cu spikes. The distance between the spike tips is $200\,\mu$m, the same as the wavelength of the original perturbation. Some of the indistinct grey regions are background noise. Some of the finer filaments independent of the spikes may be material curling up from the edges. Figure 4.11b is the result of a CALE simulation using ALE mode, tabular EOS and a smooth initial interface. The right side is the mass fraction of Cu from the simulation. The left side is a simulated radiograph made from the simulation. To calculate the simulated radiograph, we simulate shining the backlighter through the result of the simulation and recording the image with the gated camera. This involves calculating the attenuation of the backlighter through the Cu, and then applying the known point spread function of the camera pinholes to the attenuated output. The spread caused by the pinhole 'smears' the image, limiting the resolution to no better than 10 μm. As a result of this limit on the resolution, and the background noise, as well as the relative paucity of material in the rollups at the tip, we are not able to resolve the rollups in the data.

Figure 4.11c is the result of a PROMETHEUS simulation using a fixed (Eulerian) orthogonal grid, ideal gas EOS and a stairstepped initial interface (the latter unavoidable in PROMETHEUS.) As we will discuss in a moment, both CALE and PROMETHEUS reproduce the gross hydro correctly, that is, the positions vs. time of the bubble and spike tips. We show this in Figure 4.12 by a plot of bubble and spike position vs. time from the experimental data and from the 2D CALE and PROMETHEUS simulations shown in Figure 4.11b and 4.11c. Also shown is the position of a 1D (unperturbed) interface as calculated by CALE and by PROMETHEUS. It is with respect to this unperturbed interface that we calculate the bubble and spike velocities for the purpose of theoretical analysis. We present a theoretical analysis of the bubble and spike tip velocities in Section 4.4.5.

There are obvious differences in fine structure between the CALE and PROMETHEUS simulations in Figures 4.11b and 4.11c. We will discuss the differences in Section 4.5, and suggest that they are mainly due to stairstepping the initial interface as opposed to representing it as a smooth sinusoid. To show that the difference between the codes is not a fundamental issue in the way the two codes calculate hydrodynamics, we have also tried running CALE in much the same way we ran PROMETHEUS, using a fixed orthogonal

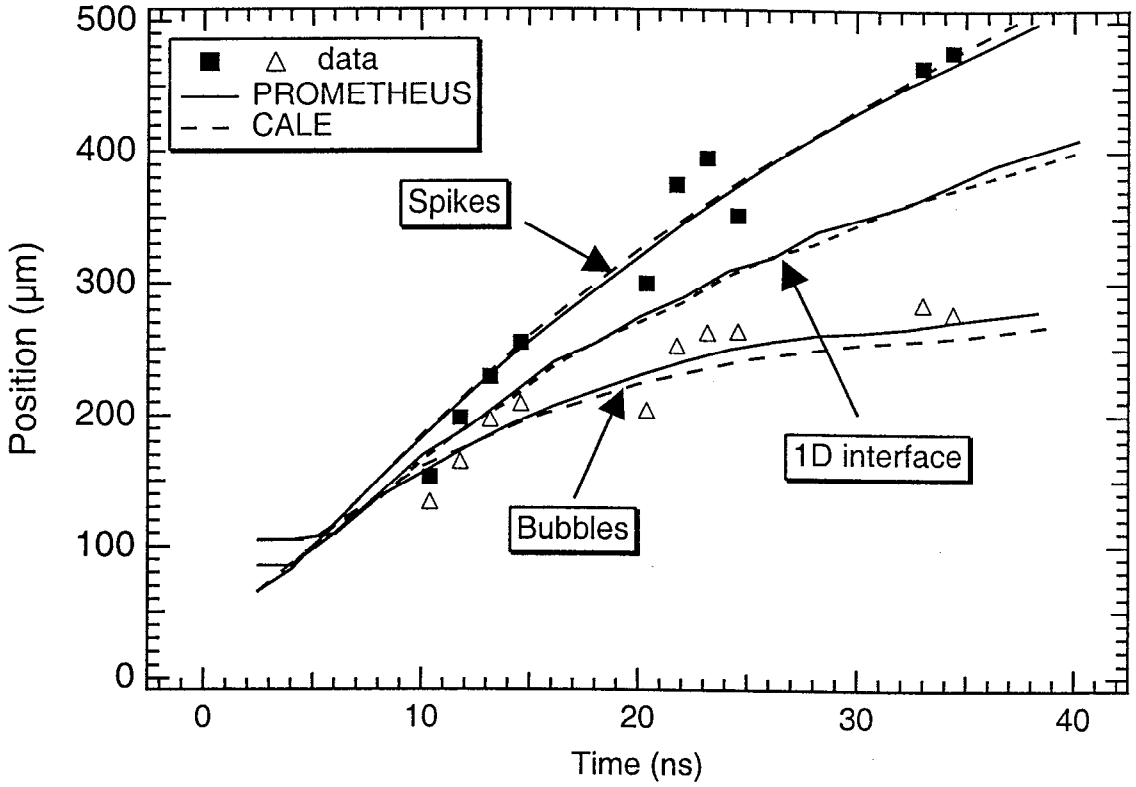

Figure 4.12: Positions of bubble and spike vs. time from the experimental data and from the 2D CALE and PROMETHEUS simulations. Also shown is the position of a 1D (unperturbed) interface as calculated by CALE and by PROMETHEUS. The uncertainty in the bubble and spike positions in the date is $\pm$ 35μm.

grid, ideal gas EOS and stairstepped initial interface. The result is shown in Figure 4.11d. The general shape of the interface is now very similar (compare Figures 4.11c and 4.11d). There is still more fine structure in PROMETHEUS, perhaps owing to the intrinsically higher accuracy of the PPM method. There is also material diffusion in PROMETHEUS, evidenced by the greyish fringes on the interface, in which the mass fraction is a mixture of Cu and CH_2. These simulations are high resolution, in the sense that the gross hydrodynamics (bubble and spike positions) are well converged at this resolution. The bubble and spike positions in a simulation at one quarter the resolution differ only by one or two zone widths from the positions in these higher resolution simulations.

In the fixed grid simulations (Figures 4.11c and 4.11d), we used 200 zones per wavelength of the perturbation, that is, 1 μm per zone, in both the x and y directions. In the CALE simulation, we used similar zoning, 200 zones per wavelength in the y direction

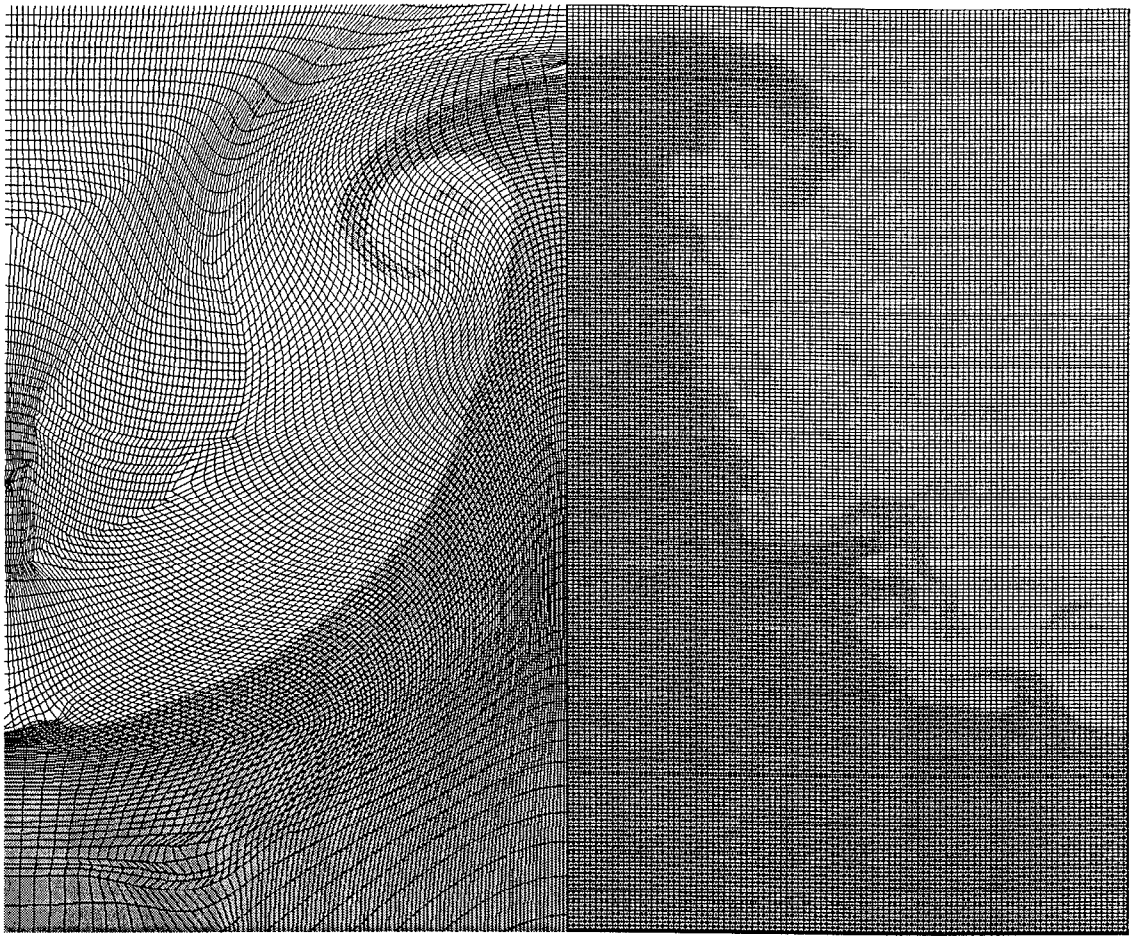

Figure 4.13: Grid in simulations of 2D Nova experiment at $t = 30$ ns. Left: fixed Eulerian grid (PROMETHEUS). Right: ALE grid (CALE).

(parallel to the 1D interface), but feathered the zoning upward in size in the x direction away from the Cu-CH_2 interface. Figure 4.13 shows the difference in the CALE and PROMETHEUS grids at $t = 30$ ns. Because of the natural compression of zones in CALE, the resolution becomes similar in the regions of interest near the Cu-CH_2 interface.

4.4 Analytic theory of instability growth

4.4.1 Overview

In this section we present a preliminary theoretical analysis of the bubble and spike velocities shown in Figure 4.12. We compare predictions for bubble and spike velocities from potential flow theory (see Refs. [5, 6, 81]) and our modification of the Ott thin shell

theory (see Refs. [120, 17]) to the results of a CALE simulation of the Nova experiment. Since the CALE (and PROMETHEUS) simulations agree well with the data (see Figure 4.12 and the accompanying discussion in Section 4.3.2), this is equivalent to comparing the theory to the experimental data.

We use Meyer-Blewet (MB) theory (see the discussion in Section 1.3.4.2 and see Refs. [111, 57]) for the linear stage of bubble and spike growth, to provide initial conditions for the potential flow and thin shell theories. The reason we consider thin shell theory is seen in Fig. 4.6; in terms of density, the half-height thickness of the dense Cu is is small at 20 ns — about 50 μm — compared to the perturbation wavelength $\lambda = 200$ μm. By comparison, the shocked CH_2 layer is comparable in thickness to λ. The potential flow assumes two adjacent fluids of semi-infinite extent perpendicular to the interface between the fluids. A low density bubble should rise faster if it has to push aside only a thin shell of dense material than if if had to push aside a deeper extent of material (see [113] and references therein for a study of RT instability in finite thickness fluids.)

Potential flow theory also assumes that the fluids do not decompress over time. In the Nova experiment, the fluids do decompress over time, because of the pressure gradient from the shock backwards through the Cu-CH_2 interface and into the Cu — see the profile of pressure in Figure 4.6 (the pressure gradient is also responsible for the deceleration of the interface and thus the RT component of the instability growth.) Thus, before applying the potential flow theory to the results of the simulations, we first 'undecompress' the bubble and spike velocities, as discussed in Section 4.4.5.

4.4.2 Meyer-Blewett theory

The Meyer-Blewett (MB) theory [111, 57] predicts the amplitude η_0^* and rate of change of amplitude $\dot{\eta}^*$ of a material perturbation at the interface between two fluids after a shock has passed the interface. Intuitively, the shock will reach the 'valley' of the perturbation first, and compress the valley before the shock reaches the peak of the perturbation. Thus, the amplitude of the perturbation should be decreased by the shock. The prediction of MB is

$$\eta_0^* = \eta_0(1 - u_i/v_s) \tag{4.1}$$

$$\dot{\eta}^* = \frac{\eta_0 + \eta_0^*}{2} k A^* u_i, \tag{4.2}$$

where η_0 is the preshock amplitude of the perturbation, $k = 2\pi/\lambda$ is the wavenumber of the perturbation, A^* is the postshock Atwood number $(\rho_2^* - \rho_1^*)/(\rho_2^* + \rho_1^*)$, and u_i and v_s are the fluid velocity behind the shock, and the shock velocity, respectively. The original RM theory [130] made a prediction for $\dot{\eta}^*$ which was found experimentally to be incorrect. MB theory is an ad hoc modification to the original RM theory in which the term $(\eta_0 + \eta_0^*)/2$ is used instead of the more intuitively obvious η_0.

4.4.3 Potential flow theory

Potential flow theory predicts the rate of change of the single mode bubble and spike velocities in the nonlinear stages of instability growth (See the discussion in Section 1.3.4.3 and see Refs. [5, 6, 81]). The prediction of the theory for the velocity u of a bubble or spike is (see Refs. [6, 81])

$$\dot{u}(t) = c_b g(t) - c_D u(t)^2/\lambda, \tag{4.3}$$

where the buoyancy coefficient is $c_b = A^*/(1+A^*)$ and the drag coefficent is $c_{D,\text{bubble}} = 3\pi$ for the bubble and $c_{D,\text{spike}} = 3\pi(1 - A^*)/(1 + A^*)$ for the spike. In applying this theory we will take initial conditions from MB and numerically integrate this equation forward in time to predict bubble and spike velocities vs. time.

4.4.4 Thin shell theory

In his original thin shell theory [120, 17] Ott solved the equations of motion for an infinitely thin shell with massless fluids at constant pressure above and below, and a gravitational force acting perpendicular to the initial average interface. The equations of motion are

$$\ddot{x}(\xi, t) = -g(t)z'(\xi, t) \tag{4.4}$$

$$\ddot{z}(\xi, t) = -g(t)x'(\xi, t), \tag{4.5}$$

where where ξ is the Lagrangian coordinate of a point on the thin shell, and x and z are the Eulerian coordinates parallel and perpendicular, respectively, to the unperturbed interface, $g(t)$ is the gravitational field, the dot refers to derivatives with respect to time, and the prime to derivatives with respect to the Lagrangian coordinate.

In [120], Ott presented the solution for the case of a constant gravitational field $g(t) = g_0$. In Ref. [17], Basko presented the solution for the case $g(t) \propto 1/t^2$. In the

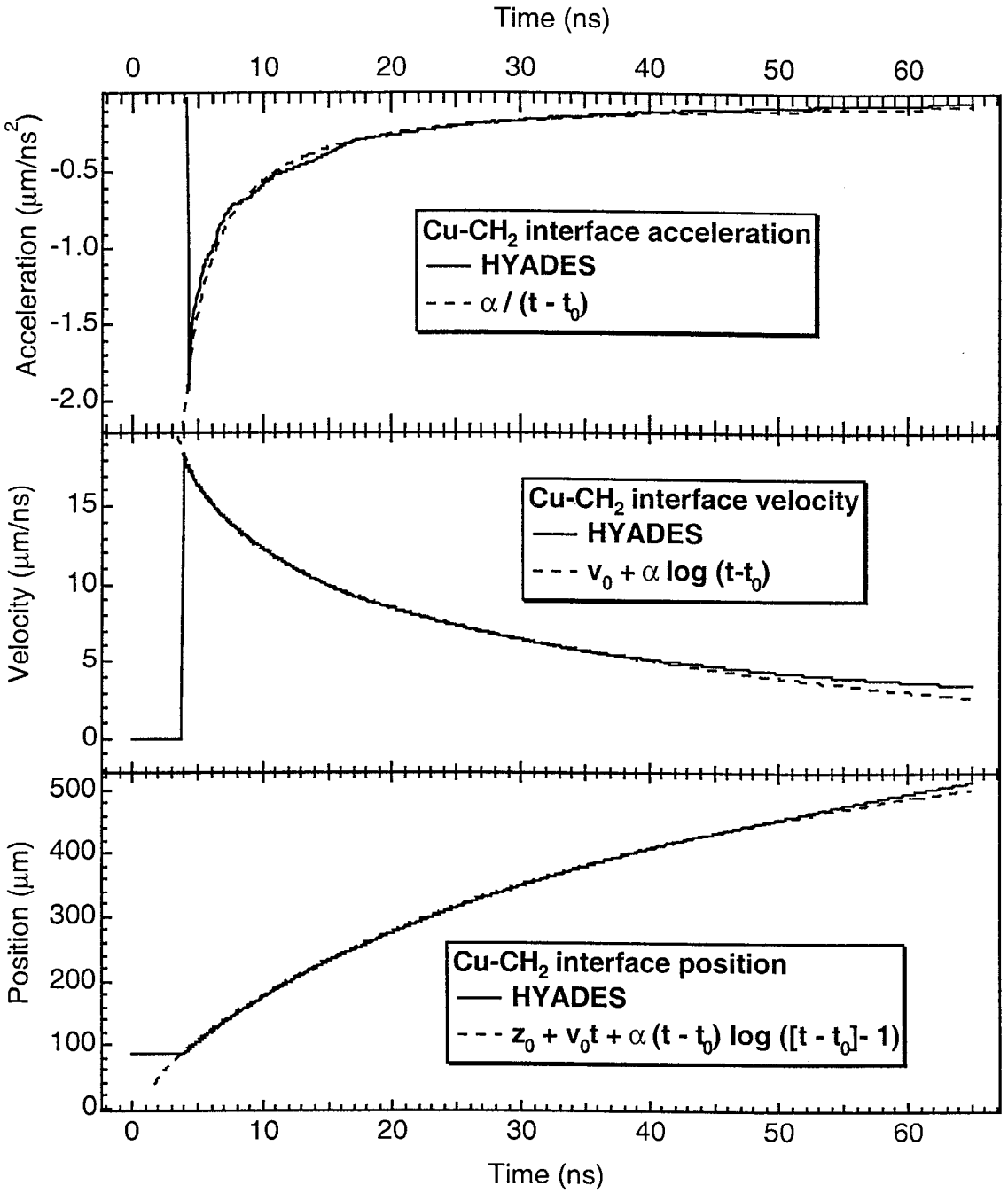

Figure 4.14: Fitting $g = \alpha/(t - t_0)$ to the actual interface deceleration in the Nova experiment. We fit $g = \alpha/(t - t_0)$ to the simulated interface deceleration at $t = t_0 = 1.8$ ns and $t = 24$ ns. The resulting α is -4.67 μm/ns. (a) Comparison of $g = \alpha/(t - t_0)$ for $\alpha = 3.1$ μm/ns to the interface acceleration from HYADES. (b) Comparison of integrating $g = \alpha/(t - t_0)$ over time to the interface velocity from HYADES. (c) Comparison of integrating $g = \alpha/t$ over time twice to the interface position from HYADES.

HYADES calculation of the laser experiment, (see Section 4.3.1) the effective deceleration $g(t)$ of the interface after the sharp acceleration due to shock is fit extremely well by the simple form $g(t) = \alpha/(t-t_0)$. We fit $g = \alpha/(t-t_0)$ to the simulated interface deceleration at $t = t_0 = 1.8$ ns and $t = 24$ ns, resulting in $\alpha \approx -4.67$ μm/ns; using this t_0 and α, we integrate $g(t)$ over time to reproduce the 1D interface velocity and position. We illustrate this in Figure 4.14. In Figure 4.14a we compare $g = \alpha/(t - t_0)$ for $\alpha = 4.67$ μm/ns to the acceleration of the interface zone in the HYADES simulation, calculated by taking the time derivative of the interface velocity as calculated in HYADES. In Figure 4.14b we compare the result of integrating $g = \alpha/(t - t_0)$ over time to the actual interface velocity profile shown earlier in Figure 4.8. In Figure 4.14c we compare the result of integrating $g = \alpha/(t-t_0)$ twice over time to the actual interface position profile from HYADES. The fits in acceleration, velocity, and position are extremely good until $t = 40$ ns.

Here we present the solution to equations 4.4 for the case $g(t) = \alpha/t$, namely,

$$x(\xi, t) = \xi + f(t)\cos(k\xi) \tag{4.6}$$

$$z(\xi, t) = z_0 + f(t)\sin(k\xi) \tag{4.7}$$

$$\ddot{z}_0(t) = g(t) \tag{4.8}$$

$$f(t) = \sqrt{\frac{t}{A^* k\alpha}}\{a_1 I_1\sqrt{A^* k\alpha t} - b_1 K_1\sqrt{A^* k\alpha t}\}, \tag{4.9}$$

where $k = 2\pi/\lambda$ is the wavenumber of the perturbation, and I_1 and K_1 are the growing and damped modified Bessel functions, respectively. The two constants a_1 and b_1 are set by the amplitude and velocity of the initial perturbation. In the exact solution of this case, with massless fluids above and below, the quantity A^* (the postshock Atwood number) in Eq. 4.6 equals unity. To crudely account for the arbitrary postshock Atwood number, we insert A^* back into the $A = 1$ solution, replacing all factors of $k\alpha$ with $A^* k\alpha$. Thus A^* in this ad hoc modification to the exact solution plays the same role that it does in the original RT linear stage growth rate solution [104, 145], $\dot{\eta} = \eta_0 \exp(-\gamma t)$, where the growth rate γ is given by $\gamma = \sqrt{(Akg)}$, A being the Atwood number and g the constant gravitational force (See the discussion in Section 1.3.4.1). The effect of A^* in both cases is to slow the growth rate. For the Cu-CH_2 experiment, our simulations predicted a post-shock Atwood number of 0.65.

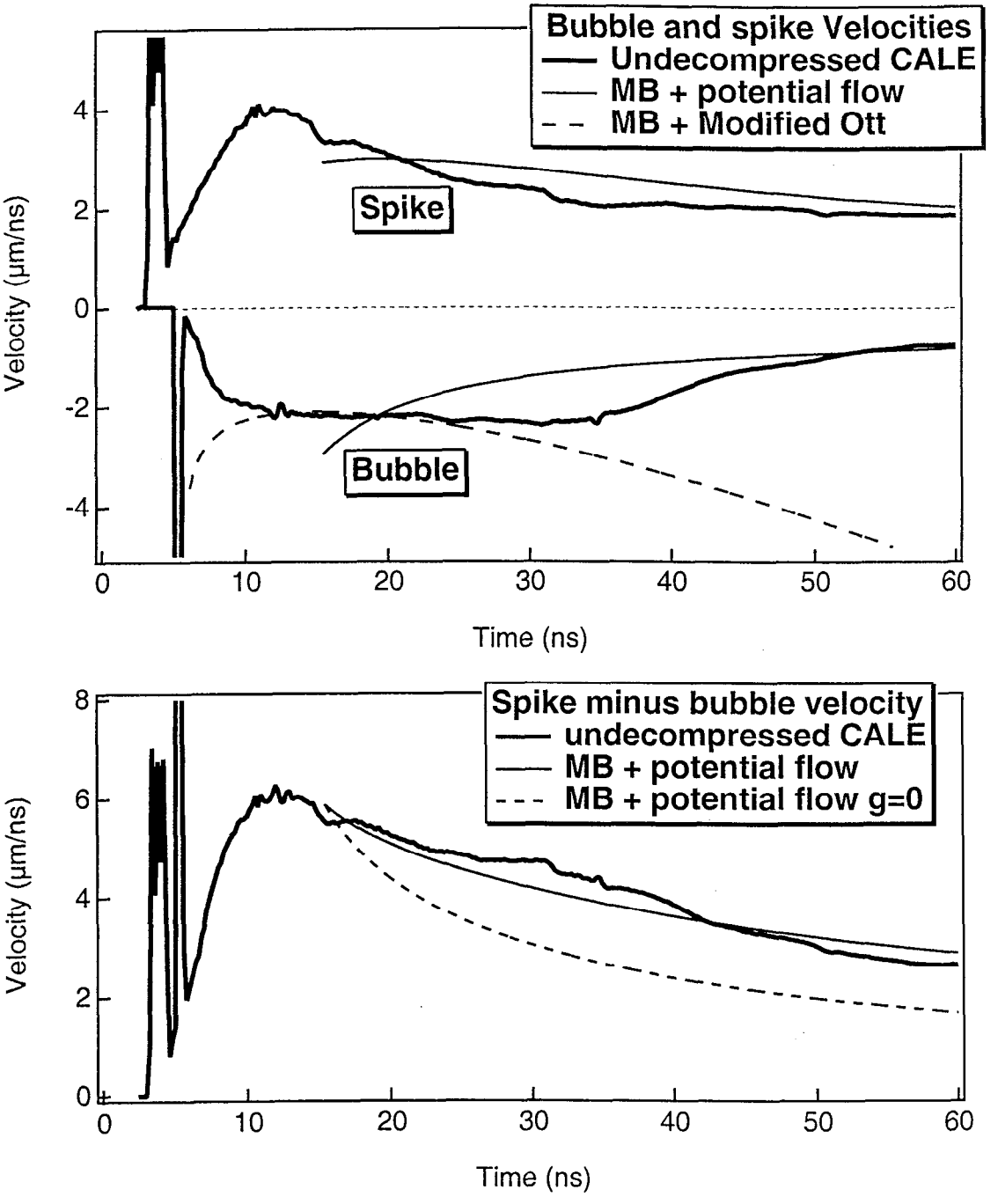

Figure 4.15: Comparison of simulations to analytic theory for the Nova Cu-CH_2 experiment. (a) Meyer-Blewett (MB) theory mapped to potential flow theory and to modified Ott thin shell theory. (b) Spike velocity minus bubble velocity for simulation and for MB mapped to potential flow theory (solid line), and the result of integrating Eq. 4.3 with the $g(t)$ set to zero (dashed line).

4.4.5 Comparison of theory to simulations

As discussed in Section 4.4.1, before applying potential flow theory we must 'undecompress' the bubble and spike velocities. One way to do this would be to gauge the decompression by the change in average density in each fluid, that is doing the transformation $u(t) \rightarrow u(t) * \bar{\rho}(t)/\bar{\rho}_0$, where u is a bubble or spike velocity, $\bar{\rho}(t)$ is the average density at time t in the appropriate fluid (the dense fluid for the spike and the light fluid for the bubble.) However, there are some difficulties with applying this procedure for the experiment. First of all, it is not entirely clear how to calculate the average density; should the massively decompressed Cu blowoff be included? The answer is probably not, since the huge volume in the blowoff would lower the averge density considerably and yet the blown off material does not affect the hydrodynamics at the interface (see Figure 4.6 and the accompanying discussion in Section 4.3.1). Also, as the shock advances into the CH_2, CH_2 enters the problem. The unshocked CH_2 should not be considered part of the problem, as it can not play a part in the hydrodynamics in the rest of the target. Yet, should shocked CH_2 that enters the problem at a later time be included in trying to determine the decompression of material that was shocked earlier? A possible solution is to track the fluid element at a bubble or spike tip at all times and normalize to its initial density. Care must be taken, though, that the initial density taken is the post-shock density.

A simpler procedure is to assume a 1D 'accordion-like' expansion velocity $v(x,t) = V(x,t) - U_{\rm i}(t)$ about the Cu-CH_2 interface for each point (x,y) in the entire target, where $U_{\rm i}(t)$ is the rest frame velocity of the interface, and $V(x,t)$ is the 1D fluid velocity in the rest frame. The velocity $V(x,t)$ can be obtained at each coordinate x in the fluid at each time t from a 1D simulation of the experiment. Given a bubble or spike velocity $U(x,y,t)$ in the rest frame, we can then subtract $V(x,t)$ from $U(x,y,t)$ to get the undecompressed bubble or spike velocity $u(x,y,t)$. That is, the decompressed ('raw') bubble or spike velocity with respect to the interface is $U(x,y,t) - U_{\rm i}(t)$, and the undecompressed bubble or spike velocity is $(U(x,y,t) - U_{\rm i}(t)) - (V(x,t) - U_{\rm i}(t))$, ie. $u(x,y,t) = U(x,y,t) - V(x,t)$. With this procedure we avoid having to decide which parts of the fluid to consider in estimating the decompression. A more elaborate version of either scheme is probably not warranted, given the crudity of the approximations in each scheme.

In Figure 4.15 we compare the undecompressed bubble and spike velocities from the 2D CALE simulation shown in Figures 4.10 and 4.11b to the predictions of MB theory mapped to potential flow theory and MB theory mapped to the modified Ott thin shell theory. In Figure 4.15a, the heavy solid lines are undecompressed bubble and spike velocities (in the rest frame of the 1D unperturbed interface.) The light solid line is the prediction of MB mapped to potential flow theory and the dashed line is the prediction of MB mapped to the modified Ott thin shell theory. MB mapped to potential flow theory predicts the spike velocity reasonably well. The modified thin shell theory predicts the bubble velocity well at early times, while at later times the potential flow theory predicts the bubble velocity better.

The bubble and spike velocities are considerably slower than the sound speed in the fluids — 2–3 μm/ns (see Figure 4.15a) vs. $\approx$ 10 μm/ns. That is why we can apply incompressible theory at all. Thus, the hydro at the bubble and spike tips should be well coupled, suggesting that we consider the velocity at which the bubble and spike tip are separating from each other. In Figure 4.15b, we show the prediction of MB mapped to potential flow theory for the spike velocity minus bubble velocity; the heavy sold line is the undecompressed spike velocity minus bubble velocity, and we also show the results of integrating Equation 4.3 both with $g(t) \propto \alpha/t$ (light solid line) and with $g(t)$ set to zero (dashed line). In the case $g(t) \propto \alpha/t$ we account for both the RM instability due to the shock and the RT instability due to the deceleration, while in the case $g(t) = 0$ we ignore the deceleration and show the prediction for the pure RM case. In the case $g(t) = 0$, Equation 4.3 reduces to

$$\dot{u}(t) = -c_D u(t)^2/\lambda, \tag{4.10}$$

which has the solution

$$u(t) = -\frac{\lambda}{c_D t}. \tag{4.11}$$

The RM plus RT case predicts the velocity difference much better than the pure RM case; it appears that the instability growth is partly RM-driven and partly RT-driven. In general, then, potential flow theory appears to describe the undecompressed peak-to-valley velocity, while a modification of the Ott thin shell theory appears to describe the bubble velocity at early times. This result can be understood if at early times the thin shell effect is strong, while at later times, the thin shell effect has weakened as the shell

decompresses and widens.

4.5 Numerical differences in fine structure

In Figure 4.11 there is a noticeable difference in the fine structure between the CALE and PROMETHEUS simulations of the Nova Cu-CH_2 experiment. CALE was run with tabular EOS in ALE mode, while PROMETHEUS was run with a fixed rectilinear grid and using ideal gas EOS. The difference in the grids in these two simulations at $t = 30$ ns is shown in Figure 4.13. As we stated in Section 4.3.2, we have investigated the fine structure issue further using CALE, and our investigation suggests that the difference in fine structure is mainly due to stairstepping the initial interface as opposed to representing it as a smooth sinusoid. As we also said in Section 4.3.2, when we run CALE in a similar manner to the manner in which we ran PROMETHEUS, using a fixed orthogonal grid, ideal gas EOS and stairstepped initial interface, shown in Figure 4.11d. The general shape of the interface is now very similar in CALE and PROMETHEUS. Holmes *et al.* [84] have done an experimental and numerical study of RM instability, using three codes, the Automatic Mesh Refinement (AMR) code RAGE, the front tracking code Frontier, and PROMETHEUS. They observed somewhat more fine structure in PROMETHEUS than in the other two codes; we do not know if stairstepping was an issue with the Holmes *et al.* simulations.

We have looked further at this question using CALE alone. We are able to run CALE in a number of different ways. We can use (1) tabular EOS or ideal gas EOS, (2) ALE mode or Eulerian mode, and (3) a smooth interface or a stairstepped initial interface. The difference between a stairstepped and smooth initial interface is shown in Figure 4.16. In fact, there are other options for EOS in CALE, such as an inline (quotidien) EOS, a moving grid (though less flexible than the moving grid in PROMETHEUS), and the initial interface could be represented as a combination of smooth and stairstepped. However, as a first investigation into the fine structure issue, we simply simulate all $2^3 = 8$ combinations of the choices in (1)–(3) above. The result is shown in Figure 4.17 by the shape of the interface at $t = 40$ ns from all of the eight simulations. Parts a–d (the left panels) in Figure 4.17 show the results of the simulations with smooth initial interfaces, while parts e–h (the right panels) show the results of the simulations with stairstepped initial interfaces. Parts a,b,e and f (the top four panels) in Figure 4.17 show simulations

(a) smooth initial interface

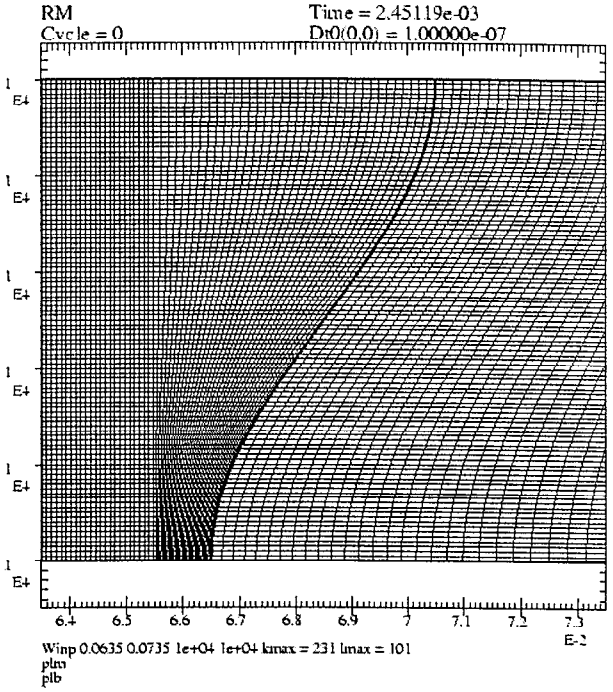

(b) stairstepped initial interface

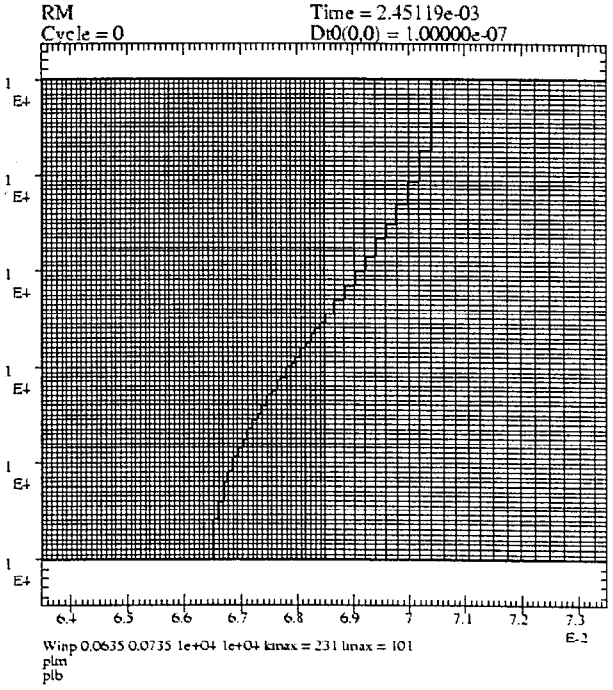

Figure 4.16: Stairstepped vs. smooth initial interface in CALE simulation of Nova Cu-CH_2 experiment.

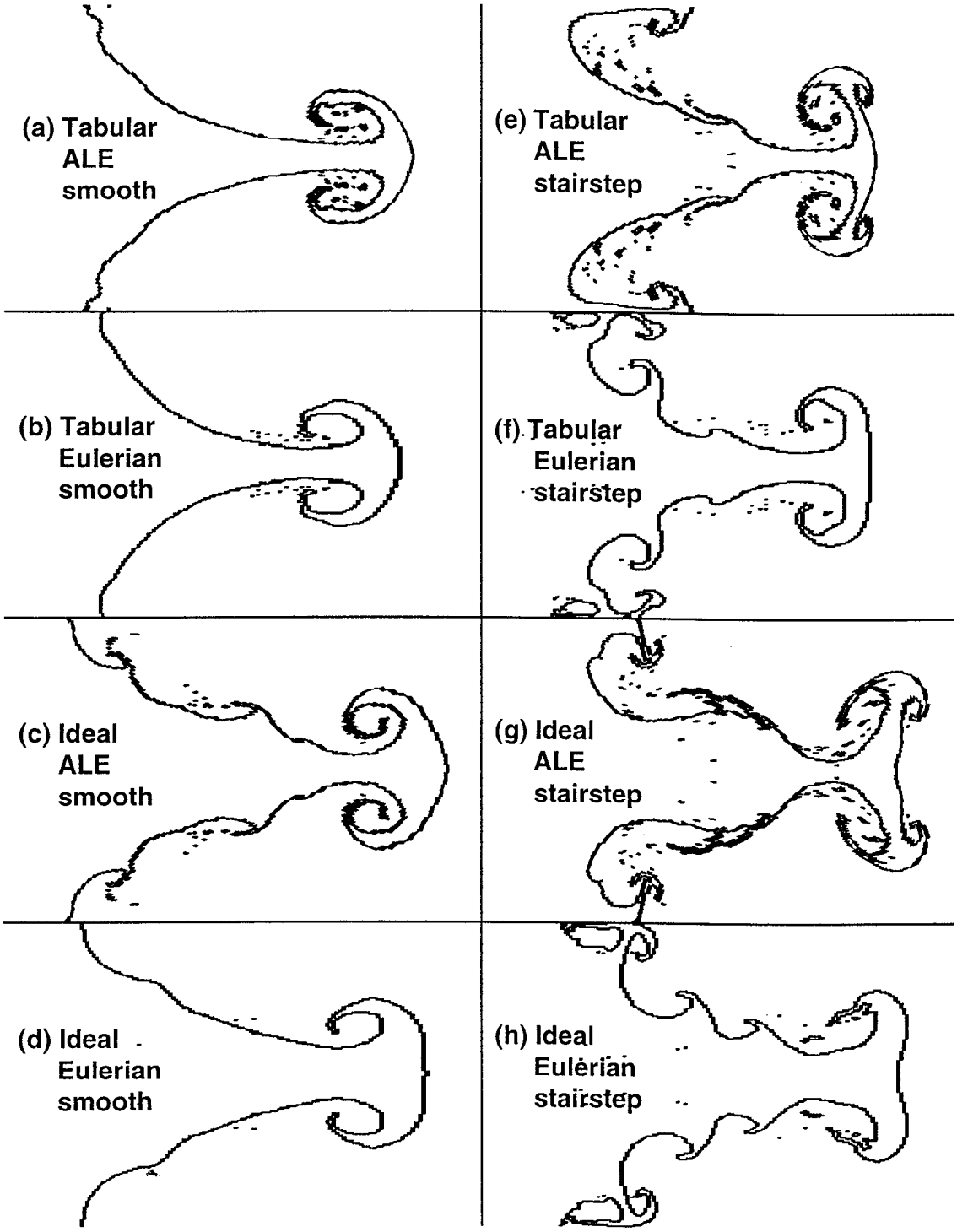

Figure 4.17: Result of using a stairstepped vs. a smooth initial interface in CALE simulations of the Nova Cu-CH_2 experiment. (a)–(d) smooth initial interface. (e)–(f) stairstepped initial interface. One wavelength (200 μm) of the initial interface is shown.

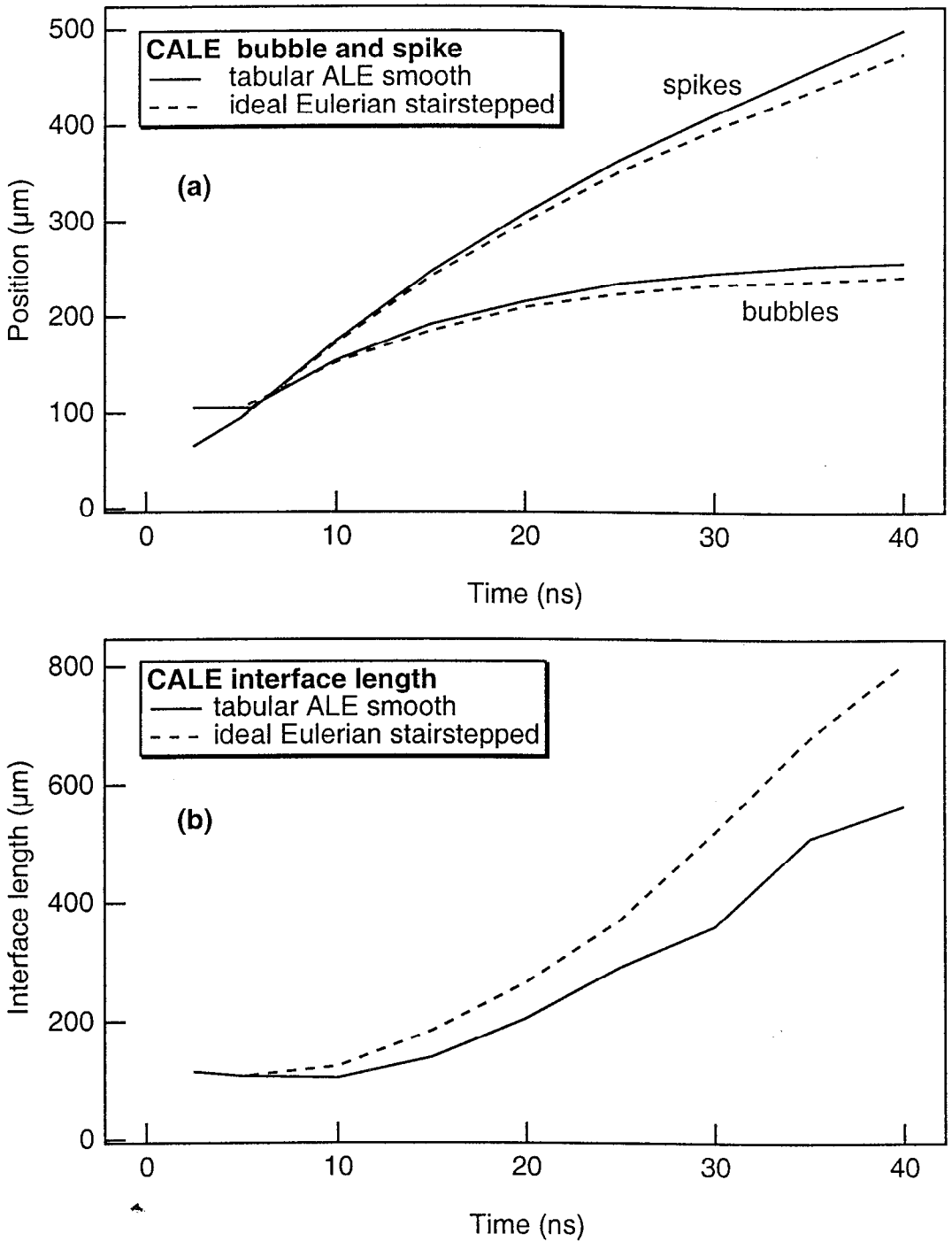

Figure 4.18: (a) Representive range of bubble and spike positions from CALE in the stairstep vs. smooth investigation. (b) Length of interface vs. time for representative simulations.

using tabular EOS, while parts c,d,g and h (the lower four panels) show simulations using ideal gas EOS. Within the tabular EOS simulations, parts a and e are for ALE mode, while parts b and f are for Eulerian mode. Similarly, within the tabular EOS simulations, parts c and g are for ALE mode, while parts d and h are for Eulerian mode.

Thus, the only difference in going from a simulation shown in a panel on the left to the simulation shown next to it on the right is in going from a smooth to a stairstepped initial interface. All of the panels on the left show simulations where the final interface at $t = 40$ ns still has little fine structure, compared to the corresponding simulation on the right, regardless of whether tabular or ideal gas EOS was used, or the simulation was run in ALE mode or Eulerian mode. Even for the case (ideal, ALE, smooth) shown in Figure 4.17c, which has the most fine structure of all the simulations which began with a smooth initial interface, the corresponding simulation on the right, the case (ideal, ALE, stairstep) has significantly more fine structure.

These results suggest that stairstepping the initial interface is indeed the main cause of the extra fine structure seen in Figures 4.11c–d compared to Figure 4.11b. However, the difference in fine structure does not greatly affect the gross hydro, that is, the positions of the bubble and spike tips vs. time. This is shown in Figure 4.18a by a plot of bubble and spike position vs. time for two representative simulations of the eight described above, the cases (tabular, ALE, smooth) and (ideal, Eulerian, stairstepped). The length of the interface vs. time is clearly different for these two interfaces, looking at Figures 4.17a and 4.17h. This is further shown in Figure 4.18b by a plot of interface length vs. time for the two simulations, where interface length is crudely estimated by laying down a thread along the interface at each time and measuring its length. A more precise measurement in the simulation is difficult and somewhat ambiguous, because the interface does not stay connected, and pieces of material break off into islands in the flow. The measurement of the path length in the vortices is also difficult, because there can be considerable length along the edge of a vortex that has rolled up several times. However, this simple measurement should give a reasonable sense of the difference in the length of the interface. The difference in path length could be of interest for processes whose rate is proportional to the area of an interface, such as molecular mixing. It would be of interest to study the difference in path length as a function of resolution, and also to extend this study to 3D simulations, for which the interface surface area would have to be tracked and measured.

CHAPTER 5

FURTHER WORK

5.1 2D vs. 3D hydrodynamics laser experiments

In Section 2.4 we discussed differences in 2D vs. 3D hydrodynamic instabilities in SN 1987A, concentrating on single mode instabilities. In Section 1.3.4.5 we discussed the reason for the differences in 2D vs. 3D hydrodynamic growth. The motivation for studying 2D vs. 3D hydrodynamics was discussed in Section 1.2: the velocities observed for ^{56}Co in the ejecta of SN 1987A are underpredicted in 2D simulations by at least a third. We have begun work on analogous 2D-3D experiments at the Nova laser. In the experiments discussed in Section 4, we used a 2D single mode (sinusoidal) perturbation. 3D numerical simulations are very expensive to carry out routinely, and intractable to carry out routinely at the higher resolutions used in 2D simulations, such as the ones presented in Fig. 4.11b–d. However, a laser experiment with a 3D perturbation is no more difficult to perform than an experiment with a 2D perturbation, and thus offers a useful tool for studying SN-relevant hydro.

We are currently investigating two types of 3D material interface perturbations, designing experiments where we shoot targets with 2D perturbations and targets with 3D perturbations. The different perturbations are illustrated in Figure 5.1. Figure 5.1a shows the form of the 2D perturbation used in the experiment decribed in Section 4.2. We choose the amplitude and wavelength of the perturbations such that the growth rate of the 3D instability is the same as the growth rate of the 2D instability in the linear regime. The difference in growth occurs in the nonlinear regime. The reasoning here follows the discussion in Section 2.4.1.

The first type of 3D perturbation, the 'eggcrate' or 'crosshatch' pattern, is shown in Figure 5.1b. It has the form

$$x(y,z) = \eta_0 \sin(k_3 y) \times \sin(k_3 z), \tag{5.1}$$

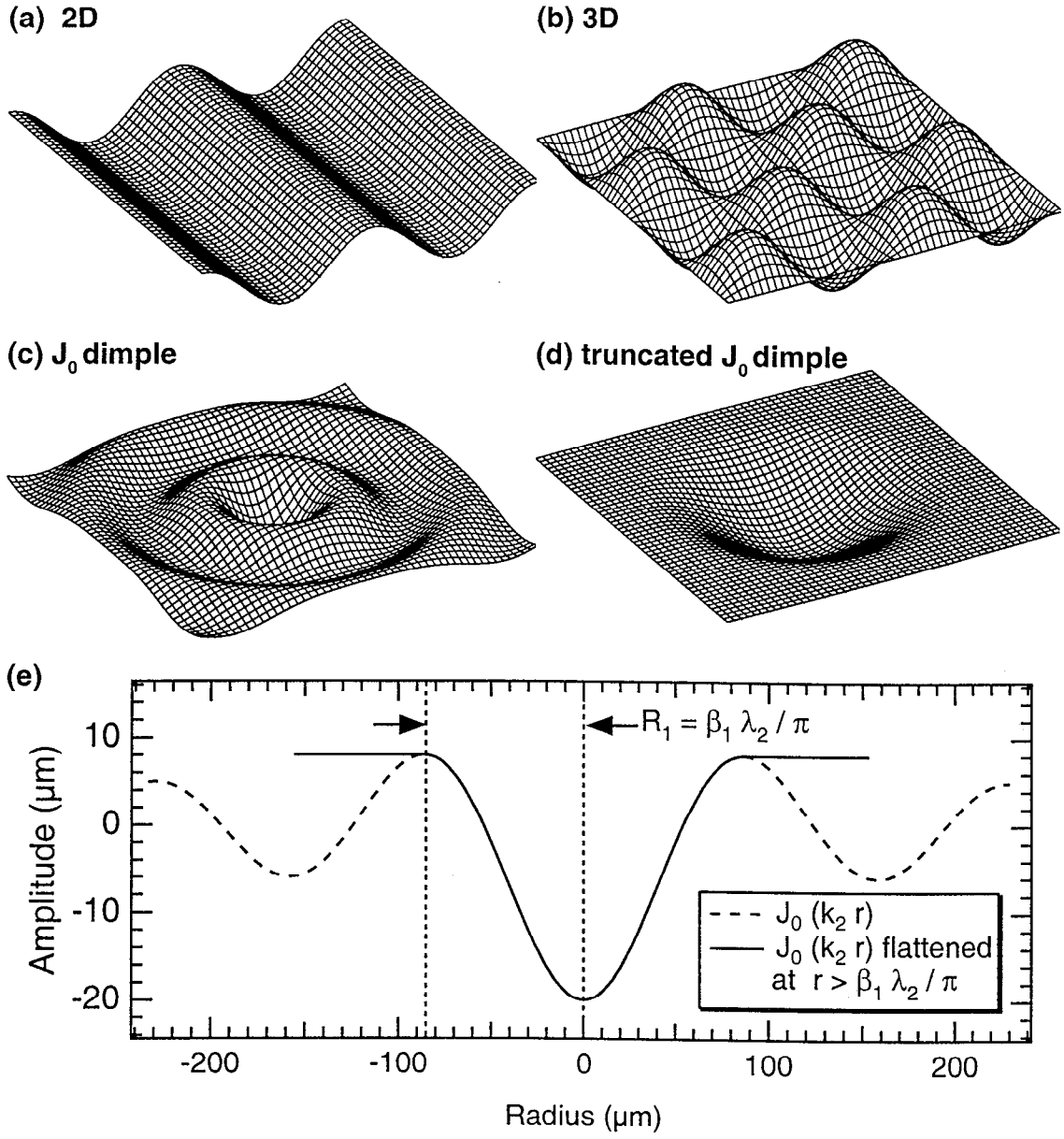

Figure 5.1: 2D vs. 3D material interface perturbations. (a) 2D sinusoidal perturbation. (b) 3D crosshatch perturbation. (c) Bessel dimple perturbation. (d) Truncated (flattened) Bessel dimple perturbation. (e) Amplitude vs. radius for Bessel dimple perturbations.

where x is the coordinate direction perpendicular to the unperturbed interface, y and z are the coordinate directions parallel to the unperturbed interface, and $k_3 = 2\pi/\lambda_3$ is the wavenumber of the single mode perturbation of wavelength λ_3. We choose $2k_3^2 = k_2^2$, where $k_2 = 2\pi/\lambda_2$ is the wavenumber of the 2D perturbation of wavelength λ_2. That is, $\lambda_3 = \sqrt{2} \times \lambda_2$. The amplitude of the perturbation, η_0, is the same in 2D and 3D. These choices gives the same 2D and 3D growth rates in the linear regime (see Refs. [51, 81, 107] and see the discussion in Section 1.3.4.5).

The second type of perturbation, the 'dimple' pattern, is shown in Figure 5.1c. It has the form

$$z(r) = -\eta_0 J_0(k_2 r), \tag{5.2}$$

where the coordinates are cylindrical (r, z), z now being the direction perpendicular to the interface, and r being the distance from the axis of symmetry. The minus sign means that there will initially be a dimple on-axis; this dimple will be inverted by the RM instability into an axially symmetric 3D spike. The next 'ring' out, initially a peak, will be inverted into a bubble ring. To produce the same growth rate for the dimple as for the 2D perturbation, in the linear regime, we use the same wavenumber $k = k_2$ for the Bessel perturbation as for the 2D perturbation (see Refs. [51, 81].) We define the radius R_1 of the dimple as the first peak of $J_0(k_2 r)$, the first zero of the first derivative with respect to r of $-J_0(k_2 r)$, which is $J_1(k_2 r)$. The radius R_1 is larger than $\lambda_2/2$ by a factor of about 1.22 (that is, the diameter of the dimple is about 1.22 λ_2), as follows. The zeros of $J_1(k_2 r)$ occur at $kr = 0$ and at $k_2 r = \beta_1, \beta_2, \beta_3, \beta_4 \ldots \approx 3.8317, 7.0156, 10.1735, 13.3237, \ldots$. Thus the radius R_1 of the dimple is given by

$$R_1 = \beta_1/k_2 = \frac{\beta_1 \lambda}{2\pi} \approx \frac{3.8317}{2\pi}\lambda_2 \approx 1.22\ \lambda_2/2. \tag{5.3}$$

Experimentally, it is desirable to use only the central portion of the Bessel function out to $r = R_1$, as shown in Figure 5.1d. In this perturbation the profile has been flattened past $r = R_1$, as shown in Figure 5.1e. The reason for doing this is that the outer rings of the perturbation will grow as (2D) spikes and bubbles which will obscure the view of the central spike in a side-in radiograph (see Section 4.2). Flattening the outer rings will change the hydrodynamics of the instability somewhat. However, we have simulated targets in CALE both with and without the outer rings, and found no significant difference in the hydrodynamics of the central spike and bubble ring between

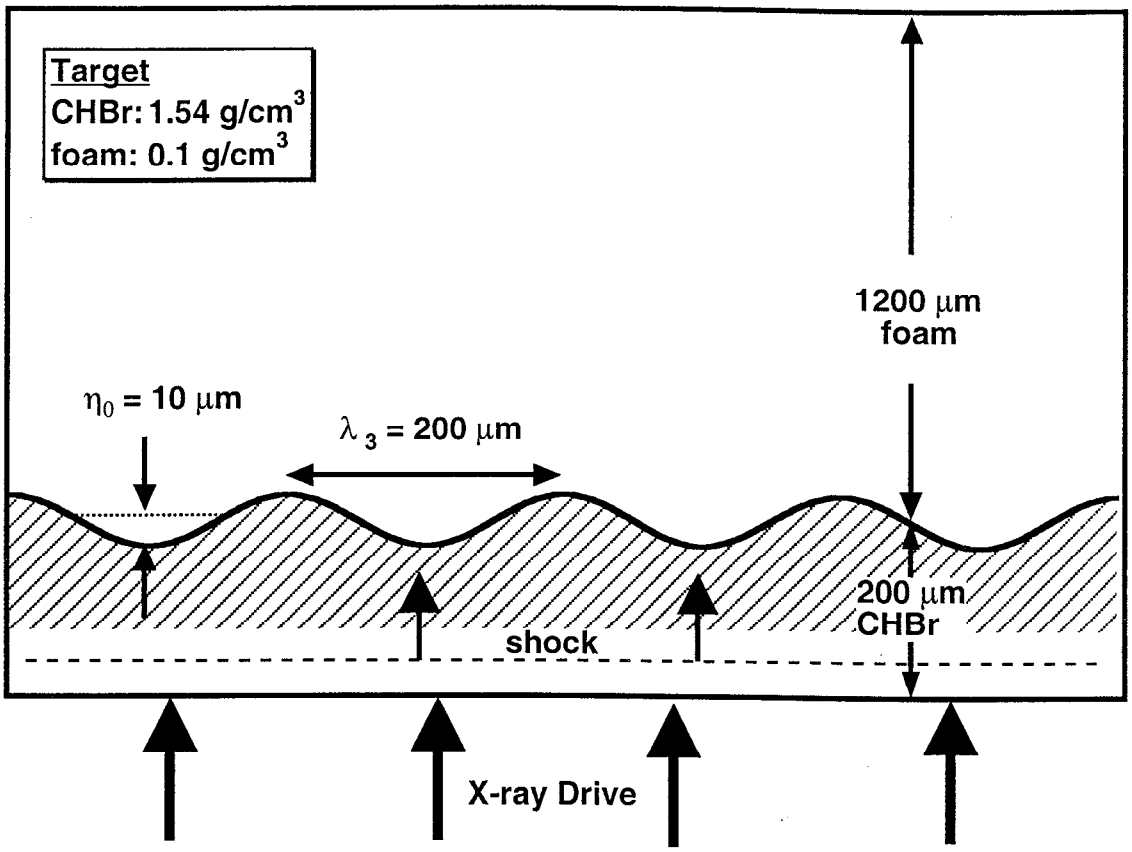

Figure 5.2: Target for two layer Nova experiment with CHBr and foam.

the two cases. This suggests that during the time of interest in the experiment, little information is transmitted from the outer rings to the central bubble and spike that would change the evolution of the latter.

In the first set of experiments, we use targets with the 2D and 3D perturbations shown in Figures 5.1a and 5.1b. The target is a planar two-layer target, the same as the Cu-CH_2 target which was discussed in Section 4.2, and shown in Figure 4.2. The target described here is shown schematically in Figure 5.2. The materials in the target are now different; we use 6% brominated plastic, CHBr, with molecular formula C_50:H_44:Br_6, as the dense material instead of Cu, and we use a foam with molecular formula C_3:H_3:0_1, as the light material, instead of CH_2. The Br serves two purposes. First, it absorbs wavelengths of the x-ray drive which could penetrate well beyond the ablation front and preheat the target. Second, it absorbs the backlighter x-rays more strongly, which improves the quality of the radiographs. The density of the CHBr is 1.54 g/cm^3, and the density of the foam is 0.10

g/cm^3. In our simulations, this choice of foam density gives about the same post-shock Atwood number, $A^* \approx 0.65$, as we had in the Cu-CH_2 experiment. The thickness of the CHBr is 200 μm, as compared to 85 μm in the Cu-CH_2 experiment shown in Figure 4.2. We use a thicker layer here because the shock travels faster in the CHBr than in the Cu, and we want the hydrodynamics near the interface to become decoupled from the drive by the time the shock has crossed the CHBr, similar to what we had with the Cu-CH_2 experiment. The thicker layer also ensures that there will be virtually no preheating of the materials near the interface. Thus, with this design we again have an experiment that is hydrodynamics-dominated except near the ablation front.

For the 3D perturbation, we use a wavelength $\lambda_3 = 200\,\mu$m, and for the 2D perturbation, we use a wavelength $\lambda_2 = 200/\sqrt{2}\,\mu$m. Once again, as with the Cu-CH_2 experiment, we begin our simulations with a 1D run in HYADES, stopping now at a mapping time of 3.6 ns. The energy input to HYADES is once again the measure radiation temperature $T_r(t)$ of the x-ray drive coming from the hohlraum. To simulate the 3D experiment after the mapping time, we need a 3D code. Thus, we turn to PROMETHEUS, simulating both the 2D and 3D experiments with this code. We use ideal gas EOS, once again choosing a fixed ideal gas γ for each material such that 1D PROMETHEUS reproduces as closely as possible the shock speed, interface velocity and compression of the materials from HYADES. We use $\gamma_{\rm CHBr} = 56/30$ and $\gamma_{\rm foam} = 45/30$.

In Figure 5.3 we show the results of the PROMETHEUS simulations of the 2D and 3D CHBr-foam experiments. Figure 5.3a shows the CHBr-foam interface at $t = 30$ ns as 3D surface plots. Figure 5.3c show the positions of the bubble and spike tips in the rest frame of the 1D unperturbed interface as calculated by PROMETHEUS, for the two simulations. The interface in the 2D simulation looks similar to what we saw in Section 4.3.2 for the interface in the Cu-CH_2 experiment. In the 3D simulations we can see the narrow finger-like spikes of CHBr bordering the bubbles of foam, and we can see the 2D saddle lines connecting the spikes and separating the bubbles. At this low resolution there is only faint evidence of KH rollups on the saddle lines. The KH rollups on the spike tips also appear to be less well-developed in 3D than in 2D. The 3D spikes grow $\approx$ 30-35% faster in 3D compared to 2D, as we can see in Figure 5.3c. This difference in growth is similar to what we saw in the simulations of the He-H and O-He layers of SN 1987A, in Section 2.4. Thus, we have a hydrodynamics-dominated experiment which can

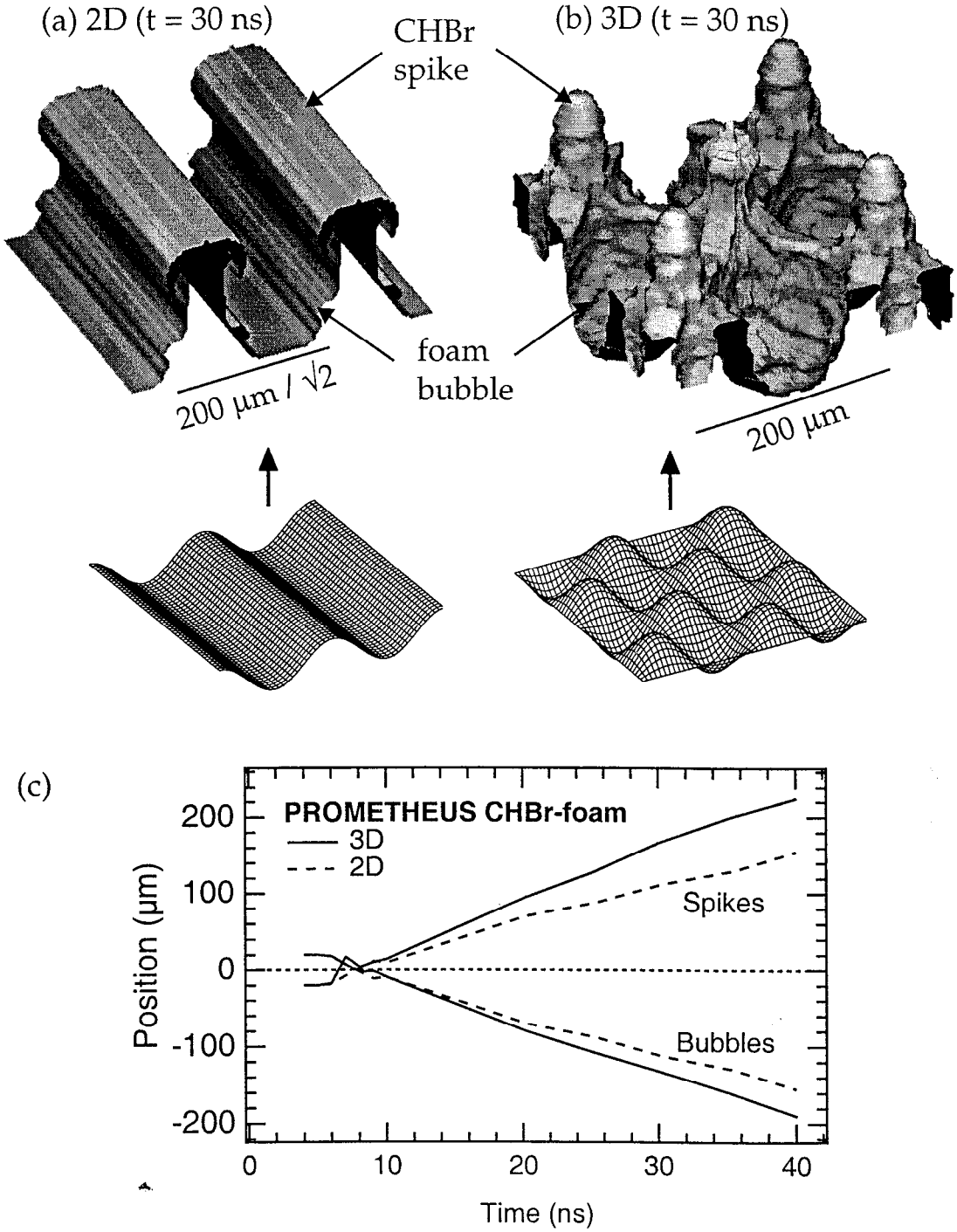

Figure 5.3: PROMETHEUS simulation of CHBr-foam Nova 2D-3D experiment. (a) 2D sinusoidal perturbation at $t = 30$ ns. (b) 3D crosshatch perturbation at $t = 30$ ns. (c) Bubble and spike positions vs. time.

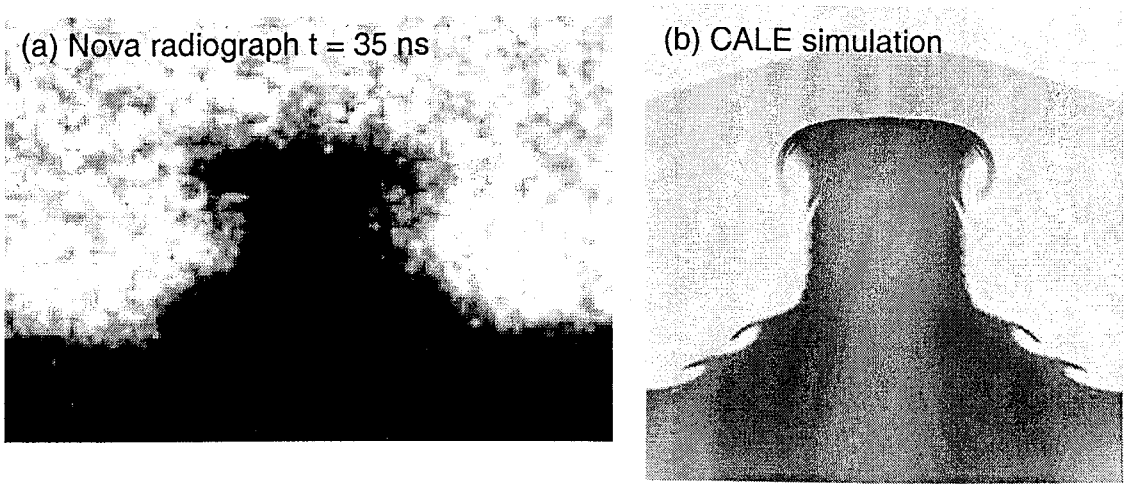

Figure 5.4: Nova Cu-CH_2 experiment using a dimple perturbation. (a) Radiograph from a Nova shot. (b) CALE simulation of a similar experiment.

potentially be used to study the difference in 2D vs. 3D hydrodynamic instability growth that occurs in SNe.

To date, several preliminary shots of the CHBr-foam 3D crosshatch vs. 2D sinusoid have been performed. Initial results were encouraging: finger-like structures of CHBr were imaged for both the 2D and 3D targets. However, the data were not of sufficient quality to allow a quantitative analysis of bubble and spike positions.

We have also shot preliminary Cu-CH_2 targets in which we use a truncated dimple perturbation like the one shown in Figure 5.1d. The side-on radiograph from one of the shots is shown in Figure 5.4a. Figure 5.4b shows a CALE simulation of a similar target, but of smaller dimple radius and amplitude. In the CALE simulation, density is plotted as a color scale intended to be qualitatively suggestive of the measure of optical depth which the radiograph supplies. In the CALE simulation, the shock is visible ahead of the spike tip; it is being bowed by the very fast growing spike.

For the experiment, 16 simultaneous radiographs were taken at $t = 33$ ns. Each of the 16 radiographs corresponded to one of the sixteen pinholes of the gated x-ray camera. As a result, each image was taken from a slightly different angle. The sixteen images were combined numerically, subtracting out the background noise in the numerical procedure. Because of this procedure, the fine structure at the tip vortex has now become visible in the radiograph in 5.4a, and is in good qualitative agreement with the type of structure

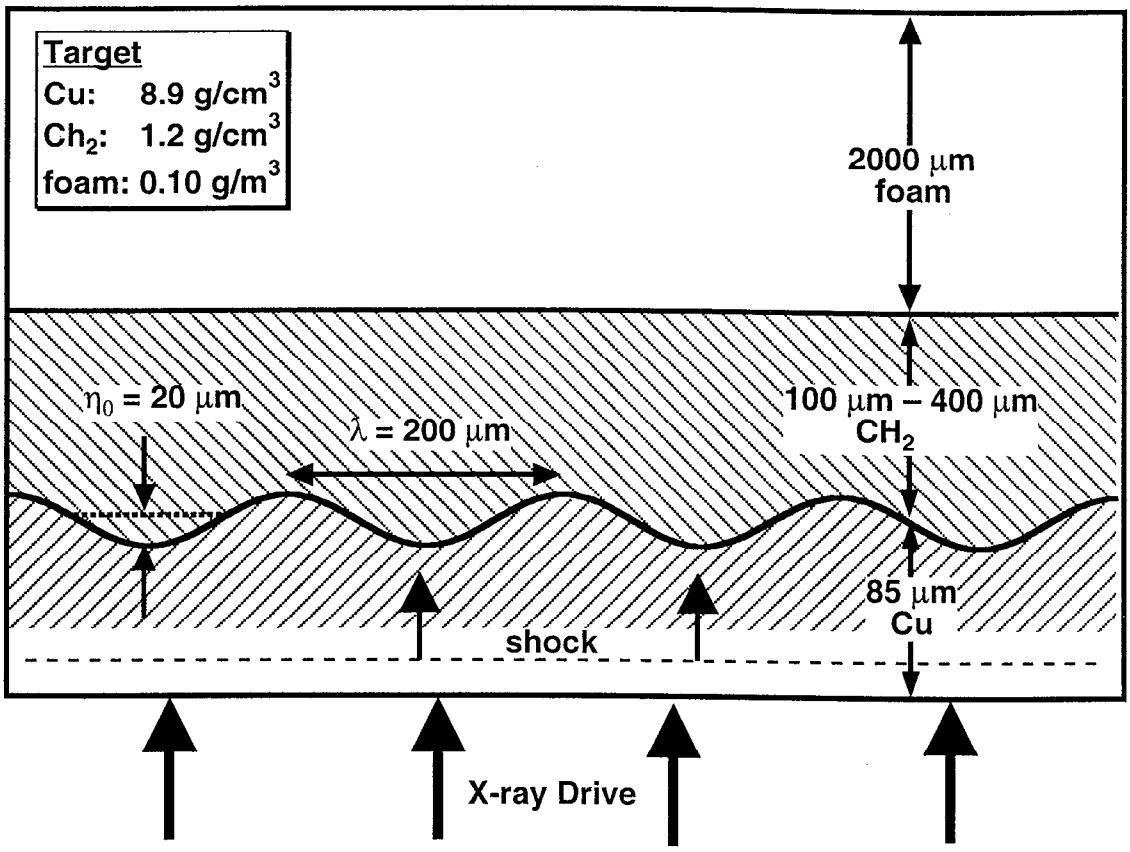

Figure 5.5: Design of a direct drive three layer laser experiment.

seen in the CALE simulation in Figure 5.4b. This technique offers the hope of beginning to examine the fine structure issue, discussed in Section 4.5, experimentally.

A campaign of Cu-CH_2 shots with sinusoid and dimple perturbations is scheduled for the Phebus laser in France (see Section 1.4.2.4) for March, 1999, by Romain Teyssier and collaborators [146]. The goal of this campaign is to systematically study the 2D vs. 3D difference in growth, by using the same wavenumber k_s and amplitude η_0 for the sinusoid and the dimple, as discussed in this section.

5.2 Multiple-layer experiments

An important aspect of the hydrodynamics in SN 1987A may be the coupling of instabilities between layers, as we saw in Section 2.4.2. As a first step in studying such coupling, we are designing laser experiments with three-layer planar targets. These experiments are scheduled for the OMEGA laser (see Section 1.4.2.1) at the University of Rochester

in June, 1999. Our goal in these experiments is to study the imprinting ('feedthrough') of a perturbation from one interface to another. The target for the experiment is shown schematically in Figure 5.5. We extend and adapt the Cu-CH_2 target discussed in Section 4.2, adding a third layer of foam, of lower density than the CH_2. At the Cu-CH_2 interface, we once again impose a single mode perturbation, such as sinusoid, crosshatch or dimple (see Figure 5.1). The second interface, the CH_2-foam interface, is flat.

When the shock passes through the Cu-CH_2 interface, it is perturbed by the material interface perturbation. The shock speeds up in the lighter CH_2; as a result, the part of the shock which hits the valley of the perturbation (the thinnest part of the Cu) moves ahead of the part of the shock which hits the peak of the perturbation (the thickest part of the Cu). The result is a shock which is bowed in shape. Such a shock will oscillate in the CH_2, with the phase of shock inverting after the shock has traveled a distance approximately equal to one wavelength λ of the perturbation. The amplitude of the shock becomes damped over time. The amplitude changes with time approximately proportional to the Bessel function $J_0(\beta_1 x/\lambda)$, where x is the coordinate direction perpendicular to the unperturbed interface, and $\beta_1 \approx 3.83$ is the first zero of J_1 (see Ref. [117]). The perturbed shock then hits the CH_2-foam interface, and imprints a perturbation onto that interface in the same phase as the shock. By the RM inversion, the spike at the Cu-CH_2 interface will grow in opposite phase to the initial perturbation. After the shock has traveled a distance $\approx \lambda$, it will be in the same phase as the initial perturbation, and so if the flat CH_2-foam interface is at a distance λ from the Cu-CH_2 interface, the shock will produce a perturbation at the CH_2-foam interface which has the same phase as the initial perturbation and which is out of phase with the bubble and spike at the Cu-CH_2 interface. If the CH_2 is thicker still, then the shock will invert once more before hitting the CH_2-foam interface, and the bubbles and spikes at the two interfaces will be in phase.

This phase effect is shown in Figure 5.6 by plots of density and material interfaces from CALE simulations with two different thicknesses of the middle CH_2 layer. In Figure 5.6a–d we show a simulation using a CH_2 thickness of $\Delta x_2 = 200\,\mu$m, and in Figure 5.6e–f we show a simulation using a CH_2 thickness of $\Delta x_2 = 400\,\mu$m. In Figure 5.6a and 5.6a at $t = 2$ ns we can see the shock approaching the initial Cu-CH_2 interface (from the bottom of the plots.) In Figure 5.6b $t = 4$ ns for $\Delta x_2 = 200\,\mu$m, we can see that the Cu-CH_2 interface has inverted by the RM instability, and that the shock is moving

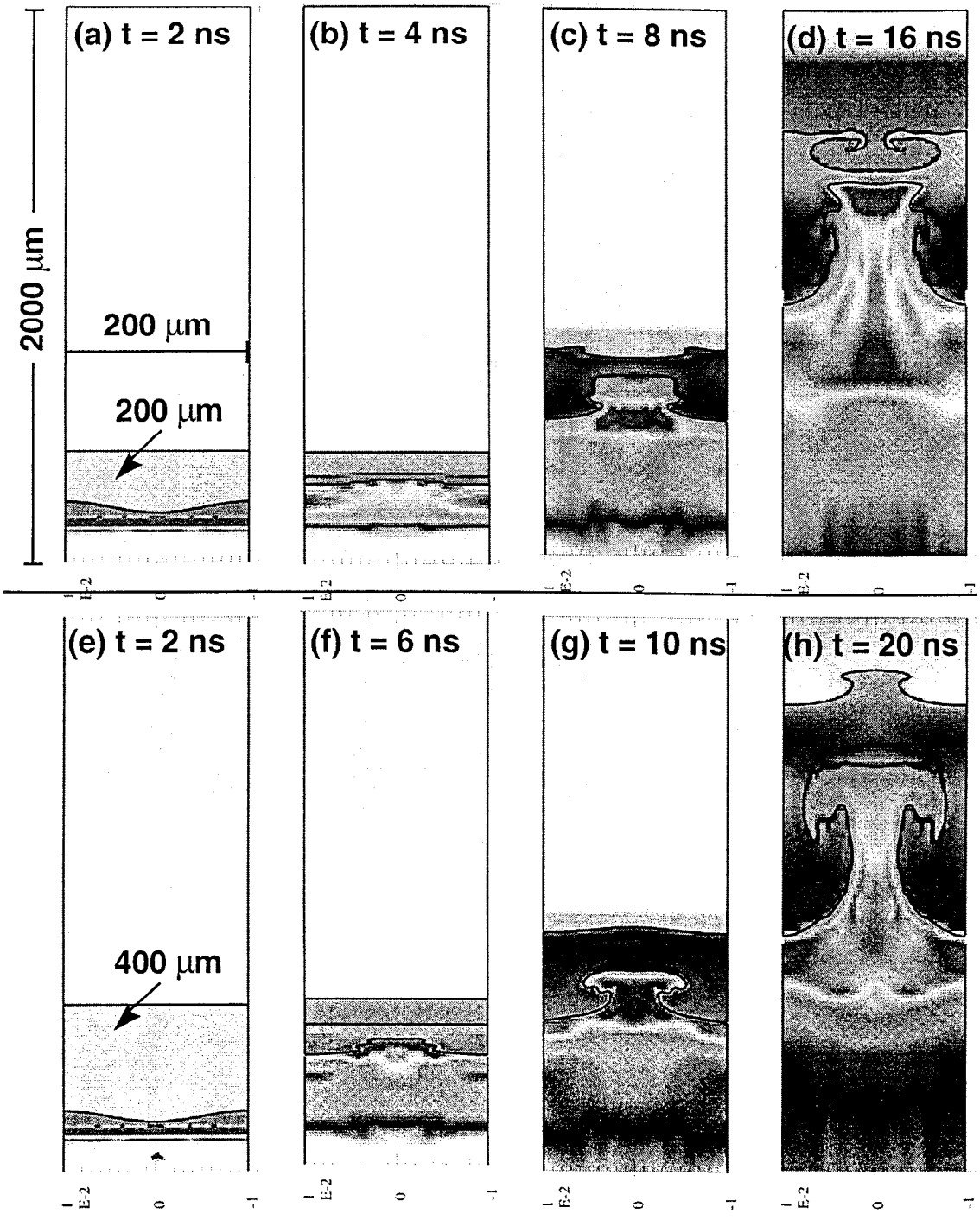

Figure 5.6: Feedthrough in CALE simulation of three-layer laser experiment — imprinting of an oscillating shock from one interface to a second.

towards the CH_2-foam interface. We can see the same in Figure 5.6b at $t = 6$ ns for $\Delta x_2 = 400\,\mu$m. By $t = 8$ ns in Figure 5.6c for $\Delta x_2 = 200\,\mu$m, the shock has passed the CH_2-foam interface and the perturbation at the Cu-CH_2 interface is growing strongly. The shock is visible moving into the foam. The same has occurred by $t = 10$ ns in Figure 5.6g for $\Delta x_2 = 400\,\mu$m. For $\Delta x_2 = 200\,\mu$m in Figure 5.6c, the phase of the perturbation imprinted at the CH_2-foam interface is opposite to the phase at the Cu-CH_2 interface, while for $\Delta x_2 = 400\,\mu$m in Figure 5.6g, the phase of the perturbation imprinted at the CH_2-foam interface is the same as the phase at the Cu-CH_2 interface. In the experiments at OMEGA, we first hope to see at least the difference in phase at the CH_2-foam interface, and possibly be able to image both interfaces at once.

As mentioned, we could potentially use 3D as well as 2D perturbations at the Cu-CH_2 interface. The 3D spikes should grow more quickly, perhaps significantly changing the perturbation at the CH_2-foam interface. Again, such an effect is of particular interest in light of the difference in 2D vs. 3D hydrodynamics in SN 1987A seen in the PROMETHEUS simulation discussed in Section 2.4.2 and shown in Figure 2.8.

5.3 Three layer divergent geometry experiment

Another important aspect of the hydrodynamics in SNe is the spherical geometry. The experiments we have described so far in Chapter 4 and in this chapter are all in planar geometry. Figure 5.7a shows a CALE simulation of a spherical geometry three layer target with multimode perturbations at the initial interfaces. Material from the lowest layer has been mixed well into the outer layer by the interacting instabilities at the two interfaces. Such mixing is reminiscent of the mixing of the O layer into the H envelope in SN 1987A, illustrated in Figure 2.8 by a PROMETHEUS simulation of SN 1987A, and in 5.7b by an image reproduced from [115] of a PROMETHEUS simulation of SN 1987A. This target is being designed for SN experiments on the National Ignition Facility (NIF), now under construction. This target is again an adaptation of the basic designs discussed in Sections 4.2 and 5.2. We use an inner dense Cu layer, a lighter CH_2 layer and an outer layer of foam. For each interface, we first produced a material interface perturbation of random zone-by-zone amplitude up to a maximum amplitude η_0, and then removed short wavelengths and the longest wavelengths from the Fourier spectrum, resulting in a superposition of a range of wavelengths of different amplitudes and random

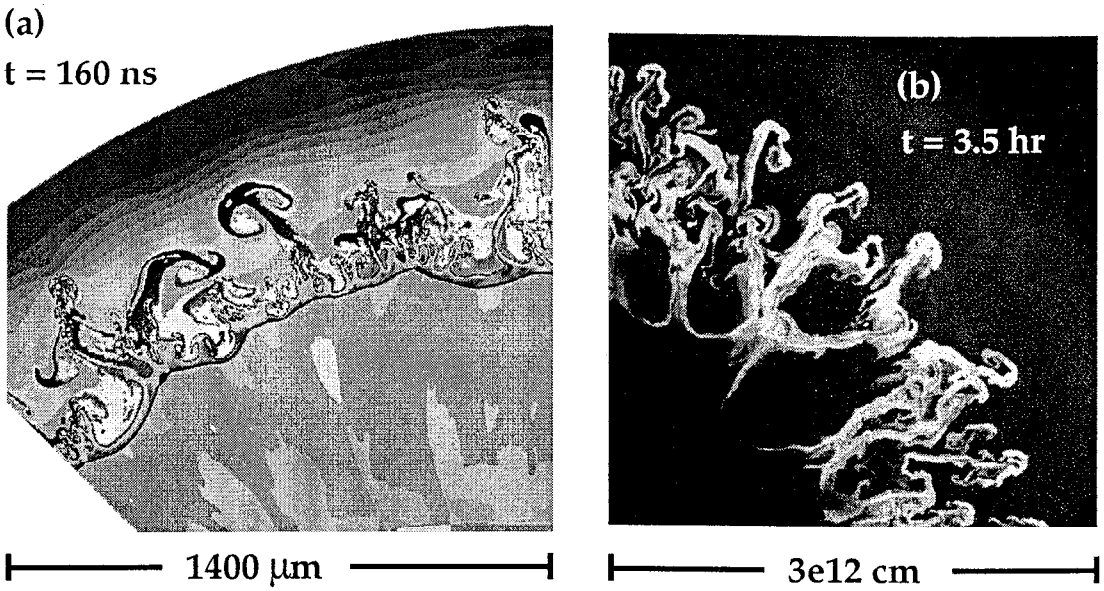

Figure 5.7: (a) CALE simulation of a spherical geometry three layer target with multi-mode perturbations at the initial interfaces (b) PROMETHEUS simulation of SN 1987A. Reproduced from [115].

phases. The initial inner radius of the Cu was 800 μm. The thicknesses of the Cu, CH_2 and foam layers were 85 μm, 120 μm and 2000 μm, respectively. In such an experiment, the target expands considerably, so that the optical depth of the material being imaged goes down significantly (such expansion is desirable, since it also occurs in SNe). Hence, these experiments will present challenges to our diagnostic skills. The energy delivered to the target by NIF will be on the order of 40 times as much as at Nova. This much higher energy is needed to produce a shock strong enough to cause considerable mixing in the experiment discussed here.

CHAPTER 6
CONCLUSIONS

We have presented experiments at the Nova laser and other large lasers whose hydrodynamics are scalable to the hydrodynamics of SNe. A key motivation in doing these experiments was observations of SN 1987A, which implicated hydrodynamic mixing in the explosion, and suggested the possible importance of 3D hydrodynamics in the explosion. We have shown that these experiments can be used to test the modeling of multidimensional hydrodynamic instabilities in hydrodynamics codes used by astrophysicists to model SNe, and demonstrated how these experiments could be used to study difficult-to-model issues in SNe, such as the difference between 2D and 3D hydrodynamics.

We have numerically explored the difference in single mode 2D vs. 3D hydrodynamics in SN 1987A using the SN hydrodynamics code PROMETHEUS, and found that the hydrodynamics of single mode instabilities may be a significantly different in 3D compared to 2D. We have shown in detail why the hydrodynamics at intermediate times in SN 1987A (after the input of energy from the collapse and rebound of the core) scale to the hydrodynamics in the laser experiments at intermediate times (after the input of energy from the laser); the reason is that both scenarios are described well by the pure compressible hydro equations — the Euler equations. Our first laser experiments were in planar geometry, with targets composed of two layers of different and constant density, and with controlled 2D material perturbations at the interface between the two layers. The passage of the laser-induced shock produced RM and RT instabilities, similar to what is seen in PROMETHEUS simulations of SN 1987A. We showed that the hydrodynamics codes CALE and PROMETHEUS can reproduce the gross 2D hydrodynamics in these experiments, that is, the bubble and spike positions vs. time, although there are differences in the fine structure predicted by the two codes. We presented analytic theory that appears to describe the velocities of the bubble and spike tips in these planar experiments. We used the Meyer-Blewett theory for the post-shock conditions at the interface, and used potential flow theory and our modified version of the Ott thin shell theory to

describe the growth of the bubbles and spikes. We have also explored the difference in fine structure predicted by the codes CALE and PROMETHEUS in simulations of the laser experiments, concluding that a stairstepped (as opposed to a piecewise smooth) representation of a single mode interface perturbation is the cause of the fine structure.

We have presented further and ongoing work in astrophysics experiments on large lasers, and also explored the RM instability in SNRs. One direction in further experiments is to study 2D vs. 3D hydrodynamics in laser experiments. Other directions involve including more aspects of the actual SN progenitor star in the laser target, including multiple layers, density gradients, spherical geometry, and multimode perturbations. An important direction in further work will be developing theory to account for the instability growth in these more advanced targets, accounting in particular for the effect of spherical geometry. The scaling arguments presented in Ch. 3 should be improved to account for the difference in geometry between the SN modeled in Ch. 2 and the planar experiments described in Ch. 4. However, these improvements to the scaling argument may become moot once we are able to use the advanced spherical targets at high powered future lasers like the National Ignition Facility.

APPENDIX A

RICHTMEYER-MESHKOV HYDRODYNAMIC INSTABILITIES IN SNR FORMATION

A.1 Richtmeyer-Meshkov hydrodynamic instabilities in SNR formation

A.1.1 Overview

We present an initial evaluation of the role of the Richtmyer-Meshkov (RM) instability in supernova remnant (SNR) formation. Although the Rayleigh-Taylor (RT) instability is most often considered in the canonical picture of SNR formation, the theoretical penetration depths for the RM instability suggest that it could play a significant role in the early stages of SNR formation. We have used the code PROMETHEUS to perform a sequence of 2D hydrodynamic simulations in order to test this possibility. Here we discuss a case in which we impose a large perturbation in the expanding ejecta behind the reverse shock. The interaction of the reverse shock with the perturbation produces significant early RM growth, with spikes penetrating from the contact surface to near the forward shock. Then the RM instability weakens, RT growth eventually dominates, and the perturbation of the forward shock diminishes. We conclude that RM instability growth due to the type of perturbation we have studied might contribute to, but alone cannot account for, the observed radio and x-ray structures which extend to the forward shock in such SNRs as SN 1006.

This material was first presented in almost the form shown here in [94]. My main contribution to this work was performing and discussing the PROMETHEUS simulations of SNRs. I also contributed the mention of the polar protrusions from Reference [27], the summary discussion of why conduction and radiation transport are not expected to be important during the stages of the SNR we are studying, from work done by Dmitri Ryutov and Paul Drake in Ref. [134], with myself as third author, and also the summary description of global analysis of instabilities. Paul Drake had the original idea for the

paper and wrote the first draft, contributing most of the observational and theoretical discussion of SNRs, and writing much of the summary of the theory of RM instability. Bruce Remington considerably improved and augmented not only our understanding and description of the RM instability, but also the flow of the text, suggesting the description of global instability and the discussion of conduction and radiation transport, to which discussion he also contributed as a coauthor in Ref. [134], and adding the discussion of the mixing layer evolution of the SNR, in particular the description of bubble merger dynamics.

Although this work is somewhat tangential to the main work described in this dissertation, that is, developing and analyzing scalable laboratory astrophysics experiments (but see the discussion of SNR-relevant laser experiments in Section B.2 and the scaling arguments in [134]), doing the simulations and tackling the theoretical material in this paper proved invaluable for the main work. The SNR problem led me to some insight into the nature and structure of spherical explosions, and the structure commonly seen in such explosions: unshocked ejecta; reverse shock; shocked ejecta; contact discontinuity; shocked medium; forward shock; unshocked medium. Furthermore, to simulate this problem I first had to become considerably more sophisticated in my methods than I had to be to do simulations in planar geometry. I was forced to use the moving grid, a tool which requires some care to employ, and to develop robust methods of tracking the shock. The moving grid in turn proved essential for simulating the intermediate stages of the explosion of SN 1987A (Ch. 2). Furthermore, in the course of doing this work, I was forced to confront and expose a serious 'bug' in the version of PROMETHEUS I had obtained; the artificial viscosity was formulated incorrectly for spherical geometry. I discovered this bug when I found that PROMETHEUS was unable to calculate a single mode hydrodynamic instability; the spike and bubble structure rapidly broke up into a mass of fine structure. This bug had prevented me from simulating single mode instabilities in SN 1987A much earlier in my dissertation, and considerably delayed these important simulations. Finally, by showing that CALE was able to grow single mode instabilities as expected in spherical problems where PROMETHEUS was not, I was able to rally interest in the problem and obtain a corrected version of the artificial viscosity from Ewald Müller, coauthor of PROMETHEUS. This corrected version of the artificial viscosity was also then distributed to other workers who had the older versions of

PROMETHEUS with the incorrect artificial viscosity. The length of time that the bug had gone undetected was a testament to the tremendous complexity of the PPM method.

A.1.2 Introduction

A supernova remnant (SNR) forms as the ejecta from an exploding star expand into the circumstellar medium (CSM). The ejecta, which have initial velocities above 10,000 km/s, drive a blast wave out through the CSM, producing a forward shock in the CSM, a contact surface between the ejecta and the shocked CSM, a region of shocked and stagnated ejecta, and a reverse shock in the ejecta. In the first phase of SNR formation, this entire structure moves outward. As increasing amounts of matter are swept up, the expanding ejecta are decelerated, producing conditions that may favor the growth of the Rayleigh Taylor (RT) [104, 145] and related hydrodynamic instabilities at the contact surface. It has been thought that the structure observed in young SNRs, including for example Tycho [137, 55] and SN 1006 [123, 129], and anticipated in 1987A [29], reflects in part the development of these instabilities during their expansion. The present paper is written to explore whether the structure of SNRs may be enhanced by the Richtmyer Meshkov (RM) [130, 110] instability which occurs as the forward and reverse shocks progress through the CSM and the ejecta, respectively.

The initial, qualitative, one-dimensional (1D) behavior of a SNR has come to be understood by analyzing the expansion and the subsequent shock structures as self-similar phenomena. The equations for a radial, spherically-symmetric expansion admit self-similar solutions (see Ref. [43]). The radii of the reverse shock, the contact discontinuity, and the forward shock are found to have the same time dependence and to remain in a constant ratio to one another. The shocked regions can be subject to hydrodynamic instability growth. In the typical case of an RT-unstable contact surface, spikes of denser ejecta penetrate forward into the less-dense, shocked CSM. From a self-similar, one-dimensional analysis, one can determine the linear regime growth rate of the RT instability within the profile, either by a local analysis, or by a global analysis which may prove more reliable at identifying regions affected by instability (see Ref. [44]). The global analysis assumes that the hydrodynamic variables are perturbed throughout the shocked regions, and assumes that they can be written in a self-similar form which includes an expansion in spherical harmonics and a power-law dependence on time. The exponent in the power

law is then iterated until the Euler equations can be integrated from each shock to the contact discontinuity while satisfying the boundary conditions at all three surfaces. In the global analysis, the forward shock, contact surface and reverse shock can be coupled, so that growth at one surface can distort the other surfaces.

Simulations of RT evolution at the contact discontinuity show multimode spikes that initially grow rapidly towards the forward shock, enter the nonlinear regime, eventually saturate, and fall back toward the contact layer (see Refs. [44]). This behavior differs from the standard nonlinear inverse cascade for steady-state evolution of an RT-unstable interface between incompressible, semi-infinite fluid layers [141, 58, 135]. The difference in RT behavior in the SNR case is due to three effects. (1) The growth is constrained to a finite layer bounded by the forward and reverse shocks. (2) The 1D velocity profile between the forward and reverse shocks is not uniform, but rather slowly decreasing with radius. The latter effects mean that the kinematic drag felt by the spikes growing radially outward from the contact surface increases with the extent of the spike. (3) The shear along the spike tips (and hence Kelvin-Helmoltz instability) also increases with the extent of the spike. These three effects modify the standard Youngs RT mix width evolution [160], where the mix width is $h_{\rm RT} = \alpha A g t^2$, $\alpha \approx 0.05$, $A = (\rho_{\rm h} - \rho_{\rm l})/(\rho_{\rm h} + \rho_{\rm l})$ is the Atwood number, h and l referring to the heavy and light fluids, respectively, and g is the acceleration of the mixing layer.

The mixing layer evolution for the SNR case is analyzed as follows. If the radius of the unstable layer is increasing with $R = t^m$, with $m < 1$, as is thought to be common, then g is proportional to t^{m-2}. The penetration depth of the saturated RT turbulence is found to be (as just discussed) $d \sim 0.05 g t^2 = 0.05 t^m = 0.05 R$. Because the instability is located near the contact discontinuity, whose radius is $< 0.8 R_s$ (from the Chevalier self-similar solution), where R_s is the radius of the forward shock, the RT turbulence is predicted to be confined to a definite volume well behind the forward shock. This conclusion is supported by 2D simulations [44]. In the simulations, as the old spikes fall back toward the contact surface, new ones rise, with the process repeating itself in a dynamic quasi-steady state. A simple explanation is that the dynamics are driven by the bubbles, with the spikes simply acting as the repository for the denser material pushed out of the way by the bubbles. As bubble merger dynamics sets in [141], old dominant bubbles (and consequently their corresponding spike partners) give way to new larger

dominant bubbles, which leads to new dominant spikes. As the old spikes are no longer replenished with material flowing down around the bubble, they give way, and fall back to the contact surface. We believe it is fair to say that the above picture is the standard current view regarding the development of young SNRs.

Jun, Jones and Norman [88] have attempted to address the problem of observed protrusions into the forward shocks of SNRs which conflict with this model. They consider the development of a SNR with an age of about 500 years. A turbulent RT layer is produced by evolving a SNR in the ambient, uniform CSM using ejecta with a power-law density profile. The turbulent RT layer is allowed to interact with a random distribution of dense and local clouds within a uniform CSM. The clouds were assumed to have a density 5 times that of the background CSM, to be randomly distributed in space, and to have radii of 0.05 pc. They find that the interaction with the clouds, and the resulting vorticity, can at times give the RT spikes sufficient additional energy to distort the forward shock. (Previous work with cloud models has included parameterized 1D modeling by Dickel *et al.* [53, 54]. This is a promising approach to the explanation of such phenomena. We note, however, that it does not explain some other discrepancies in the data, discussed below. In addition, we suggest here that the physical system which interacts with any clouds may be different from the RT turbulent layer used to date.

We would like to suggest that the existing analysis may take up the problem of instability at too late a stage in the unstable evolution. Before the system of shocked CSM and shocked ejecta begins the gradual deceleration that produces RT growth, the ejecta and the CSM are first subject to the violent disturbances of the forward shock and the reverse shock, respectively. The impulsive acceleration of the shocks subject the CSM and ejecta to the RM instability [130, 110], which Dimonte [57] (p. 614) describe as follows. "When a shock encounters a fluid discontinuity, reflected and transmitted shocks are generated, which are refracted by any perturbations at the fluid interface. The modulated shocks produce pressure variations in the upstream and downstream fluids that reinforce the initial interface perturbations and cause them to grow." The RM instability can be viewed as the impulsive limit of the RT instability, in the sense that there is an acceleration but that it acts for only a very brief time [130, 110]. Any density structures present in the inital SNR system, including modulations in the radius of the inner edge of the CSM and the outer edge of the ejecta, are subject to growth by the

RM instability. Only later will the resulting turbulence undergo RT growth. However, a simulation which begins with spherically symmetric ejecta and CSM, run on a spherical grid, may not observe the effects of the RM instability, as the perturbations would have to grow from numerical noise and may not grow long enough to be observed. Depending on the treatment of viscosity in a simulation, small structures due to noise which might otherwise grow by RM instability may be stabilized.

Indeed, Borkowski [30] encountered the RM instability when treating a non-spherical bow shock on a spherical grid in the context of the interaction of Kepler's SNR with the interstellar medium (ISM). They identified the resulting grid scale noise as the source of unstable RM growth, and identified that the bow shock might be perturbed by the RM instability. They did not, however, evaluate the impact of this process on the earlier development of the SNR or on the development of structure and shocks within the bow shock. In the realistic case, the ejecta and the CSM are not spherically symmetric. This may give the RM instability a very different role. Because the RM and RT instabilities scale differently, this leads to different expectations regarding the structures that might be observed in the SNR. We explore this in the following.

A.1.3 Theoretical evaluation of penetration depths

The theory of the RM instability has been significantly advanced in recent years (see Refs. [74, 5, 81, 6, 163, 150, 112] and references therein.) Unfortunately, the theory to date has been developed only for incompressible media, and for compressible media which can be considered as incompressible because the velocities of interest (eg. bubble and spike velocities) are much lower than the sound speed.

The behavior of RM in compressible media and the behavior of RM driven by a blast wave of rapidly increasing density remain to be studied. Here we first ask what the implications of incompressible theory would be for the behavior of the RM instability in a developing SNR. Then we discuss the simulations we used to explore the more realistic compressible case and the nonlinear saturation.

The RM instability occurs whether the Atwood number, A, is positive or negative. Here $A = (\rho_2 - \rho_1)/(\rho_2 + \rho_1)$, with the shock propagating from region 1 to region 2. We take $A < 0$ for this discussion, as the ejecta rapidly become more dense than the shocked CSM in the typical case. Our qualitative conclusions would also apply for $A > 0$. When

$A < 0$, a perturbation of [initial] amplitude [η_0] η is predicted [111, 158] and observed [57] to grow in the linear regime by the RM instability as

$$\mathrm{d}\eta/\mathrm{dt} = A^* U k(\eta_0 + \eta_0^*)/2,$$

where k is the wavenumber of the perturbation and A^*, U, and η_0^* are the post-shock Atwood number, interface velocity, and perturbation amplitude, respectively.

The instability rapidly reaches a nonlinear regime, once the amplitude becomes a significant fraction of the wavelength, and this has been an active area of recent study [74, 5, 81, 6]. In the nonlinear limit, the penetration velocity, u_s, for a spike of wavelength λ becomes $u_s \sim -(\lambda/t)\cdot 2|A|/(1-|A|)$, where $t = 0$ when the shock crosses the interface [6]. We take $\lambda = 2\pi R/\ell$, where ℓ is the mode number corresponding to λ. The corresponding lower limit on the penetration depth d for a dominant, imposed perturbation is $d = \log(t/t_0) \cdot (2\pi R/\ell) \cdot 2|A|/(1 - |A|)$. This quantity can approach or may even exceed the position of the forward shock. Physically, the penetration depth for RM cannot outrun the forward shock [57], although the perturbation can distort the shock. For a distribution of modes, one must consider the competition among the modes, which leads to the merging of some bubbles. In this case, theory and simulation indicate [6] that the penetration depth of the RM spikes is $h_S \sim \lambda_0(Ut/\lambda_0)^{\theta_s}$, where λ_0 is the mean initial wavelength of the perturbations and θ_s increases from 0.4 to 1 as A increases from 0 to 1. (The theory was done for $A > 0$, but one would expect similar results for $A < 0$). This penetration depth can clearly be a large fraction of the shocked layer depth. Note that these scalings are very different from those of the RT instability, discussed above. Thus, in the environment of an expanding, young SNR, it would appear that at early times the RM instability may perturb the medium more extensively than the RT instability. This is the case whether a distribution of modes is present or a single mode dominates the response, because of a large local perturbation.

A.1.4 Simulations

To investigate the degree to which this actually might occur in the compressible and radially varying environment of a SNR blast wave, we used PROMETHEUS, a Piecewise Parabolic Method (PPM) [154, 47] code, to simulate the evolution of a young SNR in two dimensions. We have done a number of simulations, one of which we present here.

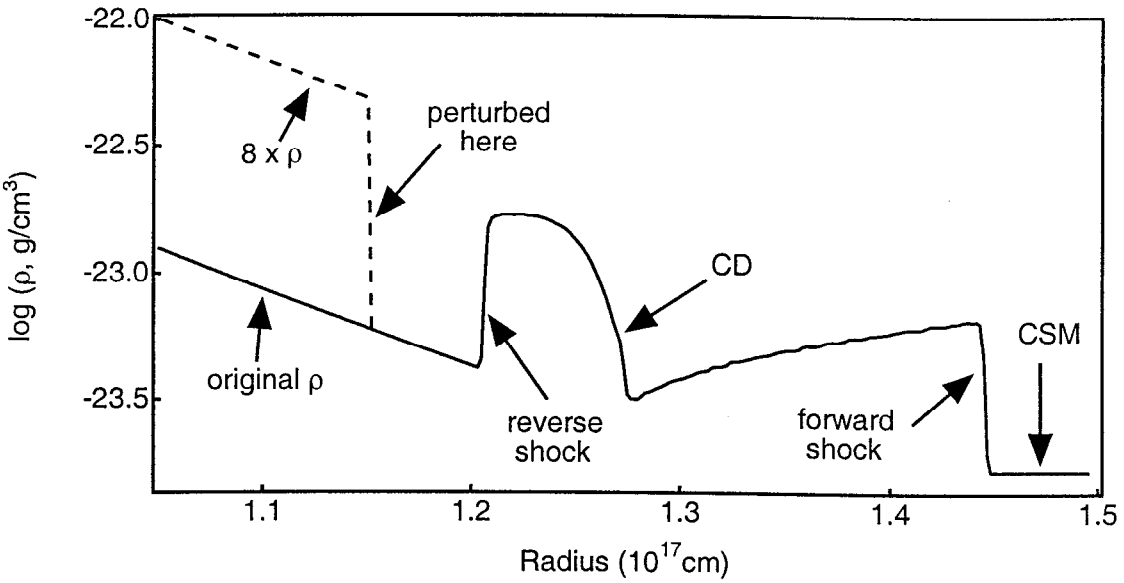

Figure A.1: 1D density profile at 0.6 y, before the 2D perturbation is applied. The solid line shows original density at 0.6 y from the 1D simulation. The dashed line shows the altered, 8 times higher density profile inside the reverse shock. The 2D perturbation will be applied at the new rise. Also indicated are the positions of the forward and reverse shocks, the contact discontinuity (CD), and the unperturbed circumstellar medium (CSM) outside the forward shock.

We initialized the problem spherically (1D), after Refs. [89, 90] and [48], to correspond to a Type Ia SN. The outer 3/7 of the star, of mass 1.4 $M_{\odot}$, has a power law density profile $\rho \sim r^{-m}$, with $m = 8$ in the case we present, and the inner 4/7 of the star has constant density. The explosion energy of 10^{51} ergs is deposited as kinetic energy, with velocity linearly proportional to radius. The background density is chosen to be uniform and equal to 1.67×10^{-24} g/cm^3, and the initial temperature is taken to be 10,000 K throughout. We use a moving grid that expands homologously with the forward shock. We feed in constant density CSM at the radial boundary above the shock, and simulate only the required part of the ejecta, feeding in the exact 1D homologously expanding profile at the radial boundary below the reverse shock. We have 200 zones in the radial direction in the intershock region, and 'squarish' aspect ratio zones ($\Delta r = r\Delta\theta$). As a check on our methods, we first successfully reproduced the 1D and 2D results in Ref. [89]. One would expect that the hydrodynamic code PROMETHEUS would reproduce the results from the MHD code ZEUS for this case, as the magnetic field is not dynamically

significant here.

Likewise, following [134], heat conduction and radiation transport are not expected to be important during the stages of the SNR we are studying, taking into account the expected atomic number, ionization level, densities and temperatures at various times (eg. 1, 10 and 100 years.) To study the effects of heat conduction, we estimate the Peclet number, the ratio of heat convection to heat conduction for electrons, which dominate the heat conduction. We expect magnetic fields on the order of a few μG in a SNR of the ages we are studying [88, 90]. Using this value, along with the expected atomic number, ionization level, densities and temperatures, we can compute expected Peclet numbers for magnetized electrons which turn out to be $\gg 1$ during the times of interest, indicating that heat conduction effects are negligible. Similarly, we can compare the estimated radiation cooling time for the optically thin SNR at these stages, again as functions of atomic number, ionization level, densities and temperatures, and find that the radiative cooling time is much greater than the age of the SNR at any time of interest, indicating that radiation is unimportant.

The simulation discussed here is motivated by the possibility that structure in the ejecta itself might seed RM growth. We start the simulation with the radius of the ejecta, R_e, equal to 5×10^{16} cm, and with equal ejecta and CSM densities at R_e. We first run the problem in 1D with no perturbation, until 0.6 y, by which time a distinct reverse shock–contact discontinuity–forward shock profile has developed, with the reverse shock, contact, and forward shocks at $R_r = 1.2 \times 10^{17}$ cm, $R_c = 1.27 \times 10^{17}$ cm, and $R_f = 1.45 \times 10^{17}$ cm, respectively, as shown by the solid line in Fig. A.1.

We then perturb the additional ejecta flowing into the system in a way that will initiate RM growth. Following a suggestion by G. Bazan, we consider a perturbation in the ejecta below the reverse shock [18]. We choose a perturbation radius $R_p = 1.15 \times 10^{17}$ cm, just inside the reverse shock. We then replace the 1D result with the exact homologously expanding solution that gives 8 times higher density in the ejecta at R_p, as shown by the dotted line in Fig. A.1. That is, we impose a density rise in the ejecta that is about to strike the reverse shock. At this time we map into 2D PROMETHEUS. We impose a mode $\ell = 24$ material perturbation at R_p, with $\eta_0/\lambda_0 = 0.1$. In separate simulations, we also add either a 2% or no zone-by-zone random density perturbation between the two shocks, to see how the usual RT seed perturbations (as in Ref. [89]) break the symmetry.

We simulate 3 wavelengths of the perturbation.

Figure A.2 shows the density structure at 4 times during the simulation of the case with the added 2% density perturbation. Fig. A.2a is a contour plot of density at 0.6 y, the starting time for the 2D simulation, while parts b–d show the same at 7, 10 and 100 years. The sinusoidal perturbation feeds through the reverse shock and perturbs the contact surface, from which spikes develop rapidly, approaching and noticeably perturbing the forward shock by about 7 years. The longest spikes grow at the imposed RM wavelength, and other spikes and rollups grow from nonlinear effects. By 10 years the spikes begin to weaken. By 100 years, the spikes have fallen back toward the contact surface, and the intershock region looks very much like the canonical picture, except for persistent regions of lower density which originated in the vortices at the tips of the inital spikes (isolated white vortices in Fig. A.2d at 100 y.) The result looks very similar at all times when we have no added random density perturbation (not shown); however, in that case the initial imposed symmetry persists slightly longer, and the density fluctuations from the spike tips are slightly more sustained and are closer to the forward shock at 100 years. In both the 2% and the no random perturbation case, the fine RT and Kelvin-Helmholtz structure has noticeably asymmetric features, indicating that numerical noise contributes to seeding the fine structure.

Thus, structure in the ejecta can perturb the forward shock, but only for a limited time. It would appear that the ejecta would have to be very inhomogeneous in order to continuously perturb the forward shock.

We have tried a number of other initial conditions, with (1) a material perturbation either below the reverse shock or above the forward shock, or at the edge of the initial ejecta; (2) both rises and drops in density at the perturbation with (3) density ratios between 2 and 8; (4) mode numbers between 16 and 96; (5) both a 2% and no additional random density perturbation in the intershock region; (6) values of R_e between 5×10^{16} and 3×10^{17} cm. We have also tried a variation of the case presented in detail above, in which we replace the perturbation by isolated hemispherical density enhancements (like dense isolated 'mushroom caps'.) The case we have presented gives the most dramatic RM growth; in most cases we have tried, the spikes do not approach the forward shock, although there is always considerable early penetration of spikes. The added random density perturbation makes no significant difference in any of the results; the RM

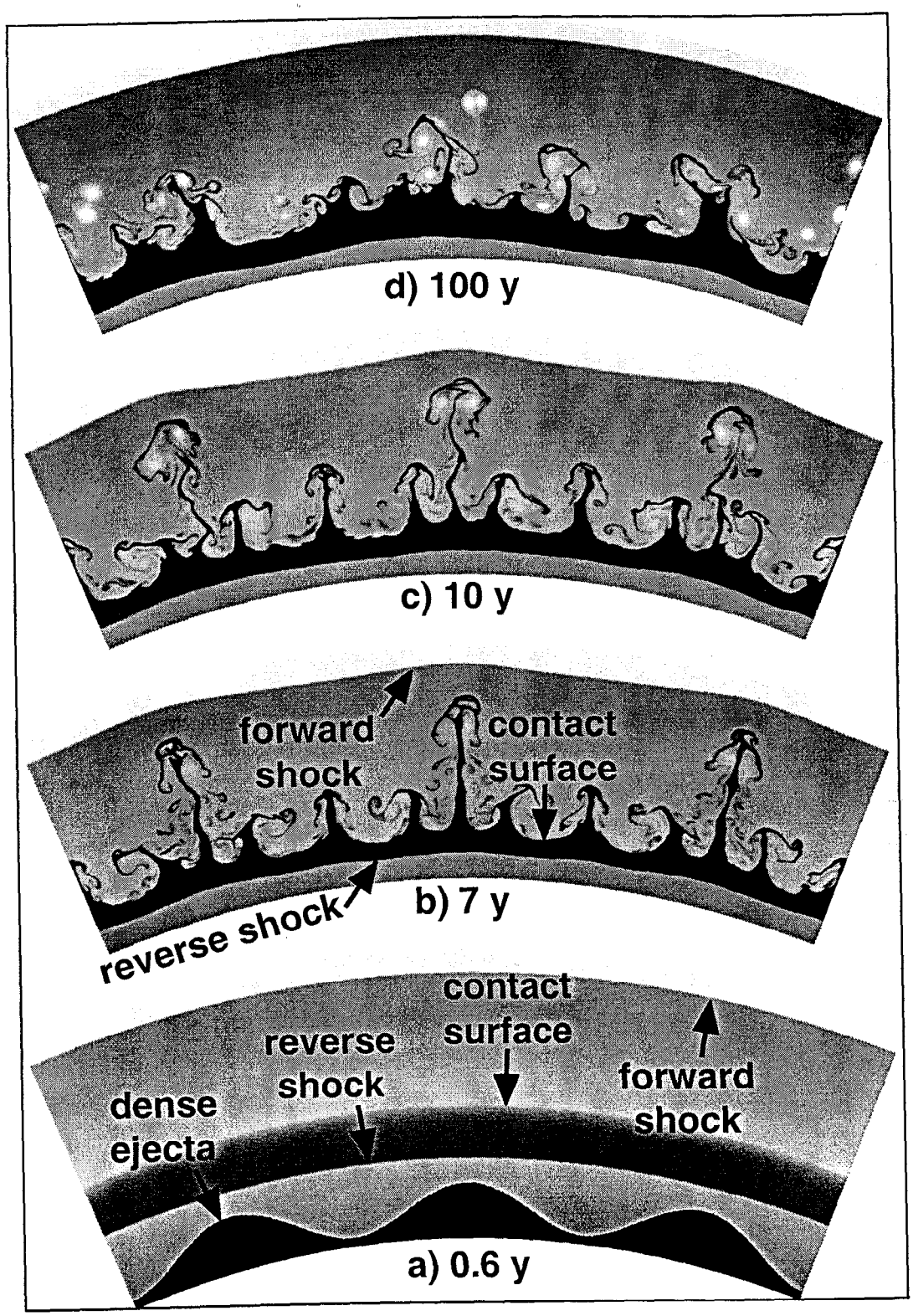

Figure A.2: 2D density structure at 0.6, 7, 10 and 100 y.

perturbation dominates the early growth.

The initial conditions presented above are quite extreme; a density change by a factor of 2 is more realistic for ejecta that has expanded considerably [9]. We conclude that the canonical reverse shock–contact discontinuity–forward shock picture is very robust, at least to the type of perturbations we have examined here. However, these perturbations do produce penetration of the spikes to near the forward shock which endure for a few years, and also produce considerable early mixing of CSM and ejecta in the intershock region.

A.1.5 Discussion of observational data

The RM instability provides a potential explanation for several features in the observational data which are difficult to explain in the standard model. The radio emission and radial magnetic fields in SNRs typically extend to the location interpreted to be the forward shock. This is the case in Tycho (SN 1572); Dickel *et al.* [55] show that the radio emission and radial magnetic field extend to the location interpreted to be the forward shock, even in regions where the x-rays are weak. In SN 1006, the radio [129] and x-ray [123] emissions show the same sharp outer edge, which is interpreted as the forward shock. Reynolds and Gilmore note that the bright radio shell corresponds to the sharp outer edge of the emission, and that the brightness is apparently not due to interaction with a denser external medium, which would result in deceleration that is not observed.

Dickel *et al.* [55] suggest that the radial magnetic field may be produced by RT instabilities along the lines suggested in Refs. [76] and studied recently in Refs. [91] and [90]. However, the RT instabilities cannot penetrate to the forward shock (see Ref. [44]), as discussed above. Jun [90, 91] have observed the production of radial magnetic fields using 3D simulations of RT growth and conclude that "an extra mechanism is required to generate radial magnetic fields at the outer shock front". Our simulations suggest that at early times, the RM instability could transport compressed magnetic flux towards the outer shock front, but also indicate that at later times further mechanisms than the perturbations we have considered in this paper would be needed. One such mechanism could be the later time growth of longer wavelengths from an initial multimode perturbation [6]. Another possible mechanism is a continuous reseeding of the RM instability by clumps in the outer parts of the SN ejecta; such clumps could arise from the nonlinear instability of

the blast wave accelerating in the steep density gradient of the outer envelope [105] and references therein.) We suggest that perhaps the brighter radio regions are a consequence of increased magnetic field compression and transport by the RM instability, in regions whose initial conditions encouraged larger RM growth.

Seward [137] interpret the x-ray data from Tycho to find the same forward shock location, but find evidence that some of the ejecta has penetrated to 0.9 Rs. This is farther than RT models [44] predict (at least in two dimensions) but could be a consequence of RM. In addition, the x-ray emission from the region near the forward shock appears clumpy and not smooth. This could be due to structure in the ambient medium, but any such structure would have been enhanced by the RM instability. To infer the structure in the medium from the observed clumpiness, one must in some sense deconvolve the effect of RM.

A.1.6 Future work and conclusions

Several issues should be addressed in future work on this subject. Fundamental issues include in what ways the RM instability differs in compressible and spatially varying media from the RM instability described by the standard incompressible models with fixed Atwood number. Other work should include quantifying the behavior of the RM instability under the range of conditions believed to be present in various SNRs, including, for example, stellar-wind profiles of the CSM appropriate to the explosion of red supergiant or blue supergiant stars. An evaluation of the observable emissions produced by saturated RM structures should also be undertaken. In addition, it would be valuable to undertake extended simulations to explore the effect of deeply structured ejecta on the forward shock. One option would be to use a calculation of the structures produced during the stellar explosion as an input to the remnant calculation. This all may lead to a clear conclusion as to the degree to which the RM instability can be used as a diagnostic of the irregular structures present in the explosion and/or the pre-SN CSM.

Kepler's SNR offers the potential opportunity to develop and test models of these effects. The observed data from this SNR provide support for a model in which the motion of this SNR in the ISM has produced a significant bow shock [15, 30, 31]. Observations of the SE edge of this remnant can probe the interaction of the blast wave with the bow shock. The structure of the reflected shock within the blast wave can determine whether

or not the blast wave and the shell are smooth, and may provide clues as to the type of structure in each. These issues can potentially be addressed by study of this object with the AXAF observatory.

The forthcoming collision between the developing remnant in SN 1987A and the circumstellar ring there may also provide a definitive opportunity to determine what the structure of the shocked shell is [143, 108]. The much-denser ring will cause definite reflected shocks within the SNR shell [29]. Their timing and structure will show whether or not there is a smooth, unstructured layer behind the forward shock. Further study of this specific interaction would be warranted, so as to better guide the observations.

We note that the RM instability requires only small spatial variations, on the order of a few percent, in the shape of the ejecta or the CSM relative to the blast wave, to generate large structures. Such perturbations are essentially certain to be present. Clouds, meaning local clumps of much denser material, may be present and if so will have consequences similar to those described in Refs. [90] and [91], although the structure which interacts with the clouds will be the consequence of both the RT and RM instabilities.

Blondin *et al.* [27] have considered the case of a CSM with a density variation at the poles, and find that strong protrusions of the intershock region can occur at the poles, which may explain protrusions in VLBI radio images in the remnants 41.9+58 in M82 and SN 1986J. The protrusions seen in Ref. [27] are large scale and dramatic, but suggest that RM instability seeded by initial conditions, and other effects such as the chaneling effect in [88] and some variant of the above protrusion effect, may occasionally combine fortuitously to produce smaller scale protrusions into the forward shock.

In conclusion, it appears as though the Richtmyer-Meshkov instability, because it acts first, may amplify the nonuniformities present in the material which forms a SNR. All of the structures observed in a SNR show us the post-Richtmyer-Meshkov environment. This instability could alter the subsequent development of the SNR, including the development of Rayleigh-Taylor instabilities. Clumps in the emission throughout the forward shock and radial magnetic field structures are two of the likely consequences, though our work would indicate that continuous reseeding of the Richtmyer-Meshkov instability would be necessary to produce this result. It may be that the ejecta are always highly structured, due to instabilities during the explosion, and/or that the CSM is structured due to variations in its source. In this case, the combined impact of Richtmyer-Meshkov

and Rayleigh-Taylor instabilities may imply that the standard model of a SNR should be altered to show a forward shock that is structured througout.

APPENDIX B

CONTEMPORARY WORK IN LASER ASTROPHYSICS

In this Appendix we review some contemporary work in laser astrophysics. Previous work was described in Section 1.5.

B.1 Density gradient experiments

In the initial model of SN 1987A shown in Figure 2.1, we note that in addition to the sharper changes in density at the O-He and He-H interfaces, there is an overall density gradient in the layers of the star (see the discussion in Section 2.2). A shock moving down such a density gradient will proceed faster than if the density were constant; the fluid velocities behind the shock will also be higher. In the laser experiments discussed in this chapter and in Chapter 4, we have used targets with layers of constant densities. There are various ways of producing density gradients in laser targets. Using one such method, Romain Teyssier and collaborators will do a campaign of shots at the OMEGA laser in June, 1999 to study shocks moving in density gradients in planar targets [147]. The design of the target is shown schematically in Figure B.1a. An indirect x-ray laser drive is created by illuminating a thin Au foil with 3 kJ of Omega laser light. This indirect laser drive volumetrically heats one side of a CH target, creating a low-velocity density gradient on that side. Meanwhile, other Omega beams illuminate the other side of the CH, sending a strong shock through the CH which then moves down the density gradient. The evolution of the density in the target from a HYADES simulation of the target is shown in Figure B.1b. The design of the target and the simulation shown were done by Romain Teyssier.

It is possible that at larger lasers like NIF, another effect of the density gradient on the shock could be observed. As the shock moves down the gradient, it heats up, that is, the fluid immediately behind the shock becomes hotter as the shock moves into less and less dense material [152]. With a strong enough shock and a steep enough density

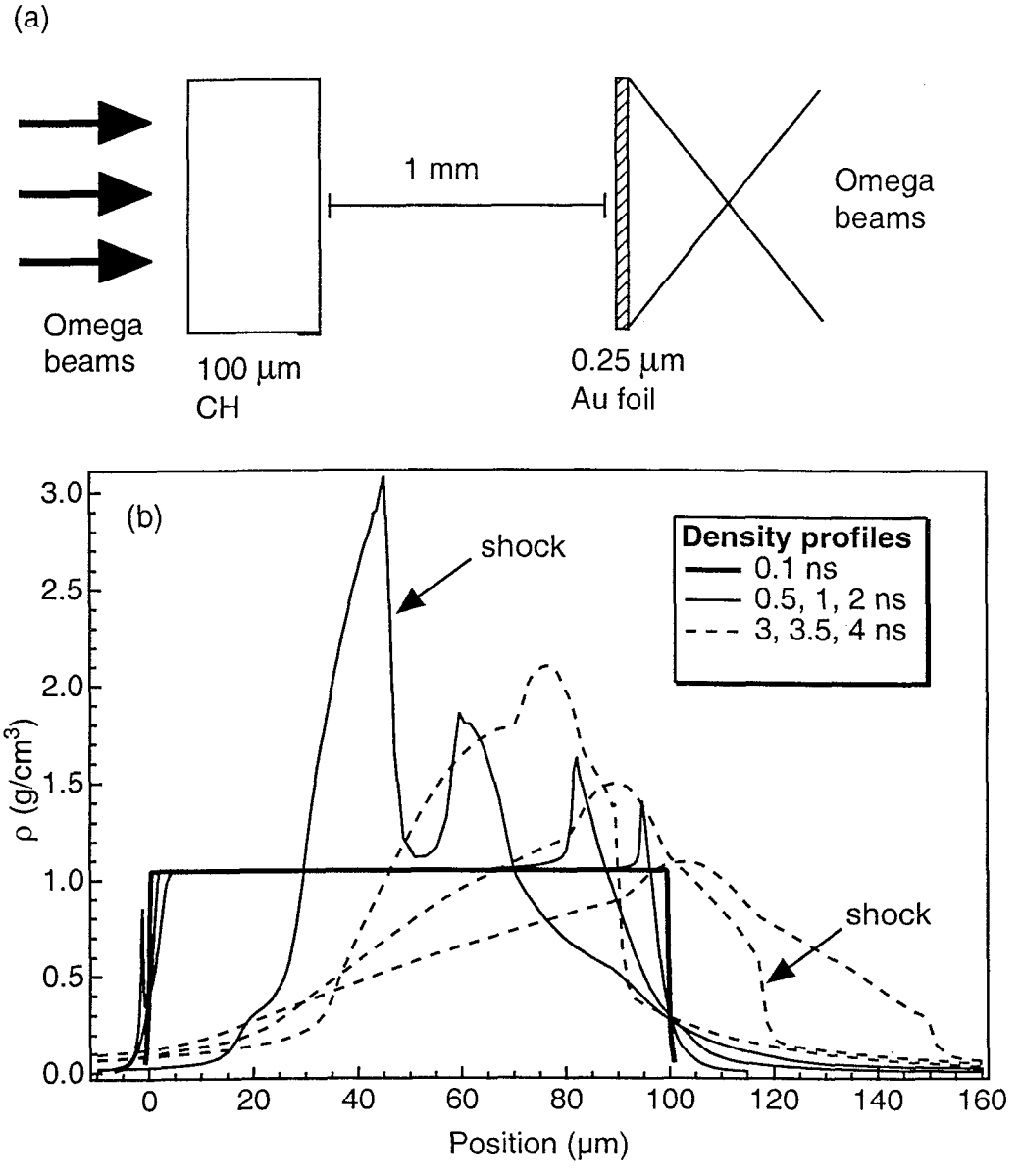

Figure B.1: Density gradient experiment. (a) Schematic of experiment. (b) Density vs. position from 1D HYADES calculation. The heavy solid line is density vs. position at $t = 0.1$ ns. The light solid lines show the formation of the density gradient, at $t = 0.5$, 1, and 2 ns. The dashed lines show the shock moving down the density gradient at $t = 3$, 3.5 and 4 ns.

gradient, such a shock could become radiative. A possible laser experiment would involve producing such a radiating shock and measuring its temperature.

B.2 SNR ring experiments

As the ejecta from SN 1987A expand after the explosion, they encounter first the circumsteller medium (CSM) which surrounded the progenitor star and then the central ring of the famous SN 1987A ring structure [29]. A Hubble Space Telescope image of the the SN 1987A ejecta and ring structure is shown on the right side of Figure B.2a. RM and RT instabilities occur as the ejecta encounters the CSM and the ring (see Appendix A for discussion of simulations of RM instabilities in SNRs.)

An experimental effort has been made at the Nova laser to investigate the hydrodynamics of these encounters [61, 60]. A schematic of the experiment is shown in Figure B.2a and a Hubble Space Telescope image of the SN 1987A ejecta and the ring structure is shown in Figure B.2b. In the experiment, a plastic 'plug' is mounted in a window in the hohlraum, which is an analog to the progenitor of SN 1987A. The x-ray drive from the hohlraum causes a shock wave to propagate through the plug and break out the back side, sending a shower of ejecta off the backside. The ejecta has a power-law density profile, similar to the ejecta from a SN. This ejecta is allowed to cross a void and then interact with a low-density foam, which is an analog to the CSM. Simulations and data appear to suggest formation of an SNR-like double shell structure of shocked ejecta and foam between a reverse and a forward shock, as shown in Figure B.2c by a spatially averaged, time streaked radiograph of optical depth in the target. Figure B.2d shows the averaged optical depth at $t = 6$ ns. RM and RT instabilities occur at the CD between the ejecta and foam. Preliminary data from experiments in which a ripple is placed on the foam surface facing the void to seed the RM and RT instability appear to show the formation of bubbles and spikes at the ejecta-foam CD [70]. In further experiments, the entire assembly of shocked ejecta and foam will be allowed to collide with a further piece of plastic, an analog to the central ring structure of SN 1987A. The actual collision of the SN 1987A ejecta with the central ring is expected to produce a strong display of x-rays, giving astronomers information about the ejecta, ring and forward shock structures and the evolution of the collision [29].

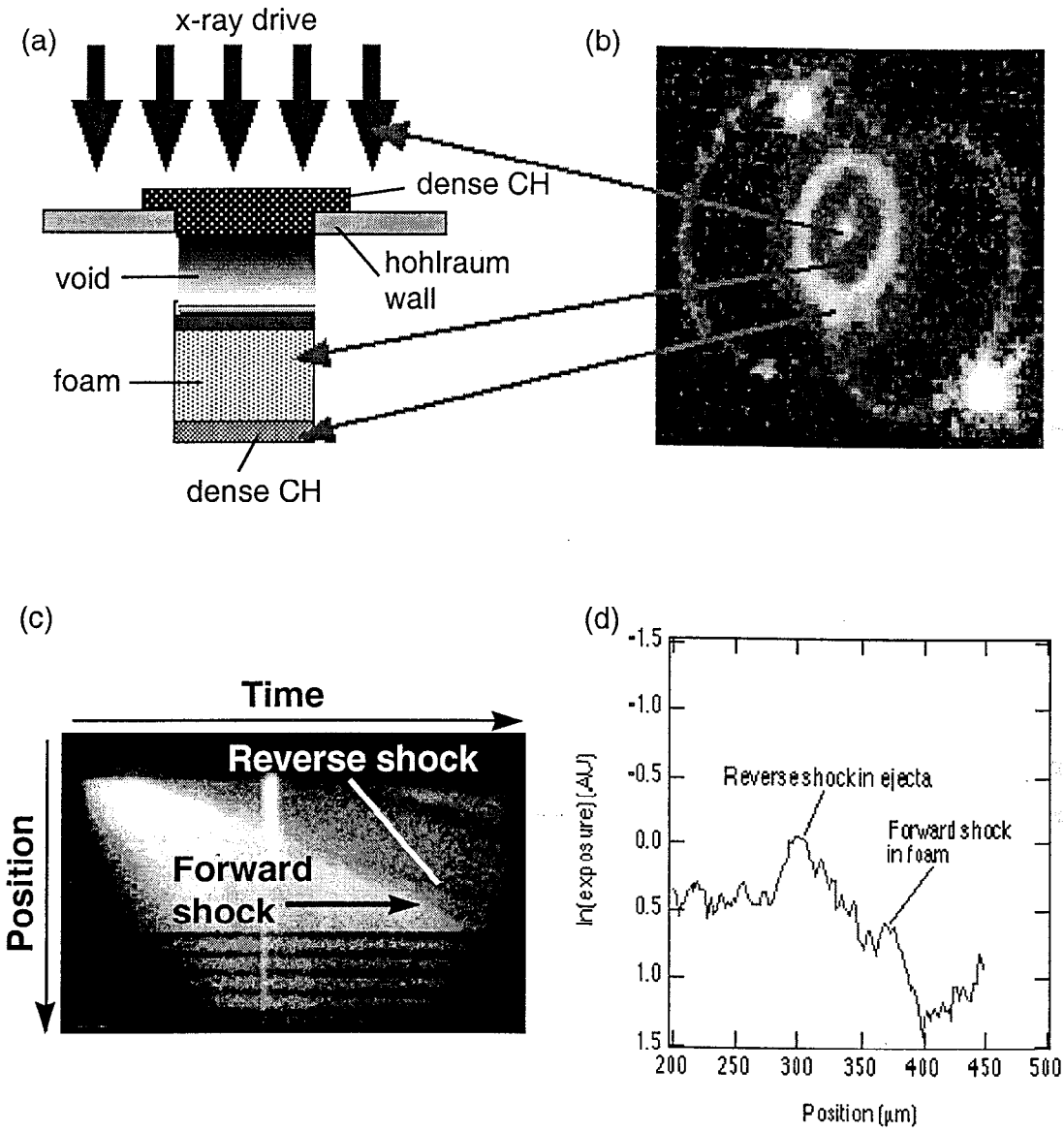

Figure B.2: SNR 1987A Nova experiment. (a) Nova experiment (b) SN 1987A ejecta and ring structure (Hubble Space Telescope image). (c) Streaked radiograph from experiment. (b) Reverse and forward shock positions from optical depth measured in data at $t = 6$ ns.

B.3 Blast wave and jet experiments

Two other examples of astrophysical experiments on large lasers are the blast wave experiments at the Falcon laser at LLNL, and the radiative jet experiments which have been carried out recently at the Nova laser and at the Gekko laser (see Section 1.4.2.3) in Osaka, Japan.

A schematic for the Falcon blast wave experiment is shown in Figure B.3a, and results from the experiment are shown in Figure B.3b–c. The figures are reproduced from [138]. The goal of the experiment was to observe blast waves in high-temperature cylindrical plasmas, establishing a testbed for the study of astrophysically-relevant shock physics. Gas targets of Ar, N_2 and Xe at densities of 10^{18} cm^{-3} were irradiated with a 30 fs Ti:sapphire laser. Atomic clusters form in the gas jets; the clusters strongly absorb the laser light, creating the high temperature plasma. The electron density was measured by Michelson interferometry, and the creation of the cylindrical plasma of dimensions 50 μm$\times$ 5000 μm was observed, using F/15 optics.

A strong blast wave was observed in the electron density profiles. In the case of Xe gas, shown in Figure B.3b, a radiative precursor was observed ahead of the shock; a precursor was not seen for N_2, and was seen for Ar. A radiative precursor is expected for the higher atomic number (Z) gases. The trajectory of the blast waves were compared to simulations using HYADES (see Section 1.6.1). The simulations predicted a Sedov-Taylor expansion of the blast wave, when radiation transport was not included in the simulation, but overpredicted the blast wave velocity in this case. With radiation transport turned on, the simulation reproduced the blast wave trajectory; this suggested that radiative cooling of the blast wave slowed the blast wave. The thin shell Vishniac instability, seen in Xe in the Grun *et al.* [75] experiments described in Section 1.5, was not seen in the Falcon experiments. The researchers concluded that the effective adiabatic exponent γ was closer to 5/3 than to the 1.2 threshold required for the Vishniac instability.

Farley *et al.* [65] have recently performed a superb radiative jet experiment at the Nova laser. High Mach number radiatively-cooled jets are observed throughout our galaxy [65], and proper modeling of the radiation is required to numerically simulate such jets. A schematic for the radiative jet experiment is shown in Figure B.3. A conical dimple is machined in a target of high-Z material. The inside of the cone is illuminated in direct

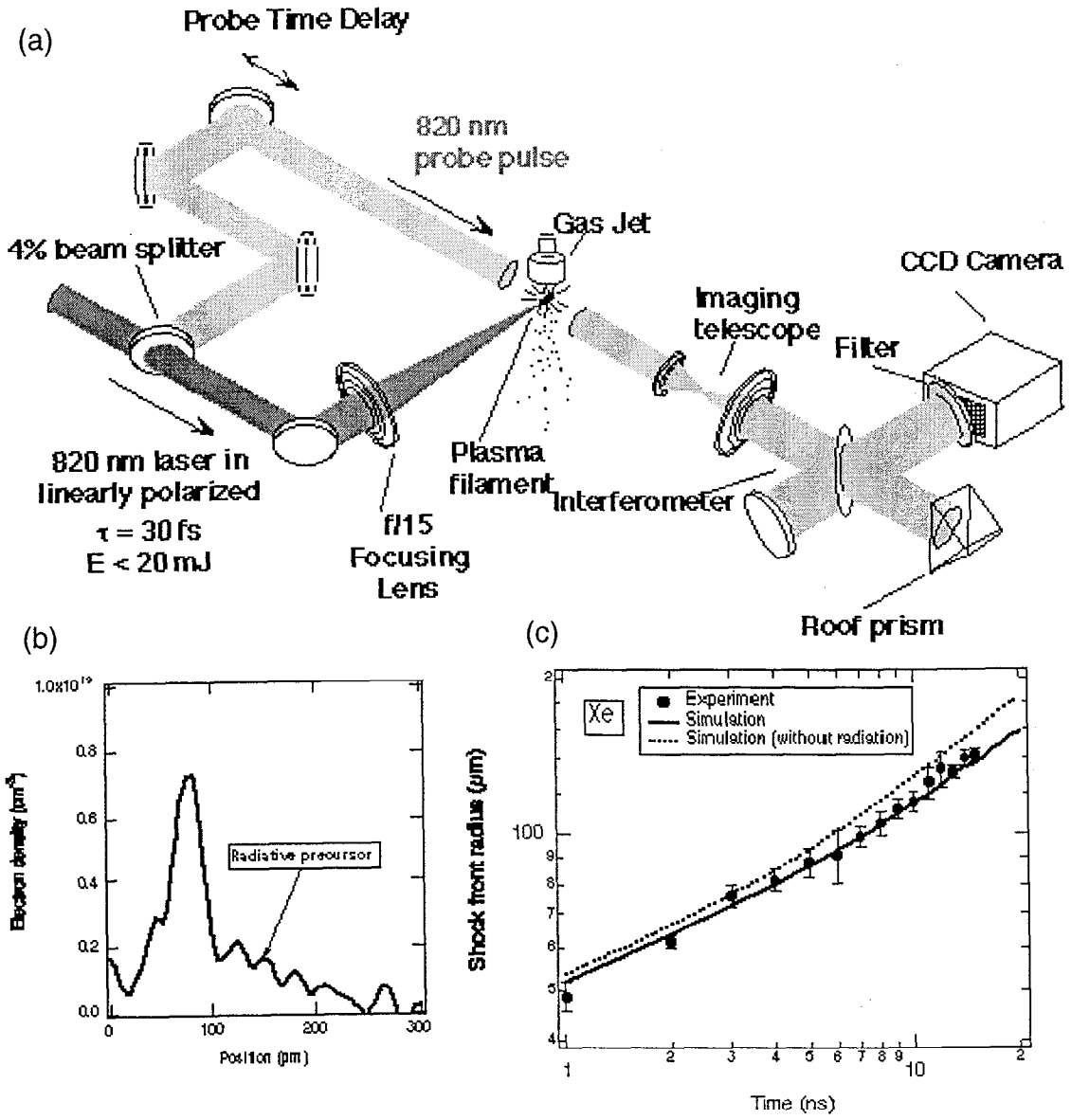

Figure B.3: Falcon laser blast wave experiment. (a) Schematic of experiment. (b) Electron density profile for Xe gas, showing radiative precursor. (c) Blast wave trajectory for Xe gas, showing effect of radiative losses. Figures reproduced from [138].

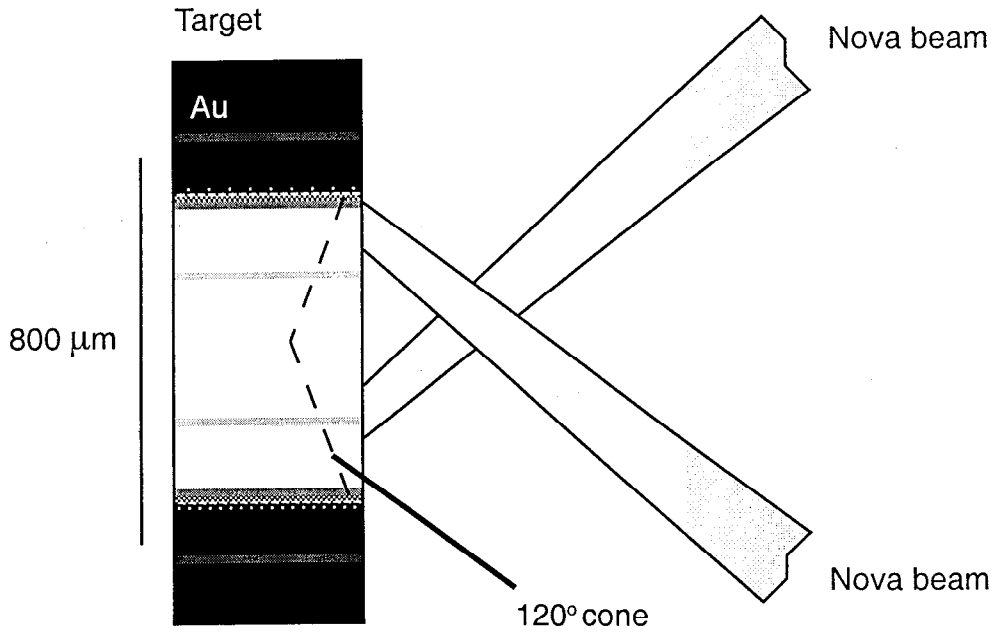

Figure B.4: Radiative jet experiment.

drive by the laser beams, which produces a blowoff that crashes in on-axis and jets out along the axis. The jet becomes hot enough to radiate, and then cools radiatively and collapses. Clear observations of the high speed jet and its radiatively cooled core were made, and were in good agreement with sophisticated numerical simulations. This experiment is an excellent test of radiation hydro codes; simulations of the experiment will require a proper treatment of radiation, which is not needed for the hydrodynamics-dominated experiments we have described in Chapters 4 and 5 and in this chapter. Similar, extremely succesful experiments with a number of different target materials have recently been done at the Gekko laser (see Section 1.4.2.3) at Osaka University.

REFERENCES

[1] Osaka University Institute of Laser Engineering Web Page. http://www.osaka-u.ac.jp/english/organ/jointuse/07.html.

[2] Vulcan laser web sites. http://www.cclrc.ac.uk/News/02jul96.html http://www.nikhefk.nikhef.nl/ed/direct/england.html http://www.clrc.ac.uk/Publications/Lasers/Vulcan.html.

[3] The National Ignition Facility: An Overview. Energy and Technology Review, December 1994.

[4] A N Aleshin, E G Gamalli, S V Zaitsev, E V Lazareva, I G Lebo, and V B Rozanov. Nonlinear and transitional stage in the onset of Richtmyer-Meshkov instability. *Sov. Tech. Phys. Lett*, 14:466–468, 1988.

[5] U Alon, J Hecht, D Mukamel, and D Shvarts. *Phys. Rev. Lett.*, 72:2867, 1994.

[6] U Alon, J Hecht, D Ofer, and D Shvarts. Power laws and similarity of Rayleigh-Taylor and Richtmyer-Meshkov Mixing Fronts at all Density Ratios. *Phys. Rev. Lett.*, 74:534, 1995.

[7] V M Antonov, V P Bashurin, A I Golubev, V A Ahmailo, A M Zakharov, , A G Orishich, A G Ponomarenko, V G Posukh, and Snytnikov. Study of the collisionless interaction of interpentrating super-Alfven plasma flows. *J. Appl. Mech. Techn. Phys.*, 26(6):757–764, 1985.

[8] D Arnett. *Astrophys. J.*, 319:163, 1987.

[9] D Arnett. private communication, 1998.

[10] D Arnett, J N Bahcall, R A Kirshner, and S E Woosley. Supernova 1987A. *Ann. Rev. A. Ap*, 27:629, 1989.

[11] D Arnett, B A Fryxell, and E Müller. *Astrophys. J.*, 341:L63, 1989.

[12] David Arnett. *Supernovae and Nucleosynthesis.* Princeton University Press, Princeton, 1996.

[13] David Arnett and Grant Bazán. Nucleosynthesis in Stars: Recent Developments. *Science*, 276:1359, May 30 1997.

[14] R Bandiera. *Astron. Astrophys.*, 319:186, 1984.

[15] R Bandiera. *Astrophys. J.*, 319:186, 1987.

[16] R T Barton. In J M Centrella, J M LeBlanc, and R L Bowers, editors, *Numerical Astrophysics*, pages 482–497. Jones and Bartlett Publishers, Boston, 1985.

[17] Basko, M M. *Phys. Plasmas*, 1:1270, 1994.

[18] Grant Bazán. private communication, 1997.

[19] Grant Bazán. private communication, 1999.

[20] Grant Bazán and David Arnett. Two-dimensional Hydrodynamics of PreCore Collapse: Oxygen Shell Burning. *Astrophys. J.*, 496-1998:316, March 20 1998.

[21] P M Bell, J D Kilkenny, O L Landen, R L Hanks, and D K Bradley. *Rev. Sci. Instrum*, 63:5073, 1992.

[22] R Benjamin. Shock and Reshock of an unstable fluid interface. In D Besnar, editor, *Third International Workshop on the Physics of Compressible Turbulent Mixing at Royaumont France*, pages 325–332. CEA DAM, 1991.

[23] R Benjamin. Experimental Observations of shock stability and shock induced turbulence. In W P Dannevik and A C Buckingham, editors, *Advances in Compressible Turbulent Mixing*, pages 341–348. National Technical Information Services, U.S. Department of Commerce, 5285 Port Royal Rd., Springfield, VA 22161, 1992.

[24] Willy Benz, Stirling A Colgate, and Marc Herant. Supernova explosions and hydrodynamic instabilities: from core bounce to 90 days. *Physica D*, 77:305–319, 1994.

[25] Willy Benz and Friedrich-Karl Thielemann. Convective Instabilities in SN 1987A. *Astrophys. J.*, 348:L17–L20, Jan. 1990.

[26] V M Blanco, B Gregory, M Hamuy, S R Heathcote, M M Phillips, N B Suntzeff, D M Terndrup, A R Walker, and R E Williams. *Astrophys. J.*, 320:589, 1987.

[27] J M Blondin, P Lundqvist, and R A Chevalier. *Astrophys. J.*, 472:257, 1996.

[28] Steven Bodner. Nike KrF Laser Facility. Technical Report NRL/PU/6730–95-289, Naval Research Laboratory, Washington, DC, June 1995.

[29] K J Borkowski, J M Blondin, and R McCray. *Astrophys. J.*, 476:L31, 1997.

[30] K J Borkowski, J M Blondin, and C L Sarazin. *Astrophys. J.*, (400):222, 1992.

[31] K J Borkowski, Sarazin, C L, and J M Blondin. *Astrophys. J.*, 429:710, 1994.

[32] J E Borovsky, M B Pongatz, R A Roussel-Dupre, and T H Tan. The laboratory simulation of unmagnetized supernova remnants: absence of a blast wave. *Astrophys. J.*, 280:802–808, May 1984.

[33] S I Braginski. *Reviews of Plasma Physics.* Consultants Bureau, New York, 1965.

[34] K S Budil, B A Remington, T A Peyser, K O Mikaelian, P L Miller, N C Woolsey, W M Wood-Vasey, and A M Rubenchik. Experimental comparison of classical versus ablative Rayleigh-Taylor instability. *Phys. Rev. Lett.*, 76:4536, 1996.

[35] Kimberly S Budil, Theodore S Perry, Richard I Klein, and David R Bach. An experimental investigation of the shock-cloud interaction. APS/AAPT Joint Meeting, April 18–21, 1998, Columbus, OH, 1998.

[36] Budil, K. S., et al. *Rev. Sci. Instrum.*, 67:485, 1996.

[37] E M Campbell. Recent results from the Nova program at LLNL. *Laser and Part. Beams.*, 9(2):209–231, 1991.

[38] E M Campbell, N C Holmes, S B Libby, B A Remington, and E Teller. *Laser and Particle Beams*, 15:607, 1997.

[39] E M Campbell, J T Hunt, E S Bliss, D R Speck, and R P Drake. Nova experimental facility. *Rev. Sci. Instrum.*, 57(8):2101–2106, 1986.

[40] Michael E Campbell, Neil C Holmes, Steven B Libby, Bruce A Remington, and Edward Teller. The evolution of high-energy-density physics: From nuclear testing to the superlaser. *Laser and Part. Beams*, 15(4):607–626, 1997.

[41] S Chandrasekhar. *Hydrodynamic and Hydromagnetic Stability.* Clarendon, Oxford, 1961.

[42] R Chevalier. *Astrophys. J.*, 207:872, 1976.

[43] R A Chevalier. *Astrophys. J.*, 258:790, 1982.

[44] Roger A Chevalier, John M Blondin, and Robert T Emmering. Hydrodynamic Instabilities in Supernova Remnants: Self-similar Driven Waves.

[45] P Colella and Glaz. *J. Comp. Phys.*, 32:101, 1979.

[46] P Colella and Glaz. *J. Comp. Phys.*, 59:264, 1986.

[47] Phillip Colella and Paul R Woodward. *J. Comp. Phys.*, 54:174, 1984.

[48] S A Colgate and C McKee. *Astrophys. J.*, 157:623, 1969.

[49] R Courant and K O Friedrichs. *Supersonic Flow and Shock Waves.* Interscience, New York, 1948.

[50] ed" "Craxton, R S. OMEGA Upgrade Preliminary Design. Laboratory for Laser Energetics REPORT DEO/DP 40200-101, University of Rochester, 1989.

[51] J P Dahlburg, J H Gardner, G D Doolen, and S W Haan. *Phys. Fluids B*, 5:571, 1993.

[52] Keay Davidson. Simulating Supernovae. *Sky and Telescope*, pages 38–40, Nov. 1997.

[53] J R Dickel, J A Eilek, and E M Jones. *Astrophys. J. Suppl.*, 70:497, 1989.

[54] J R Dickel, J A Eilek, and E M Jones. *Astrophys. J.*, 412:648, 1993.

[55] J R Dickel, W J M van Breugel, and R G Strom. *AJ*, 101:151, 1991.

[56] G Dimonte and B A Remingon. Richtmyer-Meshkov Experiments on the Nova Laser at High Compression. *Phys. Rev. Lett.*, 70(12):1806–1809, Mar. 1993.

[57] G M Dimonte, C E Frerking, M Schneider, and B A Remington. *Phys. Plasmas*, 3:614, 1996.

[58] G M Dimonte and M Schneider. *Phys. Rev. E*, 54:3740, 1996.

[59] R P Drake. Laboratory experiments to simulate the hydrodynamics of supernova remnants and supernovae. *J. Geophys. Res.*, 1999. in press.

[60] R P Drake, J P Carroll, K Estabrook, S G Glendinning, B A Remington, R Wallace, and R McCray. Development of a laboratory environment to test models of supernova remnant formation. *Astrophys. J.*, 500:L157–L161, 1998.

[61] R P Drake, S G Glendinning, Kent Estabrook, B A Remington, Richard McCray, R J Wallace, L J Suter, T B Smith, J J Carroll III, R A London, and E Liang. Observation of Forward Shocks and Stagnated Ejecta Driven by High-Energy-Density Plasma Flow. *Phys. Rev. Lett.*, 81(10):2068, 1998.

[62] R Eastman. private communication, 1998.

[63] R J Ellis, J E Trebes, D W Phillion, Kilkenny J D, S G Glendinning, J D Wiedwald, and R A Levesque. *Rev. Sci. Instrum.*, 61:2759, 1990.

[64] S W Falk and W D Arnett. *Astrophys. J.*, 180:L65, 1973.

[65] D R Farley, K G Estabrook, S G Glendinning, S H Glenzer, B A Remington, K Shigemori, J M Stone, R J Wallace, G B Zimmerman, and J A Harte. Radiative Jet Experiments of Astrophysical Interest using Intense Lasers. *Phys. Rev. Lett.*, 1999. submitted.

[66] B Fryxell. manuscript, 1999.

[67] B A Fryxell, E Müller, and D Arnett. *Astrophys. J.*, 367:619, 1991.

[68] James Glanz. Bringing the Stars Down to Earth. *Science*, 276:351–352, Apr. 18 1997.

[69] S G Glendinning. *Rev. Sci. Instrum.*, 63:5108, 1992.

[70] S G Glendinning. private communication, 1998.

[71] S K Godunov. *Mat. Sb.*, 47:271, 1959.

[72] Billy Goodman. Star in a Bottle. *Air & Space*, pages 68–76, Feb./Mar. 1998.

[73] M J Graham. *A Numerial Study of the Richtmyer-Meshkov Instability in Cylindrical Geometry.* PhD thesis, State University New York, Stony Brook, NY, December 1996.

[74] J W Grove, R Holmes, D H Sharp, Y Yang, and Q Zhang. *Phys. Rev. Lett.*, 71:3473, 1993.

[75] J Grun, J Stamper, J Manka, J Resnick, R Burris, J Crawford, and B H Ripin. Instability of Taylor-Sedov blast waves propagating through a uniform gas. *Phys. Rev. Lett.*, 66(21):2738–2741, 1991.

[76] S F Gull. *MNRAS*, 161:47, 1973.

[77] Izumi Hachisu and Takuya Matsuda. Mixing in Ejecta of Supernovae. I. General Properties of Two-dimensional Rayleigh-Taylor Instabilities and Mixing Width in Ejecta of Supernovae. *Astrophys. J.*, 390:230–252, May 1 1992.

[78] S W Hann. Weakly nonlinar hydrodynamic instabilities in intertial fusion. *Phys. Fluids B*, 3(8):2349–2355, Aug. 1991.

[79] C J Hansen and S D Kawaler. *Stellar Interiors.* A&A Library, New York, 1995.

[80] R W Hanuschik and J Dachs. *Astron. Astrophys.*, 192:L29, 1987.

[81] J Hecht, U Alon, and D Shvarts. Potential flow models of Rayleigh-Taylor and Richtmyer-Meshkov bubble fronts. *Phys. Fluids*, 6:4019, 1994.

[82] J Hecht, D Ofer, D Alon, D Shvarts, S A Orszag, and R L McCrory. Three-dimensional simulations and analysis of the nonlinear stage of the Rayleigh-Taylor instability. *Laser and Part. Beams*, 13(3):423–400, 1995.

[83] M Herant and S E Woosley. Postexplosion Hydrodynamics of Supernovae in Red Supergiants. *Astrophys. J.*, 425:814, 1994.

[84] Richard L Holmes, Guy Dimonte, Bruce Fryxell, Michael L Gittings, John W Grove, Marilyn Schneider, David H Sharp, Alexander L Velikovich, Robert P Weaver, and Qiang Zhang. Richtmyer-Meshkov Instability Growth: Experiment, Simulation and Theory. *J. Fluid Mechanics*, 1999. submitted.

[85] Richard L Holmes, John W Grove, and David H Sharp. Numerical investigation of Richtmyer-Meshkov instability using front tracking. *J. Fluid Mech.*, 301:51–64, 1995.

[86] J W Jacobs and I Catton. *J. Fluid Mech.*, 187:329, 1987.

[87] J W Jacobs and I Catton. *J. Fluid Mech.*, 187:353, 1987.

[88] B I Jun, T W Jones, and M L Norman. *Astrophys. J.*, 468:L59, 1996.

[89] B I Jun and M L Norman. *Astrophys. J.*, 465:800, 1996.

[90] B I Jun and M L Norman. *Astrophys. J.*, 472:245, 1996.

[91] B I Jun, M L Norman, and J M Stone. *Astrophys. J.*, 453:332, 1995.

[92] J Kane, D Arnett, B A Remington, G Bazán, E Mller, S G Glendinning, and B A Fryxell. 2D vs. 3D supernova hydrodynamic instability growth. *Astrophys. J.*, 1999. submitted.

[93] J Kane, D Arnett, B A Remington, S G Glendinning, J Castor, R Wallace, A Rubenchik, and B A Fryxell. Supernova-relevant hydrodynamic instability experiments on the Nova Laser. *Astrophys. J.*, 478:L75, 1997.

[94] J Kane, R P Drake, and B A Remington. An Evaluation of the Richtmyer-Meshkov instability in SNR Formation. *Astrophys. J.*, 511:335, Jan. 1999.

[95] R Kippenhahn and A Weigert. *Stellar Structure and Evolution.* Springer-Verlag, Berlin, 1994.

[96] Laboratory for Laser Energetics, University of Rochester. *National Laser User's Facility User's Guide*, Jan. 1998.

[97] L Landau and E Lifshitz. *Fluid Dynamics.* Pergammon Press, Princeton, 1960.

[98] J T Larsen and S M Lane. *J. Quant. Spect. Rad. Trans.*, 51:179, 1994.

[99] James M Lattimer and Adam S Burrows. Neutrinos from Supernova 1987A. *Sky & Telescope*, pages 348–350, Oct. 1988.

[100] David Layzer. On the instability of superposed fluids in a gravitational field. *Astrophys. J.*, 122(1):1–4, July 1955.

[101] H W Liepmann and A Roshko. *Elements of Gasdynamics.* Wiley, New York, 1957.

[102] J D Lindl, R L McCrory, and E M Campbell. Progress towareds ignition and burn propagation in inertial confinement fusion. *Phys. Today*, 5:32, 1992.

[103] J D Lindl and W C Mead. *Phys. Rev. Lett.*, 34:1273, 1975.

[104] Lord Rayleigh. Scientific Papers II. Cambridge, England, 1900.

[105] D Luo and R A Chevalier. *Astrophys. J.*, 435:815, 1994.

[106] M M MacLow and M L Norman. Nonlinear Growth of Dynamical Overstabilities in Blast Waves. *Astrophys. J.*, 407:207–218, Apr. 1993.

[107] M M Marinak, B A Remington, S V Weber, R E Tipton, S W Haan, K S Budil, O L Landen, J D Kilkenny, and R Wallace. Nonlinear Rayleigh-Taylor Evolution of a Three-Dimensional Multimode Perturbation. *Phys. Rev. Lett.*, 75:3677, 1995.

[108] K Masai and K Nomoto. *Astrophys. J.*, 424:924, 1994.

[109] R McCray. Supernova 1987A Revisited.

[110] E E Meshkov. *Izv. Akad. Nauk SSSR Mekh. Zhidk.*, Gaza 4:151, 1969. [Izv. Acad. Sci. USSR Fluid Dynamics 4, 101 (1969)].

[111] K A Meyer and P J Blewett. *Phys. Fluids*, 15:753, 1972.

[112] K O Mikaelian. *Phys. Rev. Lett.*, 80:508, 1998.

[113] Karnig O Mikaelian. Rayleigh-Taylor instability in finite-thickness fluids with viscosity and surface tension. *Phys. Rev. E*, 54(4):3676–3680, Oct. 1996.

[114] E Müller. *Astron. Astrophys.*, 162:103, 1986.

[115] E Müller, B A Fryxell, and D Arnett. *Astron. Astrophys.*, 251:505, 1991.

[116] E Müller, B A Fryxell, and D Arnett. In F Federini, J Franco, and F Matteucci, editors, *Elba Workshop on Chemical and Dynamical Evolution of Galaxies*, Pisa, 1991. ETS Editrice.

[117] D Munro. *Phys. Fluids B*, 1:134, 1989.

[118] S Nagatki, T M Shimizu, and K Sato. Matter Mixing from Axisymmetric Supernova Explosion. *Astrophys. J.*, 495:413, 1998.

[119] A M Orishich, I F Shakhislamov, and V G Posukh. A self-compression of laser-produced plasma into thin monovelocity shell. *Laser and Part. Beams*, 1996. in press.

[120] E Ott. *Phys. Rev. Lett.*, 29:1429, 1995.

[121] T A Peyser, P L Miller, P E Stry, K S Budil, E W Burke, D A Wojtowicz, D L Griswold, B A Hammel, and D W Phillion. Measurement of radiation-driven shock-induced mixing from nonlinear initial perturbations. *Phys. Rev. Lett.*, 75:2332, 1995.

[122] M S Plesset. On the Stability of Fluid Flows with Spherical Symmetry. *J. Appl. Phys.*, 28(1):96–98, Jan. 1954.

[123] Pye, J P et al. *MNRAS*, 194:569, 1981.

[124] K I Read. Experimental investigation of turbulent mixing by Rayleigh-Taylor instability. *Physica D*, 12:32–44, 1984.

[125] B A Remington, S G Glendinning, R J Wallace, S Rothman, and S Morales. *Rev. Sci. Instrum*, 63:5080, 1992.

[126] B A Remington, B A Hammel, O L Landen, and R A Pasha. *Rev. Sci. Instrum*, 63:5083, 1992.

[127] B A Remington, S V Weber, S W Haan, J D Kilkenny, S G Glendinning, R J Wallace, W H Goldstein, B G Wilson, and J K Nash. laser-driven hydrodynamic instability experiments. *Phys. Fluids B*, 5(7):2589–2595, July 1993.

[128] B A Remington, S V Weber, M M Marinak, S W Haan, J D Kilkenny, R Wallace, and G Dimonte. Multimode Rayleigh-Taylor Experiments on Nova. *Phys. Rev. Lett.*, 73(4):545–548, July 1994.

[129] S P Reynolds and D M Gilmore. *AJ*, 92:1138, 1986.

[130] R D Richtmyer. *Commun. Pure App. Math.*, 13:297, 1960.

[131] S J Rose. High-power laser-produced plasmas and astrophysics. *Laser and Part. Beams*, 9(4):869–879, 1991.

[132] Steven Rose. Astropysical plasma laboratories. *Physics World*, April 1994.

[133] A M Rubenchik, K S Budil, C Brown, S G Glendinning, D Gold, K Estabrook, D Pennington, M Perry, B A Remington, T C Sangster, R Wallace, K Keilty, and E Liang. Simulating High Speed Meteorite Impact Physics with Experiments on the PetaWatt Laser. Presentation at APS Division of Plasma Physics Annual Meeting, Nov. 18, 1998, New Orleans, LA, Nov. 1998.

[134] D Ryutov, R P Drake, J Kane, E Liang, B A Remington, and W M Wood-Vasey. Similarity criteria for the laboratory simulation of supernova hydrodynamics. *Astrophys. J.*, June 1999. in press (June 1999).

[135] M Schneider, G Dimonte, and B A Remington. *Phys. Rev. Lett.*, 80:3507, 1998.

[136] L I Sedov. *Similarity and Dimensional Methods in Mechanics.* Academic Press, New York, 1959.

[137] F Seward, P Gorenstein, and W Tucker. *Astrophys. J.*, 266:287, 1983.

[138] K Shigemori, T Ditmire, T Kuehl, B A Remington, A M Rubenchik, M J Edwards, V Yanovsky, and D Ryutov. Measurements of strong blast waves in gas targets. presentation to DPP98 meeting of the APS, New Orleans, LA, Nov. 17–21 1998.

[139] T Shigeyama and K Nomoto. Theoretical Light Curve of SN 1987A and Mixing of Hydrogen and Nickel in the Ejecta. *Astrophys. J.*, 360:242, 1990.

[140] Steven Shore. *An Introduction to Astrophysical Hydrodynamics.* Academic Press, San Diego, 1992.

[141] D Shvarts, U Alon, D Ofer, R L McCrory, and C P Verdon. *Phys. Plasmas*, 1995(6):2465, 1995.

[142] S Skupsky, R W Short, T Kessler, R S Craxton, Letzring S, and J M Soures. Improved Laser-Beam Uniformity Using the Angular Dispersion of Frequency-Modulated Light. *J. Appl. Phys.*, 66:3456, 1989.

[143] T Suzuki, T Shigeyama, and K Nomoto. *Astron. Astrophys.*, 274:883, 1993.

[144] H Takabe, K Mima, L Montierth, and R L Morse. *Phys. Fluids*, 28:3676, 1985.

[145] Taylor, Sir Geoffrey. *Proc. R. Soc. London*, A201:192, 1950.

[146] R Teyssier, J P Chieze, S Bouquet, F Mucchielli, A Benuzzi, and F Thais, 1999. in preparation.

[147] Romain Teyssier, Dmitri Ryutov, and Bruce Remington. Accelerating Shock Waves in a Laser Produced Density Gradient. In *Astrophys. J. Suppl.Proceedings of the 2nd International Workshop on Laboratory Astrophysics with intense lasers, Mar. 19–21, 1998*, Univ. of Arizona, Tucson, AZ, 1999. submitted.

[148] J Tueller, S Barthelmy, N Gehrels, B J Teegarden, M Leventhal, and C J MacCallum. *Astrophys. J.*, 351:L41, 1990.

[149] A L Velikovich. Analytic theory for Richtmeyer-Meshkov instability for the case of a reflected rarefaction wave. *Phys. Fluids*, 8(6):1666–1679, 1996.

[150] A L Velikovich and G Dimonte. *Phys. Rev. Lett.*, 76:3112, 1996.

[151] E T Vishniac. The dynamic and gravitational instabilities of spherical shocks. *Astrophys. J.*, 274:152–167, Nov. 1983.

[152] G B Whitham. *Linear and Nonlinear Waves.* Wiley-interscience, New York, 1974.

[153] F C Witteborn, J D Bregman, D H Wooden, P A Pinto, D M Rank, S E Woosley, and M Cohen. *Astrophys. J.*, 338:L9, 1989.

[154] Paul R Woodward and Phillip Colella. *J. Comp. Phys.*, 54:115, 1984.

[155] Stan Woosley and Tom Weaver. The Great Supernova of 1987. *Scientific American*, pages 32–40, Aug. 1989.

[156] T Yabe, H Hoshino, and T Tsuchiya. 2-DIMENSIONAL AND 3-DIMENSIONAL BEHAVIOR OF RAYLEIGH-TAYLOR AND KELVIN-HELMHOLTZ INSTABILITIES. *Phys. Rev. A*, 44(4):2756, 1991.

[157] Shoichi Yamada and Katsuhiko Sato. Rayleigh-Taylor in the Asymmetric Supernova Explosion. *Astrophys. J.*, 1991.

[158] Yang Yang, Qiang Zhang, and David H Sharp. Small amplitude theory of Richtmyer-Meshkov Instability. *Phys. Fluids*, 6:1856–1873, 1994.

[159] Y Yedvab, U Alon, D Oron, and D Shvarts. Single and Multi-mode Rayleigh-Taylor Instability in Cylindrical Systems. In *6th IWPTCM, Marseille*, pages 528–533, Jun. 1997.

[160] Youngs. *Physica D*, 37:270, 1989.

[161] David L Youngs. Numerical simulation of turbulent mixing by Rayleigh-Taylor instability. *Physica D*, 12:45–48, 1984.

[162] Y P Zakharov, A G Orishich, A G Ponomarenko, V G Posukh, and V N Snytnikov. Laboratory simulation of collisionless coupling between supernova remnants and magnetised interstellar medium. In *Plasma Astrophysics: Proceedings fo the Joint Varenna-Abastumani International School and Workshop*, pages 37–40, Sukhumi, USSR, 1986. European Space Agency.

[163] Q Zhang and S I Sohn. *Phys. Lett. A*, 212:149, 1996.